DISCLAIMER

CASL-U-2017-1429-000

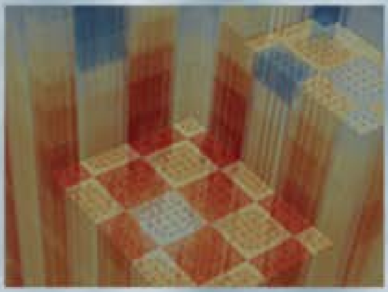

Summary report describing CASL accomplishments in support of the GTRF Challenge Problem

Brian D. Wirth (GTRF Challenge Problem Integrator), University of Tennessee and Oak Ridge National Laboratory, on behalf of:

Peter J. Blau[2], Ken Kamrin[3], Sladjan Lazarevic[1], Roger Lu[4], Wei Lu[4], David Parks[2], Anirban Patra[5], Michael Thouless[4], Carlos Tome[5], and Jun Qu[1]

[1] Oak Ridge National Laboratory
[2] Blau Tribology Consulting
[3] Massachusetts Institute of Technology
[4] Westinghouse Electric Company
[5] University of Michigan
[6] Los Alamos National Laboratory

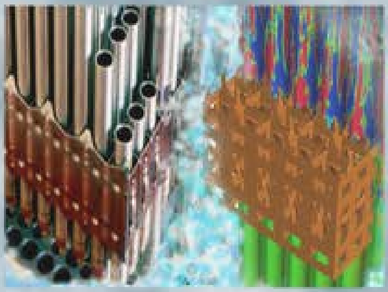

September 20, 2017

REVISION LOG

Revision	Date	Affected Pages	Revision Description
0		All	Initial Release

Document pages that are:

Unlimited_____ALL____

Export Controlled ______NONE____

IP/Proprietary/NDA Controlled______NONE___________________________________

Sensitive Controlled______NONE____

Requested Distribution:

To:

Copy:

EXECUTIVE SUMMARY

Coolant flow-induced relative motions between structural components in the cores of lightwater nuclear reactor cores, a phenomenon called Grid-To-Rod Fretting (GTRF), can result in progressive wear damage. Wear-through of the cladding on fuel rods can introduce radioactive species into the coolant loop. Such an event is termed a “leaker” and may cause premature and expensive reactor shut-down. GTRF results in wear scars of various sizes, shapes, and depths on the sides of the fuel rod cladding. Fretting damage may also occur on the springs and dimples that hold the fuel rods in place, resulting in the formation of gaps. Due to variability in the operating conditions of the reactor (burn-up rates and operating campaigns) and the associated variable cladding surface oxide film growth and removal rates, the wear coefficient is unlikely to remain constant over time. Therefore, constant wear rate models do not accurately account for transients in the operating conditions.

CASL has developed a stage-wise GTRF engineering wear model (EWM), as well as performed extensive computational fluid dynamics modeling of the fluid structure interactions, structural mechanics assessments of the GTRF phenomena and developed a novel, autoclave fretting and impact rig for providing laboratory benchmarking data. The CASL team has recently refined the EWM, exercised the EWM for different operating scenarios, investigated the possible effects of impacts or gaps on the fretting wear, and derived a materials science-based wear factor. In order to train and validate the EWM (or any other wear models), experimentally determined cladding wear coefficients are definitely needed. This is because the wear coefficient largely depends on the alloy composition of the cladding and grid materials, surface conditions (e.g., oxidation), contact geometry, water temperature, fluid chemistry, and flow rate (inducing vibration). However, the wear coefficients in actual nuclear reactors are very difficult to quantify, if not impossible. A few assembly dynamometer GTRF testers are available at major nuclear engineering companies, such as the Vibration Investigation and Pressure-drop Experiment Research (VIPER) system at WEC, but tests are very expensive and not accessible to outside researchers. Most non-reactor, benchtop wear tests fall short of producing an accurate physical simulation of GTRF due to limitations in temperatures, coolant pressures and chemistry, absence of radiation effects, and complex types of fretting and impact motions.

ORNL has worked with Phoenix Tribology (UK) to successfully design and fabricate a unique Autoclave Fretting and Impact Rig (AFIR) with well-controlled, realistic testing parameters (contact geometry, load, oscillation frequency and amplitude) in pressurized water environments (up to 220 ^{o}C, similar to the VIPER at WEC). In each test, a commercial Zr-based alloy cladding segment in either as-received or pre-oxidized surface condition was rubbing against a commercial grid of a Zr alloy (as-received or pre-oxidized) or stainless steel. Fretting tests were carried out under a variety of water temperatures from 22 to 204 ^{o}C in both D.I. water and simulated PWR coolants containing H_3BO_3 (1000 ppm B), LiOH (2.3 ppm Li), and/or H_2 (0.25 ppm). Major achievements and observations include:

- The good agreement between ORNL AFIR and WEC VIPER on both wear rate and morphology provides a solid foundation for correlating AFIR results with field experience and using them for training and validating GTRF models, including the CASL developed EWM.
- Surface treatment of the cladding and grid material are important. Pre-oxidation of Zr alloy cladding and/or using stainless steel grid effectively reduced the cladding wear rate.
- Wear and corrosion must be considered together. Fretting can dramatically promote oxidation/corrosion, and wear reduction may come at a price of oxidation/corrosion.
-

The work is felt to be a significant step because results are based on a combination of past work, observations of wear damage on actual fuel rods and simulated out-of-reactor experiments. This report summarizes the CASL accomplishments on the GTRF Challenge Problem involving the development and refinement of the EWM, and structural mechanics assessments that highlight the role of crystallographic texture on gap opening between the spacer grid and fuel clad, the effect of creep, oxidation and wear on the fretting wear depth, and multi-rod considerations that influence the location within fuel assemblies that are most susceptible to GTRF. Further, the AFIR tests provided important data for modifying the EWM to account for material pair, cladding pre-oxidation, temperature, and coolant chemistry; and the AFIR will be available for future industry testing needs in support of advanced fuel assemblies or accident tolerant fuel.

CONTENTS

FIGURES

TABLES

ACRONYMS

Table A. General Acronyms

Acronym	Meaning
AFIR	autoclave fretting and impact rig, a custom-designed apparatus used for validation tests
BTC	Blau Tribology Consulting
CASL	Consortium for Advanced Simulation of Lightwater Reactors
CRUD	originally “Chalk River Unidentified Deposits”; now insoluble yellowish deposits in reactor coolant systems arising from various sources such as corrosion scales – may be radioactive or act as a neutron absorber.
DOE	United States Department of Energy
EWM	a multi-stage engineering wear model developed for GTRF
FMC	Fuels, Materials, and Chemistry effort within CASL
GTRF	grid-to-rod fretting
PWR	lightwater reactor
ORNL	Oak Ridge National Laboratory
WEC	Westinghouse Electric Company, Nuclear Engineering

Table B. Symbols used in the GTRF EWM (except where otherwise noted in the text)

Symbol	Description	Units of measure
A	area of the wear scar on the cladding	mm^2
F	kinetic friction force (=μP)	N
L	length of the wear scar parallel to the axis of the fuel rod	mm
$LEWR$	the linear equivalent wear rate based only on the final wear depth at the conclusion of the operating period of interest. It is in effect, the average wear per day based only on the end points of the calculation.	mm/day
P	normal force applied to the wear scar during fretting contact	N
Q	grouping of variables used in the calculation of z_{inc} (see Eqn.5)	mm^3/s
t_{inc}	time of sliding during given interval of fretting	s
t_o	incubation period during which there is no wear	days
t_{op}	total operating time, usually used to plot depth versus time results	days
w	width of a wear scar on a cylindrical tube (= b if the scar is elliptical)	mm
W_f	wear factor used during the given stage of GTRF wear (Note that the wear volume is normalized by the product of friction force and sliding distance (=F). This differs from traditional wear factors in which the denominator contains the normal force (P).)	mm^3/N-m (converts to Pa^{-1} dividing by 10^9)
x	total sliding distance during time interval t_{inc}	mm
z	total depth of wear; the sum of the initial wear depth and the increment z_i	µm or mm
z_0	depth of wear at the beginning of the increment of calculation	µm or mm
z_{crit}	maximum depth of wear that is selected to be the point of cladding failure; in most cases this is 80-90% of the initial cladding thickness.	µm or mm
z_i	increment of new wear depth for the given increment of calculation and which is added to z_0 to obtain the total cumulative wear depth z	µm or mm
z_{ox}	thickness of the initial zirconium oxide on the cladding at start-up	µm or mm
μ	average friction coefficient on the wear scar during the given interval of wear calculation	non-dimensional
δ	amplitude of fretting (stroke length)	µm
ν	frequency of fretting	s^{-1}

1. GRID TO ROD FRETTING (GTRF) CHALLENGE PROBLEM DESCRIPTION

Grid-to-rod fretting (GTRF) wear is currently one of the main causes of fuel leakage and is responsible for over 70% of the fuel leaking in pressurized water reactors (PWRs) in the U.S [1,2]. The Consortium for Advanced Simulation of Light Water Reactors (CASL) has identified GTRF as a critical and challenging problem that is very important to nuclear plants. The main causes of failure have been identified as the relaxation of the grid-to-rod support in the assembly and the flow-induced vibration.

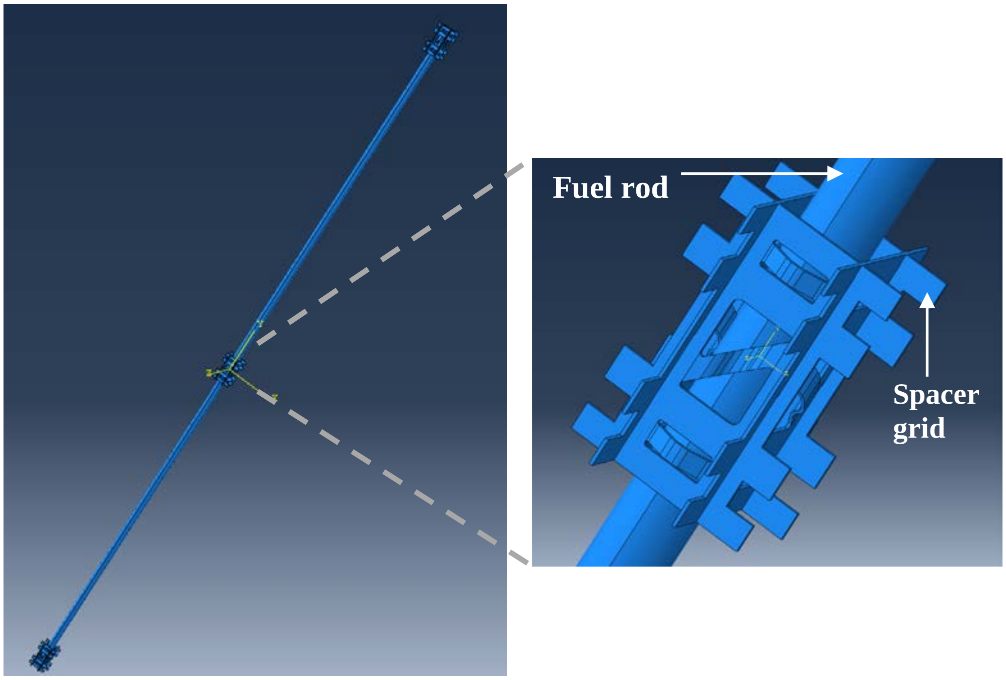

Figure 1. Schematic illustration of a section of a fuel rod, with detailed view of spacer grid geometry.

Fuel rods in the fuel assembly are supported by springs and dimples of the spacer grid, as schematically illustrated in Figure 1 [3]. As the coolant flows through the fuel assembly, the initial preload between the grid and the fuel rod can prevent gross sliding between the two components. However, the turbulent flow of the coolant can cause partial slip at the edges of each contact; this can cause local fretting wear. Furthermore, the initial preload between the grid and the fuel rod will relax over time as a result of deformation processes that take place in the reactor. Finally, the contact force between the grid and the fuel rod will relax to such an extent that gross sliding between the fuel rod and the grid occurs. This enhances the fretting wear, as the resultant wear scar further accelerates the relaxation of the contact force. Eventually, the springs and dimples of the spacer grid will lose contact with the fuel rod, and a gap will form between them. This gap enables larger amplitudes of vibration and dynamic impact between the contacts. This results in a significant increase in the wear [2-6].

Overall, reliable GTRF simulations require integration of quasi-static (in the early stage of wear) and dynamic (after a gap opens) structural analyses, turbulent flow calculations, the modeling of material behavior at high temperatures and in an irradiation environment, and the simulation of local contact and wear. In this report, the state-of-the-art modeling methodology developed to solve GTRF-related problems is described. This will be followed by a summary of the research accomplishments with respect to the effect of creep, wear, turbulence flow, structural analysis and the coupling of wear and creep. The overall approach to modeling and assessing the GTRF problem is shown in Figure 2. It should be noted that early in the initial stage of CASL work on GTRF, the focus was on integrated modeling of fluid structure interactions with concurrent structural mechanics assessment of the wear scar development. The computational fluid dynamics effort within that approach did provide a key conclusion that the fuel rod displacement, acceleration and wear work-rates as obtained from the non-linear dynamics computations using the Westinghouse VITRAN code are relatively insensitive to the use of either computational fluid dynamics modeling using Hydra-TH or Star-CCM+ for computing fluid forces on the rod [7]. However, it rapidly became apparent that the time scale challenges of the order 10 hertz rod vibrations coupled with the impact and sliding forces made this a very intractable problem. Subsequently, CASL sought to decouple the various aspects of the GTRF phenomena with CFD modeling to assess the turbulent kinetic energy excitation forces driving the rod vibration, structural mechanics modeling to assess the gap development and pragmatically evaluate numerous factors associated with the grid to rod impact and sliding forces and gap development, as well as a multi-stage engineering wear model that will be calibrated against an increasing database of laboratory wear test results.

The CFD modeling was completed in the FY13-FY14 timeframe, and the current emphasis within the project relates to the demonstration of modeling the grid to rod gap development resulting from thermal and irradiation creep, along with structural mechanics assessments of the contact mechanics and wear development, and the deployment of a specially designed, bench top fretting wear test device to develop a laboratory database to calibrate the multi-stage engineering wear model. Again, it is important to highlight that the CFD analysis indicated that the rod vibration derived from the fluid structure interaction are relatively insensitive to the choice of fluid dynamics modeling approach [7]. In the remainder of this document, the accomplishments of the resulting program to evaluate the structural mechanics of GTRF wear, with a limited examination of turbulent fluid dynamics, along with the development of an experimentally validated engineering wear model that is benchmarked to benchtop scale autoclave fretting and impact test rig are described. These accomplishments have also resulted in sixteen (16) peer-reviewed, archival journal publications, which are provided as a list in Appendix A.

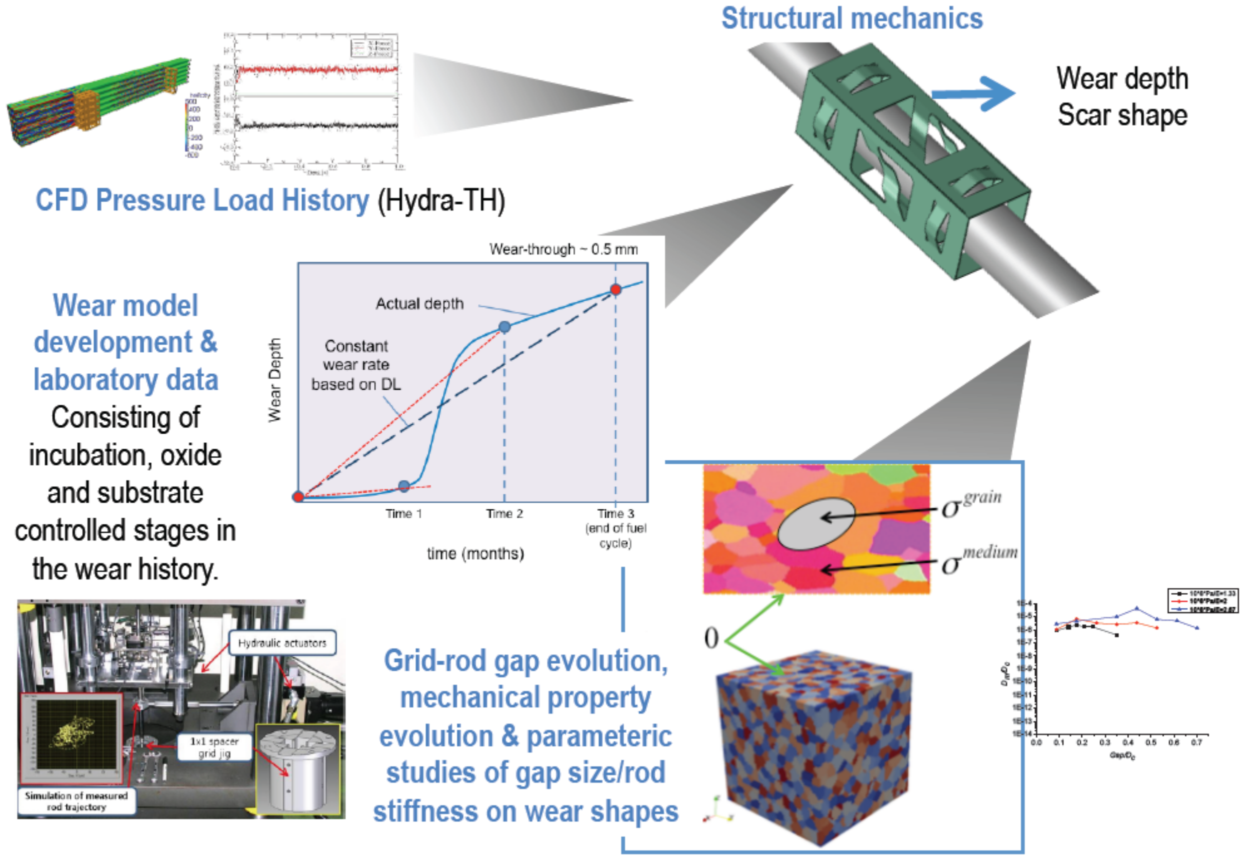

Figure 2. CASL strategy for modeling GTRF, employing CFD simulations to provide turbulent excitation forces, structural mechanics to model the gap development and evolution of the grid-to-rod contact, as well as parametrically evaluating key factors controlling wear depth, along with the development of an advanced, multistage engineering wear model calibrated against laboratory test data.

1.1 Tribology of wear and approach towards engineering wear model

In tribology, fretting is defined as the small-amplitude relative motion between contacting surfaces that can eventually produce wear damage [8-12]. In the classical tribology literature, this amplitude typically ranges from ~20-300 μm. Fretting wear is the loss or displacement of surface material on one or both opposing bodies that can result from fretting motion, if contact conditions are sufficient to produce it. The following can affect the magnitude of fretting wear between two contacting materials in a nuclear core fuel rod assembly:

  - Contact geometry of the opposing surfaces (dimples or springs against a clad rod)
  - The direction(s) of relative motion (linear, torsional (pivotal), radial, random or other)
  - Magnitude of the normal force on the contact, as affected by assembly stress, coolant flow, heat exposure, and other structural vibrations
  - Amplitude (stroke length) of the oscillations
  - Frequency of oscillation
  - Constancy of contact (continuous or intermittent with gaps and/or impacts)
  - State and composition of opposing surfaces (oxidized, coated, work-hardened, etc.)
  - The temperature of the contact – fuel rod temperature, friction heated, or both
  - The state of lubrication or fluid flow between opposing surfaces
  - The presence of third-bodies (wear debris, or CRUD)
  - Tribochemistry (effects of chemical reactions within the interface)
  - Hydrogen embrittlement (hydride formation from exposure to the environment)

In view of these potential influences, the challenge of modeling GTRF is daunting, and most laboratory-scale experiments in GTRF omit some factors seen in the actual operating conditions. The presence of adjustable variables, wear rate factors, and other empirical factors in existing GTRF models is a recognition that it is extremely difficult to know the synergistic effects between all the variables [2].

Fretting contact phenomena have been of interest for more than a century. For example it was a source of failure in mechanical fasteners on railroad rails, splines, bearings, and shaft couplings [8,13]. Numerous attempts have been made to formulate models to apply to GTRF. Such attempts tend to apply traditional disciplines like structural mechanics, computational fluid dynamics, materials science, and energy dissipative contact processes. Classical work in the field of fretting wear tends to use a combination of contact mechanics (macro- and micro-scale) and materials science.

Considering fuel rod assemblies of various design, one must recognize that GTRF can occur to varying degrees in some core locations but not others. In the current work, it seems most rational to apply the current model to a location that has greatest potential for producing a leaker. Predicting such locations in the assembly is not the goal of this subcontract. Rather it addresses the wear processes and rates that could occur in locations of greatest concern for producing leakers.

Overviews of the CASL/GTRF modeling challenge were published in 2011 [2] and updated in 2016 [3,6]. A discussion of the tribo-corrosion aspects of the GTRF problem was also presented in a chapter from a 2012 ASTM symposium proceedings [14]. The first version of the ORNL model for grid-to-rod fretting GTRF was developed by the Blau in 2012-2013 and published in *Wear* in 2014 [9].

The Engineering Wear Model (EWM) described here was developed based on the notion that the rate of wear of a complex materials system cannot *a priori* be assumed to remain constant from initial assembly to the end of its operating campaign. Therefore, the framework for the model enables the summation of increments of *wear depth into the cladding* in a series of stages whose rate of incursion differs depending on the evolving state of the materials [9]. The use of wear depth rather than wear volume, as is used in conventional wear models, was done to allow comparing the cumulative wear depth to a critical depth at which there are potential problems from subsequent cladding fracture, hydrogen embrittlement, or corrosion to produce a leaker. The four stages of the EWM for fretting include the following:

- Stage 0 = no wear, incubation period in which there is no tangential contact between grid and cladding
- Stage 1 = wear occurs in an oxide layer on the cladding
- Stage 2 = the oxide has been worn off and wear occurs in the substrate Zr alloy
- Stage 3 = hydrogen embrittlement increases the wear rate of the alloy

In general, the wear factor for each stage is expected to be larger than that of the previous one, but there is no reason why a reduction couldn't also take place if the severity of operating conditions was decreased. ORNL conducted preliminary fretting tests in D.I. water in an ambient environment to compare the wear of untreated and pre-oxidized Zr alloy cladding and showed that the wear rate in Stage 1 could be 1-2 orders of magnitude lower than that in Stage 2 [15].

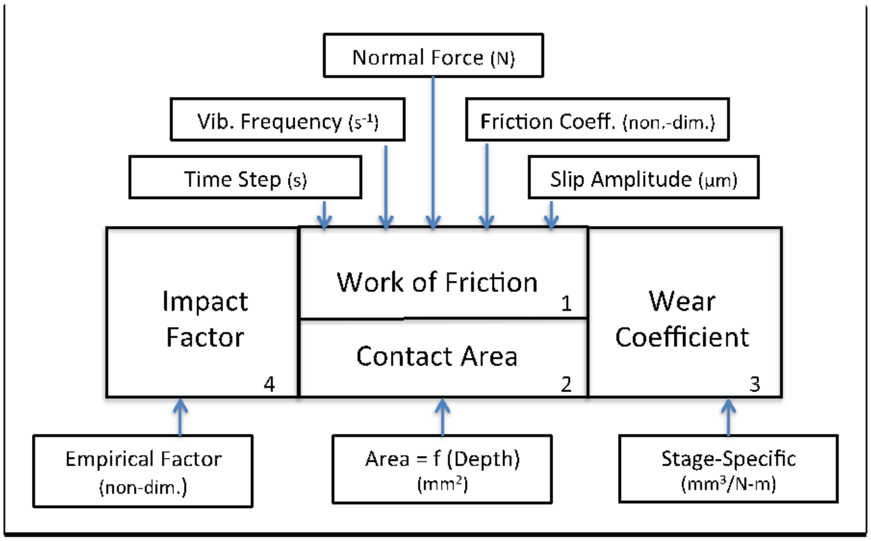

Figure 3. Block diagram of a stage in the GTRF EWM.

The basic structure of the EWM is presented in Figure 3. Inputs to the model include mechanical forces and motions obtained from other CASL modeling efforts, and it also includes information such as friction coefficients for the materials in contact as well as their wear factors that are obtained from the best available simulative experiments such as out-of-reactor tests.

Other than Stage 0 (incubation period), in which it is assumed that wear is zero or negligible, each stage reflects a conversion of the frictional work in the interface to the progressive loss of material. Contributions to the work of friction are shown in Figure 1 to comprise Block 1. This work is dissipated over an area of contact (Block 2). *The wear coefficient is effectively the efficiency by which a given amount of frictional work per unit area is converted to wear depth*. Block 4 is designed to adjust the rate of fretting wear, either to reduce or increase it, due to the presence of a gap between the grid and rod. As is discussed later, the presence of a gap may reflect a loss of contact for a period of time and the washout of debris from the interface. By contrast, if flow-induced vibrations cause more severe gap closure forces, then the impact contribution may increase wear damage.

The cumulative depth from each stage in the model can be written generally as follows:

$$z_t = z_0 + z_i = z_0 + \left(\frac{Fx}{A}\right) W_f \qquad (1)$$

where z_t = the total wear depth after time increment t, z_0 = the wear depth at the beginning of time increment t, Fx = the frictional work dissipated during time increment (i.e., average friction force F

times the sliding contact distance x), A = the average contact area over which frictional work is dissipated[i], and W_f = the wear factor.

For low-amplitude, oscillatory motion, sliding distance x, is given as follows:

$$x = 2\delta \upsilon t \tag{2}$$

where δ = the amplitude of fretting, ν = frequency of oscillation, and t = time of contact. As a cylindrical body wears, the area becomes a function of depth. Therefore, each increment is calculated using $A(z)$ for the prior increment of wear depth. The shape and length of the contact zone must be estimated in order to calculate A. This can be done by experimental measurements from out-of-reactor tests, like the VIPER test at WEC, from the literature, or based on an assumption about the scar shape.

In the first embodiment of the model, the wear scar was considered either to be a narrow rectangle or a slender ellipse of length a and width b. Fretting motion is assumed to take place in a direction cross-wise to the axis of the tube, i.e., parallel to the minor dimension of the rectangle or the ellipse. The equation for a chord of length w, and perpendicular distance z from the original circumference across a circular cross-section is:

$$A_{\text{eff}}(\text{z}) = Lw \tag{3}$$

where,

$$w = 2\sqrt{R^2 - (R - z)^2} \tag{4}$$

Clearly, the shapes of fretting scars affect the contact pressure distribution and will also depend on the initial contact geometry (e.g., a dimple or spring or strap). The shape depends on how wear progresses under forces acting in various directions during reactor operation. Therefore, consideration was given to other scar shapes in the course of this project. In general, the relatively small and concentrated initial contact (after assembly) creates the highest stress, and the nominal force per unit

---

[i] Note: At the onset of Stage 1 wear, the use of Eqn. (1) implies that initially there would be an extremely high or undefined value of (Fx/A) because at first $A_{initial} = 0$. This is not physically realistic, so the approach taken here was to compute $A_{initial}$ from the Hertz elastic contact width (w_H) under an assumed preloaded contact force to define the initial width and to assume a given a length of dimple or spring contact (L).

area decreases with time for two reasons: (i) spring force relaxation in the core environment, and (ii) widening area of contact due to wear.

In fretting damage, the scars are often rough, being composed of regions of stick and slip features, the differences in actual wearing contact within such zones would more than compensate for the slight errors arising from the shallow ellipse approximation. Actual GTRF assembly fretting wear scars from a publication by Kim [16] are shown in Figure 4. Approximation with ellipses seems reasonable for the scars on the left and right side (dimples), but approximation by shallow rectangular shapes seems a better choice for the center two scars (springs). This quasi-rectangular shape is also expected from a spring/dimple configurations discussed in more recent work by Lee and Kim [5]. The area versus depth relationships for various scar shapes, such those shown in (Fig. 5) were explored.

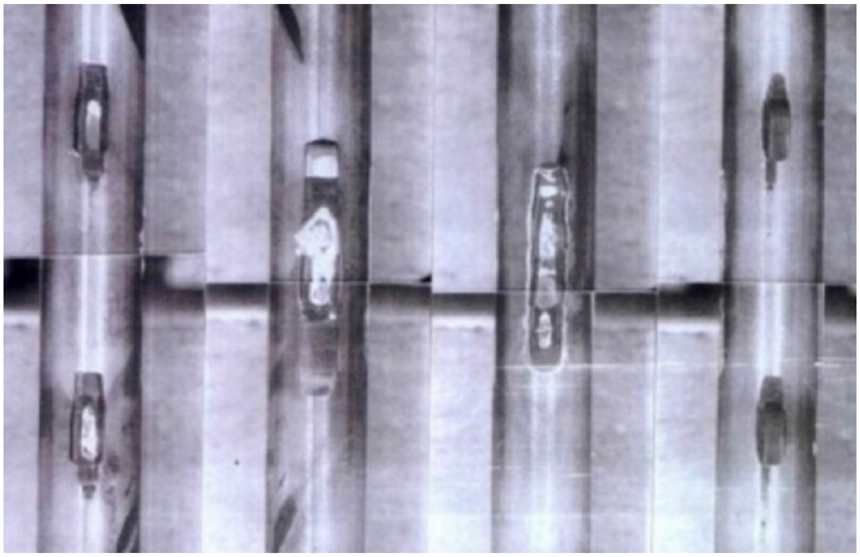

Figure 4. Example of fretting wear scar shapes, as reproduced from Fig 9. of Ref. [16].

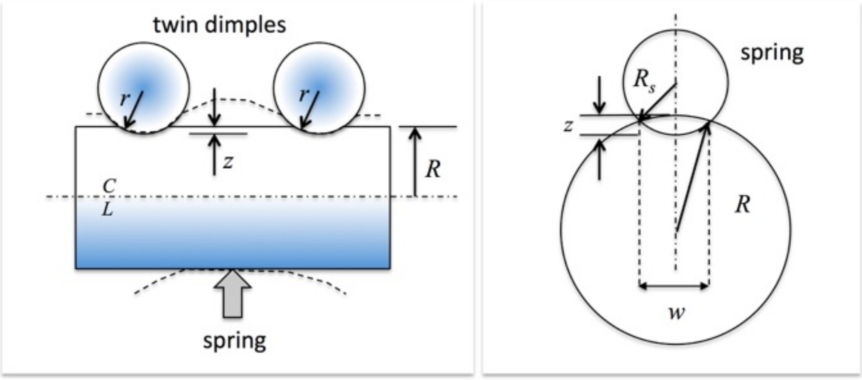

Figure 5. Twin dimple (left) and parallel axis cylinders (right) as possible contact geometries.

Six hypothetical wear scar shapes were investigated in terms of their area functions. These were:

Calculated cases:

- Plane-on-cylinder
- Twin spherical dimples-on-cylinder (Fig. 3, left)
- Twin cylinders with parallel axes (Fig. 3, right)
- The shallow ellipse approximation

Measured on analogs:

- Perpendicular crossed-cylinders
- Inclined crossed cylinders

In each case there was an attempt to simplify relationships to simple linear or polynomial curve fits. The plane-on-cylinder case was used in the original EWM. For a contact length of *L*, which is set by the length of strap that is lying across the cladding. The projected area ($A_p = Lw$) is based on the width of the wear scar (*w*) as a function of depth (*z*), see Eqn (4) above.

For twin spherical dimples lying along a tube axis, the projected area (A_p) as a function of depth can be accurately approximated by a simple linear relationship of the form:

$$A_p = b + c\,z \qquad (5)$$

For twin cylinders of two different diameters but having parallel axes, and of contact length (*x*), the projected area of contact versus depth is approximated well by:

$$A_p = x\,C\,z^n \qquad (6)$$

Frequently, elliptical fretting wear scars are observed, and the projected area is simply approximated by:

$$A_p = (\pi/4)\,x\,w \qquad (7)$$

where *w* can be calculated using Eqn. (4). Note that this relationship differs from a simple rectangular contact area by a factor of ($\pi/4 = 0.7854$), and this roughly 20% difference is likely to have less effect than uncertainty in the value of the kinetic friction coefficient (μ) in that term.

Using experimental analogs, the depth versus area relationships for perpendicular crossed-cylinders with different diameters can be represented by a linear expression such as Eqn. (7a). When the angle between the cylinders is other than 90 degrees, then the slope *c* increases. In the case of a

45 degree crossing, but with the same diameters as for the two cylinders at 90 degrees, the value of constant *c* increases by a factor of about 1.6, making area more sensitive to depth.

This earlier study addressed the calculation of the contact area used in the model (Figure 3, block 2) and how it can be represented based on variously-shaped wear scars. Four cases were considered. The more shallow the wear scar, the more simple can be the approximations of the contact area. A simple oval or rectangular shape seems to provide adequate accuracy to use linear relationships of depth to projected area. As the wear scar deepens or as the angle of contact between rod and grid becomes skewed relative to the cladding axis, the projected area differs more than a simple plane figure approximation. However, the errors associated with the geometric test cases, were relative small and the original approximation of a flat against a cylinder seems to be adequate for the purposes of this work.

The wear scars often show surrounding halos of grayish material, as evidenced in Figure 4 (especially for the scar on the far left), which is presumably the effect of accumulated debris. By assuming that the cylindrical counterbody that produced them has a radius *R* and wears not at all, it is possible to estimate the thickness of those layers around such an elliptical scar using the geometry shown in Fig. 6. Let w_1 = width of the overall wear scar and w_2 = width of the exposed bright metal substrate, both being parallel to the rod axis and the cylindrical counterbody lying perpendicular to the rod, then *h* can be calculated from wear scar dimensions transverse to the axis of the counterbody.

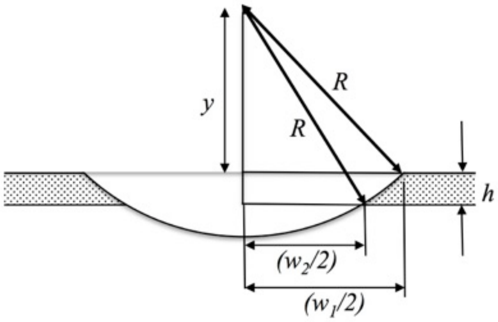

Figure 6. Estimate of the debris layer thickness h from wear-through into the substrate.

Equations (8) and (8a) show the simple Pythagorian relationships that can be used to solve for *h*.

$$R^2 = \left(\frac{w_1}{2}\right)^2 + y^2 = \left(\frac{w_2}{2}\right)^2 + (y+h)^2 \tag{8}$$

where $$y = \sqrt{R^2 - (\frac{w_1}{2})^2} \tag{8a}$$

and $$h = \sqrt{0.25(w_1^2 - w_2^2) + y^2} - y \quad (9)$$

For example, if the radius of curvature of the contacting feature on the spring happens to be R = 6 mm, and scar dimensions w_1 = 3 mm, and w_2 = 2 mm, then the thickness of the halo of material h = 0.106 mm. This is considerably thicker than any formed oxide layers, so the observed gray band is likely to be a deposit of debris.

The next section discusses the Engineering Wear Model in greeater detail, along with a brief literature review of fretting studies, modification of the EWM to account for the role of impact, an attempt to derive the fretting wear factor from metallurgy and materials science principles, a survey of applicable sliding and fretting wear factors reported in the literature, example cases for different assumptions about model variables, and finally, the initial use of wear data generated at ORNL on a simulative testing rig to improve model predictions and to account for temperature effects. Later, Section 4.6 documents modifications to the EWM based on autoclave fretting and impact rig (AFIR).

2. FRETTING RESEARCH AND THE ENGINEERING WEAR MODEL

In general, fretting-related research can be divided into four categories:

1) *Structural modeling* (mechanical engineering approaches that attempt to predict localized fretting motions and contact forces, including forced or harmonic vibrations and damping)
2) *Contact mechanics modeling* (stress, strain, and slip behavior in or near a fretting contact and having a defined macro-scale and/or micro-scale geometry)
3) *Basic (generic) experimental, materials-oriented fretting studies* (using simple contact geometries like a sphere or cylinder oscillating against a flat surface)
4) *Applied experimental work and fretting wear modeling* (using contact conditions that simulate application-specific geometric applications and environments, like GTRF)

In order to account for the localization of damage accumulation and the process of debris generation, the wear factor derivation defined a “wear process volume” (WPV) in which there has been cumulative, irreversible damage to the material. Depending on the severity of contact conditions, the WPV may include any or all of the following volumes of material: (i) a third-body layer of debris particles (TBL), (ii) a highly-deformed near-surface layer from which new debris is created (HDL), and (iii) an extended deformation zone (XDZ) below the HDL. Together these zones dissipate frictional work. Some of that work is converted onto heat or sound.

In early stages of contact, the cladding may be covered by a thin (~ several µm thick) oxide that protects the alloy until it wears off to expose a more ductile substrate whose response to fretting allows an HDL to form. The derivation presumes that each sub-zone within the WPV dissipates energy by utilizing a combination of deformation and fracture. The available frictional work is thus partitioned. Depending on the stage of wear and the microstructures of the material pair, that partition can change. Figure 7 depicts schematically how the work of friction could be partitioned.

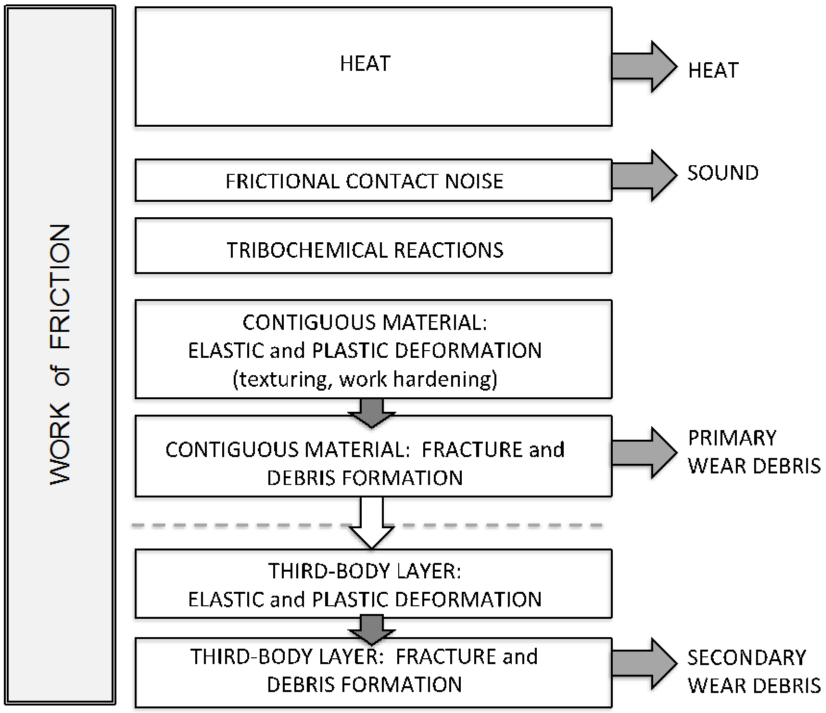

Figure 7. Partition of frictional work without an impact contribution – fretting only.

As shown in Figure 7, two possible routes for debris generation and mass loss were considered. *Primary wear debris* originates in the HDL. Consisting of fine particles of metal or oxide, it may be directly expelled from the contact under the oscillatory motion of fretting, or it may be agglomerated and compressed into a third-body layer (TBL) which subsequently breaks off into what will be called *secondary wear debris*. In either case, wear must be considered to be the net result of incremental debris loss events. The cumulative effect of countless discrete events is approximated by an average wear rate in traditional linear models. The morphology and movements of the freed debris depend upon (i) the initial size of pre-existing flaws in the microstructure (herein defined as debris embryos, DEm), (ii) the DEm density within the debris forming layers, (iii) the mode of deformation and critical crack length within the WPV, and (iv) the probability that a given debris embryo will produce an average-sized wear particle on each oscillation, given the material and form of wear that is involved.

To be consistent with the EWM, the units for the derived wear factor were based on the volume lost per unit distance slid per unit of normal force (mm^3/N-m). This wear factor is also commonly used in the literature of sliding wear research, but in this case, it was derived based on which stage of GTRF wear was underway. [Note: Other investigators in this project and in the literature use the reduced units of Pa^{-1}, which can simply be converted to mm^3/N-m by multiplying by 10^9.]

There were eight assumptions used in deriving the wear factor. In summary, they were:

1) A focus on fretting as the primary process that produces material loss
2) Focus on the cladding wear rather than the grid wear
3) Incremental nature of wear loss being approximated by a characteristic rate
4) Scale of microstructure such as oxide thickness, grains, sub-grains, and dislocation cells
5) Effects of fretting-induce deformation on the microstructural elements
6) Constancy of conditions during the wear stage of interest
7) Effects of third-bodies, such as debris and agglomerated material
8) Changes in the wear process and related mechanisms of damage

Schematically, wear particles can be generated from a series of zones shown in Figure 8 and Progressive changes in each part of the WPV are summarized in Table 1. In terms of its mechanical properties, one can visualize the WPV as a stack of three zones that vary in shear strength and in the ability to dissipate frictional work. During running-in the initial oxide wears off, then the HDL forms, and finally the XDZ forms below it while the TBL grows in thickness as it covers the surface of the HDL.

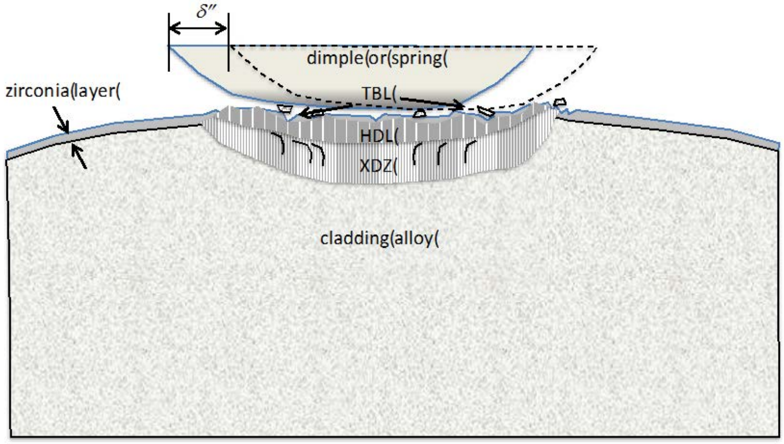

Figure 8. Indicating the development of damage zones due to fretting contact.

Table 1. Comparison of initial and steady-state conditions of three zones

Zone	Early state	Steady-state
TBL	surface oxide wears away and the roughness changes on the counterbody and the wearing body, but other than oxide detritus, there is little wear debris available to develop a TBL	a layer of compressed or mechanically-mixed debris particles has formed from the wearing surface and possibly from the counterbody; the TBL may be patchy or continuous, and loose particles may break off and be expelled from the wearing interface
HDL	a thin, highly sheared, near-surface layer begins to form due to tractions imposed by the counterbody	a highly-deformed, work-hardened layer with a preferred orientation; it may contain lamellar features and micro-cracks that can lead to debris detachment; tends to reach a nominal thickness after run-in; as wear occurs, the HDL progresses into the XDL and maintains a nominal thickness
XDZ	no deformation occurs below the HDL until the HDL workhardens fully and begins to transfer shear force deeper into the surface	plastically-deformed region with a gradient of deformation below the HDL; may contain bent grain boundaries (partial texturing) and/or deformation twins, with hardness increasing toward the HDL boundary.

The wear factor (W_f) is a measure of the efficiency of transforming a quantity of frictional work, generated by rubbing the cladding upon the grid (dimple or spring) for a period of time at a given normal force and friction coefficient and at a set amplitude and frequency, into a volume of loose wear particles. Wear particles originate at debris embryos (DEm) within the boundaries of the wear process volume (WPV).

The simplest form of the wear factor contains the effective shear strength of the material within the wear process volume (τ_{eff}), the number of particles released per stroke (N_p), and the ratio of the mean debris particle size (L_0) to the thickness of the WPV (η) whether the latter consists of the TBL, HDL, or both.

$$W_f = \frac{b}{\tau_{eff}} N_p \left(\frac{L_0}{\eta}\right) \tag{10}$$

Here, b = a units correction, and the factors in Eqn. (10) can be rationalized as follows:

- W_f increases as the resistance to shear of the WPV (i.e., τ_{eff}) decreases. The effective shear strength is a composite value that reflects the properties of the layers that comprise the WPV.

These layers include the TBL and the HDL and are analogous to electrical resistances in parallel.

- The number of debris particles produced per stroke (N_p) is proportional to the probability that some fraction of the debris embryos within the WPV is greater than the critical crack length to initiate a loose debris fragment.
- The larger the debris size relative to WPV thickness, the higher should be the incremental wear rate. If the debris consists of flat platelets, as in a delamination-type of wear, this ratio could exceed 1.0, but normally for tiny fretting debris particles (L_o/η) is expected to be << 1.0.

The constant b is the conversion from N-mm in the denominator to N-m so that the units of W_f are consistent with conventional wear factors in the literature. The following are the units are suggested based on the form of Eqn. (10):

$$\frac{mm^3}{N-m} = \frac{(1000.{}^{mm}/_{m})}{\left({}^{N}/_{mm^2}\right)} (number\ of\ particles) \frac{(mm)}{(mm)} \tag{11}$$

Most of the quantities in Eqn. (11) can be measured or estimated based on the microstructures of the materials or oxide layer dimensions, but there is a considerable uncertainty in the probability that debris embros will be larger than the critical crack size, and critical crack size for wear is not feasible from Rosenfield's previous analysis of the problem [17].

In order to test this model, it was necessary to make a number of estimates of the quantities in Eqn. (10). A summary of two cases in which W_f was back-calculated from collected data and presented in Table 2 and displayed in Figure 9.

Table 2. Quantities Used in Trial Calculations of Wf (mm3/N-m) using WEC Estimates

Quantity (Symbol)	Value and units	Comments/Basis
Normal force (*P*)	0.50 N 0.25 N	VITRAN calculations from WEC
Friction coefficient (μ)	0.12 (non-dim.)	Boundary lubricated sliding
Friction force (*F*)	0.06 N 0.03 N	$F = \mu P$ using *P* above
Area (*A*)	3.142 mm^2	area of an ellipse 4 mm long,1 mm wide
Frequency of sliding (ν)	30 Hz	first natural frequency of a fuel rod, per Ref. [9].
Amplitude of oscillation (δ)	10 µm	suggested amplitude (R. Lu, WEC)
Sliding distance in 1 mo. (*x*)	1.58 x 10^6 mm	$x = 2\delta\nu t$ (t = 2,628,288 s)
Friction work / area	94.6 N-m/mm^2 47.3 N-m/mm^2	for *P* = 0.5 N for *P* = 0.25 N

Using shorter fretting amplitudes, but with the same frequency of oscillation. means that the sliding distance per unit time is reduced. Using lower normal force means that the frictional work per unit area is reduced. Therefore, to produce the same depth of wear, the efficiency of converting the available frictional work into wear volume, as expressed in W_f , would need to be increased. This is reflected in the plots in Fig. 9, which use a 0.5 and 0.25 N normal force (left and right, respectively) with 10 µm fretting amplitude. Wear rates at that are higher than about 10^{-5} mm^3/N-m seem unreasonably high, therefore, minimum wear-to-depth times of at least several months for a 0.5 N load and over a year for a load of 0.25 N load seem more reasonable.

Using the case of 0.25 N in Fig. 9 as an example, in order to reach a wear depth (*z*) of 2 µm in 1 month translates to a wear factor of about 6.5 x 10^{-5} mm^3/N-m.

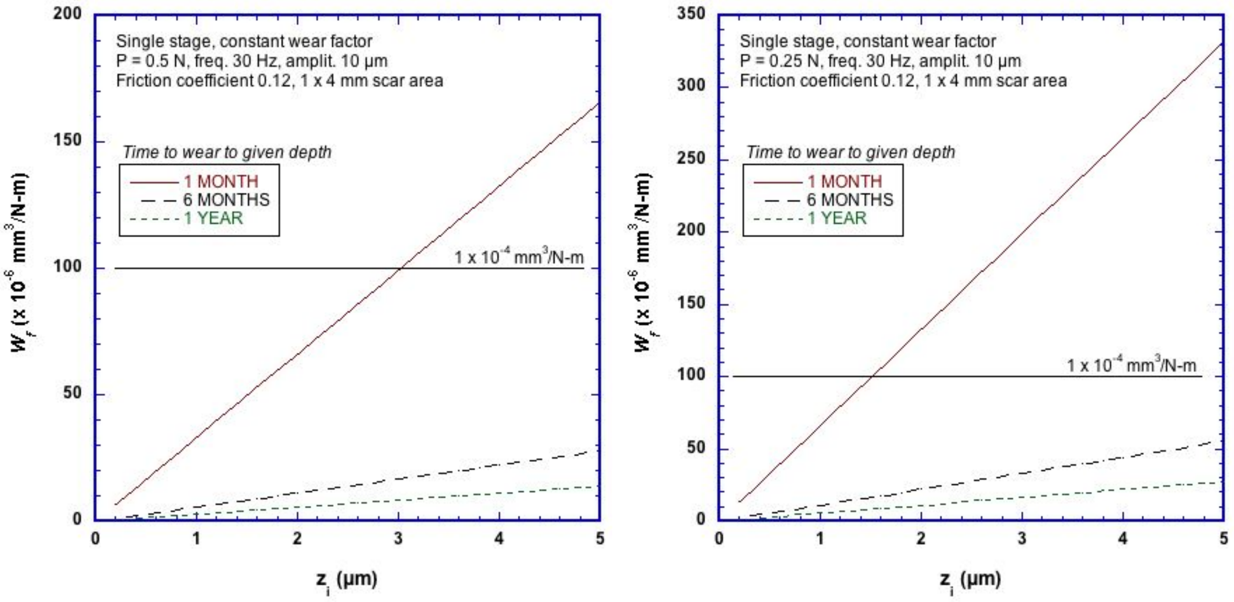

Figure 9. Calculated wear factors based on WEC values under 0.5 N (left) and 0.25 N (right).

While the proposed model for the wear factor depends on difficult-to-determine microstructural parameters, its concept seems physically reasonable. Thus, using experimental data may enable back-calculation of some of the more obtuse microstructural characteristics, like the probability of wear particle nucleation in the wear process volume.

2.1 Evaluation of the EWM for different conditions

This section summarizes the wear depth calculations compared based on a series of assumptions about the cladding oxide films and the case where the normal force decreased as a result of spring relaxation. These five cases were as follows:

- Case A. Pre-oxidized surface with low friction coefficient
- Case B. Pre-oxidized surface with exponentially decreasing normal force
- Case C. Thin-oxide with exponentially decreasing normal force
- Case D. Three stage model with pre-oxidized surface and exponentially decreasing normal force
- Case E. Effects of amplitude and frequency

Table 3 summarizes the input quantities used in each case. Figures 10 and 11 plot the results of these calculations, respectively (A-D in Fig. 10a – 10d, and E in Fig. 11).

Table 3. Input Variables Used in Test Cases of the Engineering Wear Model

Symbol (units)	Case A	Case B	Case C	Case D	Case E
L (mm)	3.0	3.0	3.0	3.0	3.0
P (N)	0.5, 1.0	1.5 to 0.5 in 30 days***	1.5 decreases to 0.5 in 30 days; remains 0.5	1.5 decreases to 0.5 in 30 days; remains 0.5	1.5 decreases to 0.5 in 30 days; remains 0.5
t_{inc} (s)	86,164. (1 day)	86,164. (1 day)	86,164. (1 day)	430,820. (5 days)	86,164. (1 day)
t_o (days)	30	30	30	30	30
t_{op} (days)	90	90	90	545 (18 months)	90
w^* (mm)	0.0195	0.0195	0.0195	0.0195	0.0195
W_f (mm^3/N-m)	5 x 10^{-7} ; 5 x10^{-6}	5 x 10^{-7} ; 5 x10^{-6}	Stage 1: 5x10^{-7}	Stage 1: 5x10^{-7}	Stage 1: 5x10^{-7}

			Stage 2: 3x10^{-5}	Stage 2: 3x10^{-5} Stage 3: 6x10^{-5}	Stage 2: 3x10^{-5}
z_o* (µm)	1 x 10^{-2}	1 x 10^{-2}	1.0	--	1.0
z_{ox} (µm)	4.0	4.0	1.0	2.0 or 3.0	1.0
μ (non-dim.)	0.15**	0.15**	Stage 1 = 0.15 Stage 2 = 0.40	Stage 1: 0.15 Stage 2: 0.40 Stage 3: 0.50	Stage 1: 0.15 Stage 2: 0.40
δ (µ□□	25	25	25	25	12.5, 25.0, or 50.0****
ν □□$^{□□}$□	30	30	30	30	15, 30, or 60****

* Based on Hertz contact at an assembly preload of 5 N.

** Water-lubricated oxide, boundary lubrication.

*** Exponential decay of the load as $P(t) = P_o e^{-At}$

**** depending on *K* that multiplies the product or the amplitude and frequency by a constant to test the effects or either variable. That is sliding distance in the numerator of the EWM, x = *K* (2δ*vt)*

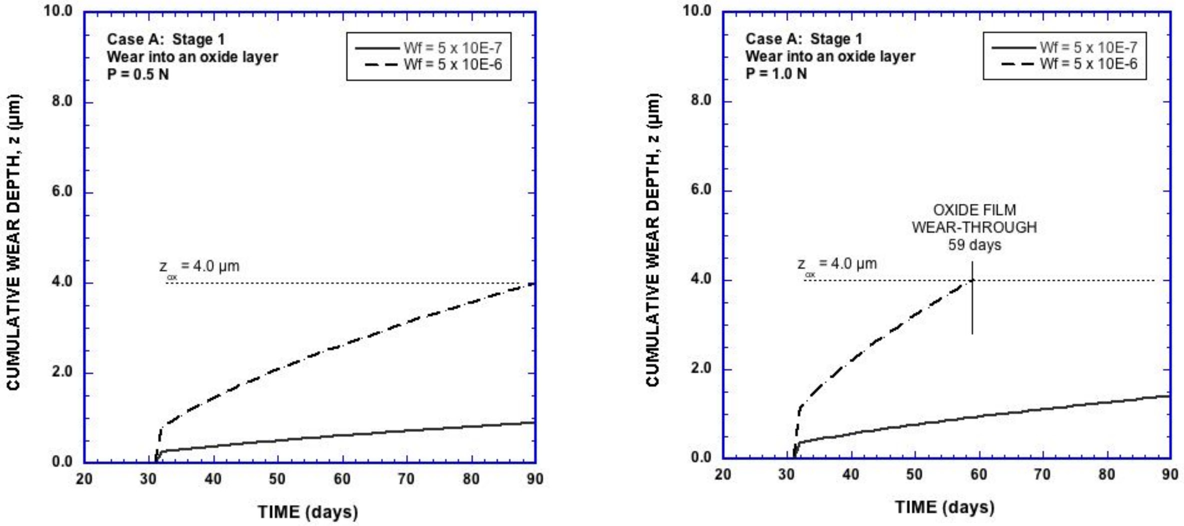

(a) CASE A (b) CASE B

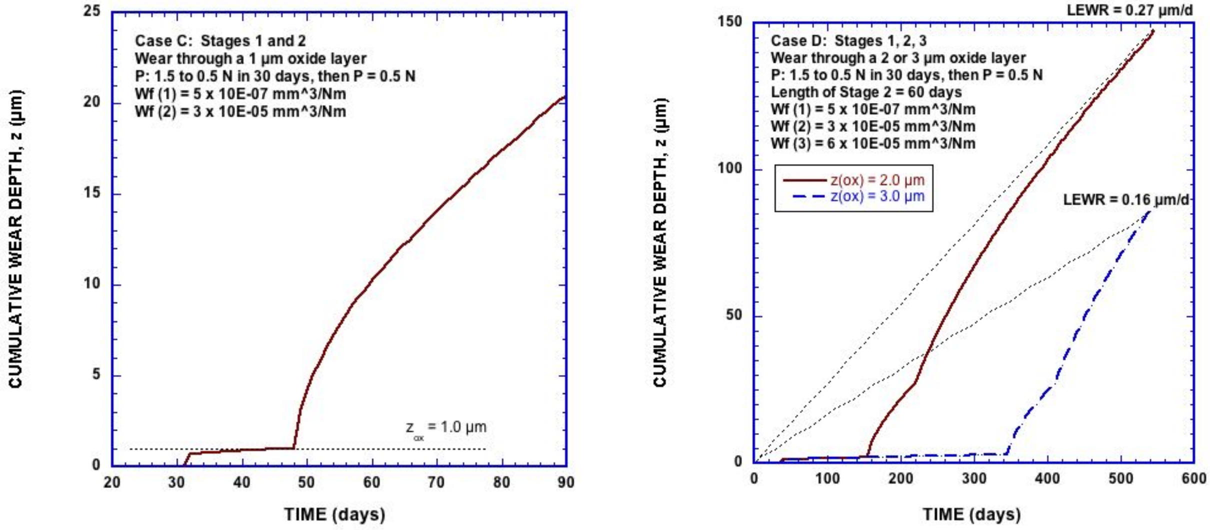

(c) CASE C (d) Case D

Figure 10. (a-d) Results of test Cases A-D respectively. LEWR is defined for Case D as the linear equivalent wear rate obtained simply by scaling the cumulative depth to the end of the period of contact accounting for no transitions or changes in wear during different stages.

ORNL conducted a series of simulative tests using their new autoclave fretting rig during May-August 2017. These are discussed more fully in Section 4, but one of the parameters measured on cladding specimens was the maximum depth of wear. It is interesting to compare the range of maximum wear depths measured in ORNL experiments under pressurized water at 0.5 N load, at 204 ^{o}C and at about 20 Bars pressure to those for the test cases plotted in Figure 8.

As-received Zr on as-received Zr:	8.7 – 16.0 µm (average 12.4 µm)
Pre-oxidized Zr on As-received Zr:	3.8 – 5.1 µm (average 4.5 µm)
As-received Zr on pre-oxidized Zr:	6.1 – 10.3 µm (average 8.2 µm)
Pre-oxidized Zr on pre-oxidized Zr:	2.4 – 4.0 µm (average 3.2 µm)

Clearly, case studies A-E were in the ball-park in terms of the ORNL wear depth data collected recently.

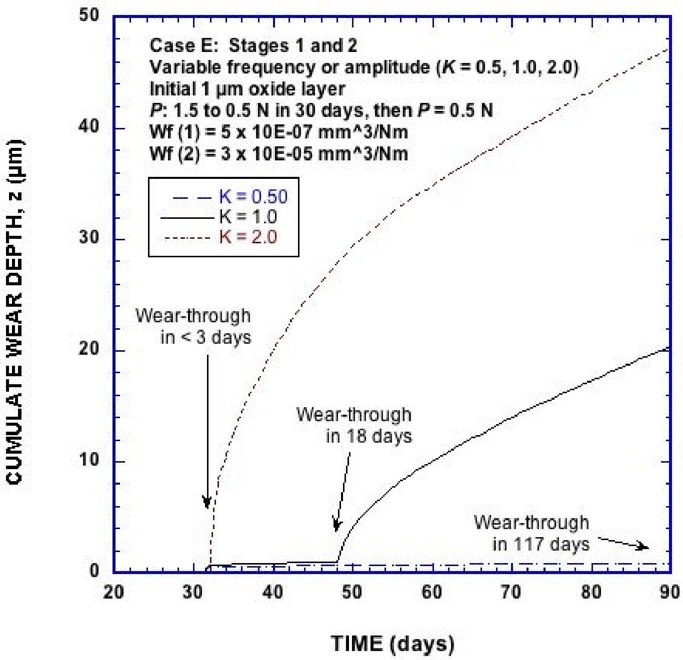

Figure 11. Calculated wear depth for CASE E. Since the EWM implies a linear relationship of the amplitude and frequency of fretting to the cumulative wear depth, Case E shows the effects of multiplying either the frequency, amplitude, or their product by some factor (K).

The summary of the case studies were as follows:

- The length of stages 0 (incubation period) and 1 (oxide film wear) have a major influence on the final wear depth prediction using the EWM
- Doubling the wear rate between Stages 2 (substrate wear) and 3 (embrittled alloy wear) has much less effect that the effects of Stage 0 and 1, because both of them essentially off-set the transition in time that reflects a change to the higher wear rate.
- The introduction of a linear effective wear rate (LEWR) enables a simplified comparison of multi-stage model wear depths a specific operating time. Rates for this exercise range from negligible (~ 0.01 µm/d) to over 0.5 µm/s.
- More accurate fretting wear coefficients are needed for embrittled Zr-4 to improve predictions, and these will be forthcoming from further experiments at ORNL.

2.2 Impact of Fuel Rod – Grid Gaps on the EWM

A light water reactor fuel rod bundle consists of thousands of individual fuel rods, each composed of pellets encased in zirconium alloy cladding and each supported at several locations, including periodic lattice-like supports (grids with springs and dimples). Therefore, the number of potential locations for GTRF to occur may be hundreds of thousands. As a result of thermo-physical and dimensional changes that occur during the operation of the reactor, the forces on individual contacts can change. The likely locations of highest contact stress in a model core assembly have been calculated by other members of the CASL team as described in Sect 3. Similarly, examination of field and out-of-reactor test components indicates that not all grid to rod locations exhibit the same degree of GTRF wear and that the most tribologically-active locations can change over time. Building a predictive GTRF model can focus on both (a) a meso-tribosystem consisting of an individual dimple- or spring-to-rod contact and (b) a macro-tribosystem that addresses the probabilities of GTRF occurrence throughout the bundle and the likelihood of leakers at different places and times. The current EWM focuses just on one location, presumably the most critical in the assembly in terms of wearing through to produce a leaker.

Most fretting wear models found in the literature assume constant contact over time (i.e., no separation of the surfaces). This assumption makes it easier to predict cumulative wear loss based on a constant wear rate under continuous contact, or by summing up energy dissipation during a given number of strokes. However, in rod bundles, gaps occur between grid-rod contacts for a variety of reasons. This report will not address their causes other that to mention possibilities like thermal expansion, relaxation of assembly stresses, rod creep, swelling, and support point shifting within the rod bundle. The net effects are:

1) Individual grid/rod locations are not in rubbing contact at the time of start-up, but do make contact later at which time fretting begins.
2) Individual grid/rod locations may begin with a loaded contact but experience separation later, the gap opening and closing being intermittent or periodic
3) Gaps may become 'permanently' open after some period of operation, at which time GTRF wear is halted.
4) Some combination of the above.

The net effect of most of the foregoing cases is to prolong the wear process at a given contact point by reducing the fraction of time in which frictional or impact contact occurs relative to the total time of operation (i.e., a duty-cycle effect). However, there is one special case – relatively severe impact – in which the damage from fretting is made worse by impact during gap closure. Structural vibrations would have to be relatively severe in order for such impact damage to be a major synergistic contributor to the overall wear rate.

Some of the foregoing cases are easy to implement in the EWM, but others are not. For example, case (1) above can be accommodated by setting the length of Stage 0 of the model where there is no oscillating contact between surfaces and hence no wear. Stages 1, 2, and 3 then follow and continue uninterrupted until the end of the fuel cycle or to the point of cladding wear-through. If, as in case (2), the contact begins to fret, but is periodically interrupted, there are several approaches to be taken and that is perhaps the most complex situation.

Table 4. Possible Gap Scenarios and Implications for the EWM.

Scenario	Physical situation	Implications for the EWM
(a) Gap is open at the start of operation	No rubbing or impact – coolant flows between rod and grid	Stage 0 – no wear occurs.
(b) A gap forms after a period of fretting contact, remains open thereafter	Fretting wear stops. Any remaining wear debris is carried away or displaced by flowing coolant downstream of the contact.	The cumulative wear depth (*z*) at that location from one or more stages of wear remains constant after the gap opens.
(c) A gap forms periodically and fretting continues when contact occurs	(i) Any trapped wear debris is released and washed out of the wear scar area. (ii) During gap opening, the coolant flow into the	The current wear stage is interrupted. Additional fretting depth increments are scaled in proportion to the fraction of total time in which the gap is closed.*

	converging gap creates pressure that holds the rod and grid apart and counteracts the mechanical gap closing force from springs.	The pressure from coolant flow through the narrow gap reduces the normal force on the contact, and reduces the wear rate.
(d) A gap forms and repeatedly closes with significant impact force	Fretting damage is exacerbated by added damage due to impact as the gaps close. Impacts could potentially damage beneficial oxide layers, loosen debris, and accelerate the fretting process.	Reduction in wear rate due to loss of fretting contact may be offset by the damage created as the gap closes. Thus, the impact factor in block 4, Fig. 1 can range from 0 to <1 if there is reduced wear, but >1 if the impact damage adds to the fretting damage.

* Note: This presumes that steady-state wear for this stage resumes immediately and there is no transient process that occurs immediately after the gap closes (re-wear-in).

There are certain physical implications of gaps as they affect the EWM. These remain to be tested and verified, but they seem reasonable based on previous observations and a consideration of the behavior of a flowing coolant through a confined gap. Table 4 summarizes them. The second column describes the proposed physical situation and the third column, how that situation would be implements in the multi-stage model.

3. STRUCTURAL MECHANICS MODELING

A major challenge in GTRF modeling is that although the key physical processes of contact, friction, sliding, and wear take place at discrete locations of sub-millimeter dimensions, the forces driving fuel rod vibration are due to turbulent coolant flow along assemblies of rods of multiple-meter scale. In turn, the scales of turbulent eddies driving rod vibration span a wide range of lengths and frequencies, forcing the relative motion of grid/cladding sites in a highly non-periodic manner. Design features enhancing heat transfer in fuel assemblies by promoting turbulent coolant flow can provide important performance advantages, but the magnitude of turbulence-induced rod vibration must be limited in order to avoid excessive GTRF wear.

A number of different activities have been performed within CASL to assess the structural mechanics aspects of the grid to rod fretting challenge problem. In particular, these activities have successfully demonstrated

3.1Modeling Gap Development

Figure 12a) shows the geometry and mesh of the spacer grid and the cladding tube. Figures 12b), 12c), and 12d) show the front and lateral views of one side of the spacer grid. Likewise, Figure 13 shows a schematic illustration of the arrangement of the springs and dimples on the inside of the spacer grid in 3 dimensions [18]. Each side of the spacer grid has a length of 38.1 mm, width of 12.776 mm, and thickness of 0.229 mm. The spring and dimple dimensions can be inferred approximately from Fig. 12. The cladding tube has an outer diameter of 9.5 mm and an inner diameter of 8.357 mm, with a length of 38 mm. The length of the fuel rod assembly (along the axial direction) represents the unit cell configuration of the springs and dimples on the spacer grid which repeats periodically every 38 mm. Each side of the spacer grid is comprised of 6044 finite elements and the cladding tube is comprised of 23370 finite elements, so that there are a total of 47546 elements in the assembly. Finite elements with reduced integration (C3D8R) are used in ABAQUS.

The bottom rim of the cladding tube is constrained in the axial (***z***) direction but allowed to expand or contract radially. The bottom corner nodes of the spacer grid are constrained in all degrees of freedom to prevent rigid body motion. The initial configuration of the cladding tube and the spacer grid is such that the former is held by the latter via hard contact conditions between the cladding tube and the springs and dimples on the spacer grid. In order to model these interactions, the nodes on the cladding tube mesh and the spacer grid mesh are overlapping initially at regions where the springs and dimples are in contact. These overclosures are resolved prior to irradiating the assembly using the SHRINK parameter in ABAQUS, which automatically displaces the spacer grid and induces initial contact stresses in the elements.

In this effort on modeling gap opening, there was no attempt to model the effect of coolant flow-induced vibrations and forces on the clad-spacer grid system. Rather, our goal is to understand the evolution of contact forces and gap opening during irradiation. Such evolution is due to irradiation creep and irradiation growth of clad and spacer grid driven by the axial and circumferential stresses induced by pressure.

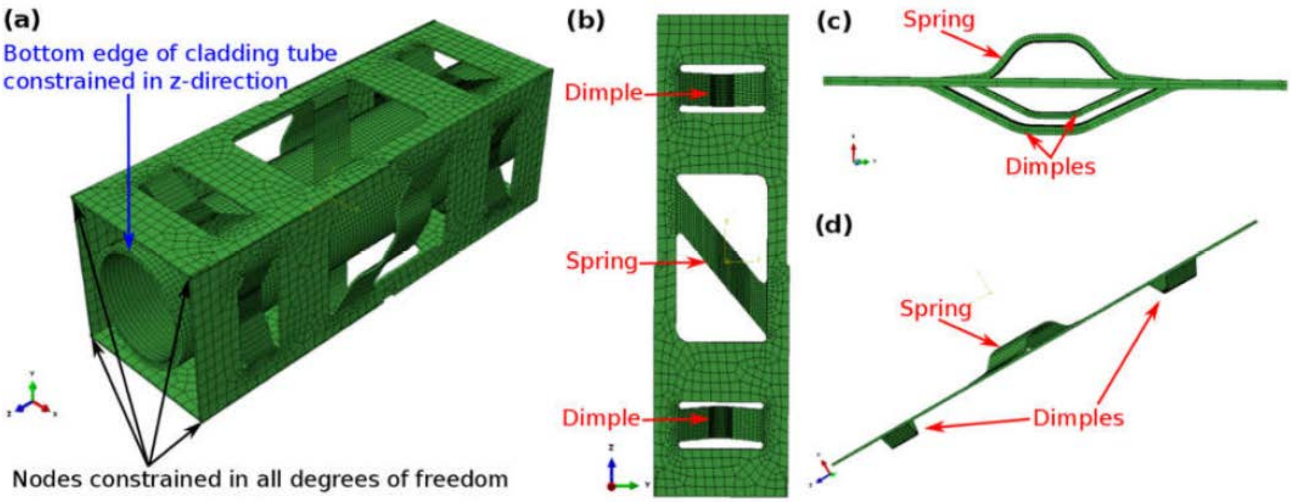

Figure 12. a) Mesh and boundary conditions for the clad – spacer assembly, b) front view of a side of the spacer grid, c) and d) lateral views of a side of the spacer grid.

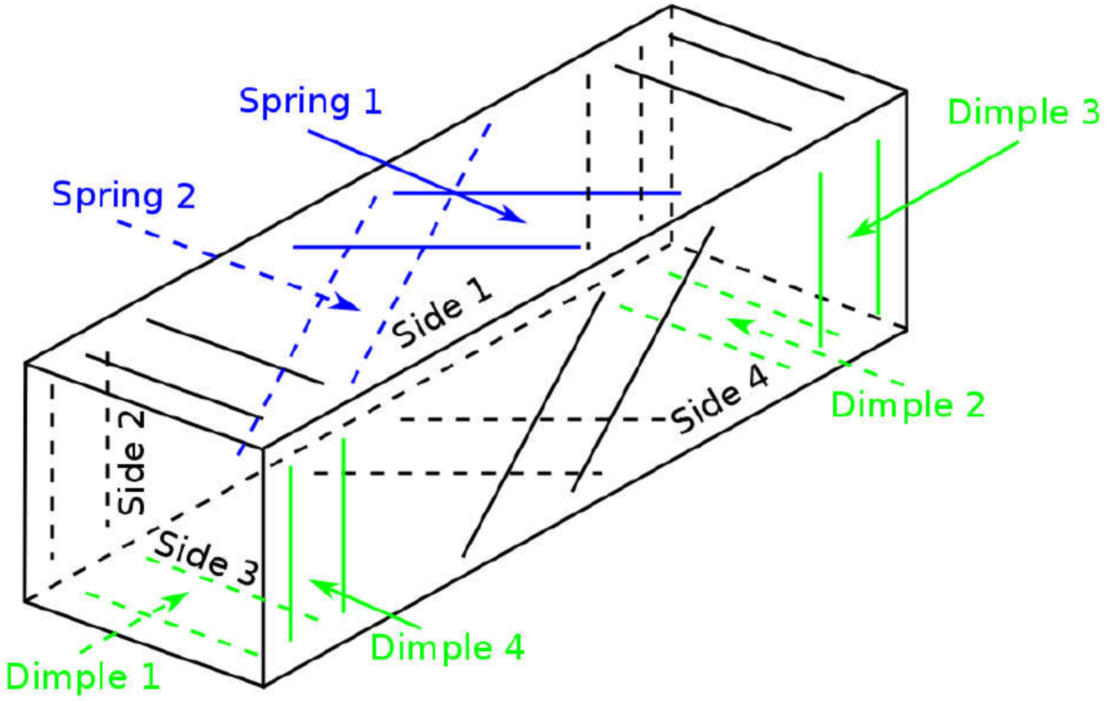

Figure 13. Schematic of the spacer grid showing the springs and dimples on the spacer grid. Only the springs (in blue) and dimples (in green) on the inner sides of the grid are labeled.

Finite element simulations are computationally expensive, especially when the material model calculations are performed at the level of grains using a visco-plastic self-consistent (VPSC) model for the stress – strain constitutive behavior. A strategy to minimize the computational cost is to represent the texture using the minimum number of crystal orientations that will predict (within a 10% deviation margin) the same mechanical response of the aggregate as would be obtained if using the whole set of orientations. Concerning the cladding tube, we have adjusted our growth model [20] to dislocation density evolution reported by Holt et al. [19] for an irradiated Zircaloy-2 tube of which we do not have the discrete texture (their Fig. 16c): basal pole figure of Chase Tube 002). As a consequence, we have used here an available tube texture of a cold-worked Zircaloy-2 cladding tube comprising 1144 orientations which has similar Kearn factors as those reported by Holt et al. [19]. From this texture, a reduced texture of only 7 orientations was derived. As for the spacer grid, a reduced texture comprising 13 orientations was derived from an initial texture of 2428 orientations (the latter texture was measured using diffraction scans from the cross-section of the spacer grid springs at Oak Ridge National Laboratory, Oak Ridge, USA). Figure 3 shows the basal pole figures for the original and the corresponding reduced textures for the cladding tube and spacer grid used in our simulations. In reducing these textures, we enforced the Kearn factors of the reduced texture to be the same as those of the original texture. Kearn factors are defined as the second order moments of the basal poles, i.e.,

$$F_i = \sum_g w^g \left(r_i^g\right)^2 \tag{12}$$

where, w^g is the weight, and r_i^g is the direction cosine of the c-axis of the i^{th} component of the g^{th} orientation. Reduction of texture and resulting irradiation creep response of the polycrystal has been discussed in detail in Ref. [20]. Kearn factors of the cladding texture in Fig. 14a) are: F_{axial} = 0.0864, F_{hoop} = 0.5232, F_{radial} = 0.3903, and those of the reduced texture in Fig. 14b) are identical. These factors are close enough to the ones reported by Holt et al. [19], which are 0.06, 0.49 and 0.45, respectively. Kearn factors of the spring texture in Fig. 14c) are: $F_{rolling}$ = 0.1907, $F_{transverse}$ = 0.1102, F_{normal} = 0.6991, while that of the reduced texture in Fig. 14d) are: $F_{rolling}$ = 0.1851, $F_{transverse}$ = 0.1051, F_{normal} = 0.7098. As demonstrated in Appendix A, irradiation growth and creep calculations performed using the reduced cladding texture compare well with experimental trends for cold-worked Zircaloy-2.

Note that the texture shown in Fig. 14b) is the same for every element in the cladding tube when expressed along the radial, hoop, and axial directions of the tube. However, because the simulation geometry and FE computations are expressed in the laboratory Cartesian coordinates, the texture is rotated to laboratory axes for each FE comprising the cladding tube. Similarly, the texture shown in Fig. 13d) is along the normal, transverse, and rolling directions of the rolled plate used to form the spacer grid, and is appropriately rotated to the laboratory axes for the FEs comprising each of the four sides of the spacer grid.

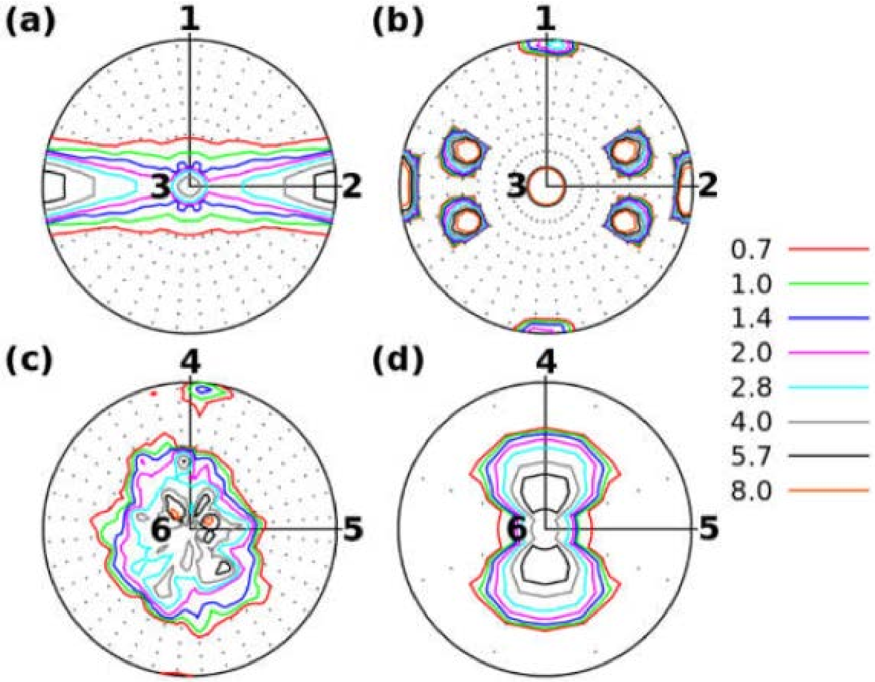

Figure 14. Basal pole figures for cladding tube texture a) with 1144 orientations, b) with 7 reduced orientations, and for the spring texture c) with 2428 orientations and d) with 13 reduced orientations.

- **<u>Distribution of pressure in springs and dimples</u>**

Figure 15 shows the distribution of pressure in the springs and dimples on the spacer grid for various radiation doses. The maximum and minimum pressures for each of these contours is also specified. Sides 1, 2, 3, 4 and 1 are contiguous to each other. Further, the elements of the spacer grid in contact with the cladding tube are: spring 1 on side 1, spring 2 on side 2, dimples 1 and 2 on side 3 (bottom to top), and dimples 3 and 4 on side 4 (top to bottom). This is schematically described in Fig. 15 to aid the interpretation of simulation results.

The cladding tube-spacer grid assembly was uniformly irradiated at a rate of 10^{-7} dpa·s^{-1}. A pressure of 15.5 MPa was applied on the outer surface (representative of the coolant pressure), and a pressure of 10 MPa was applied on the inner surface of the cladding tube. The latter value is a first order approximation of the plenum pressure experienced by the fuel rod over the entire duration of the burnup in the range 6-15 MPa (cf. [21-23]). While no further external load was applied on the spacer grid, the pressure differential induces both, hoop and axial stresses. Further, the material model used for cold-worked Zircaloy-2 was calibrated to the experimental irradiation growth data at 550 K from Ref. [19] (cf. [24]). Note that we have neglected the effects of thermal creep on the deformation behavior of Zircaloy-2 as it contributes second order effects in comparison to irradiation growth and creep at these relatively low homologous temperatures. Moreover, we have not modeled the fuel pellets in our FE simulations, which may contribute indirectly to the cladding-spacer grid interactions by impinging on the inner surface of the cladding tube. At the specified dose rate, a radiation dose of ≈ 3.15 dpa is accumulated over one full power year. This implies that 10 dpa corresponds to ≈ 3.2 power years and 20 dpa corresponds to ≈ 6.4 power years.

The stresses on the spacer grid shown in Fig. 15 are induced primarily due to contact between the cladding tube and the springs and dimples. The stress concentration induced at the corners of the springs and dimples that are not in contact with the cladding tube are second order effects and are not expected to influence the gap opening between the spacer grid and the cladding tube significantly.

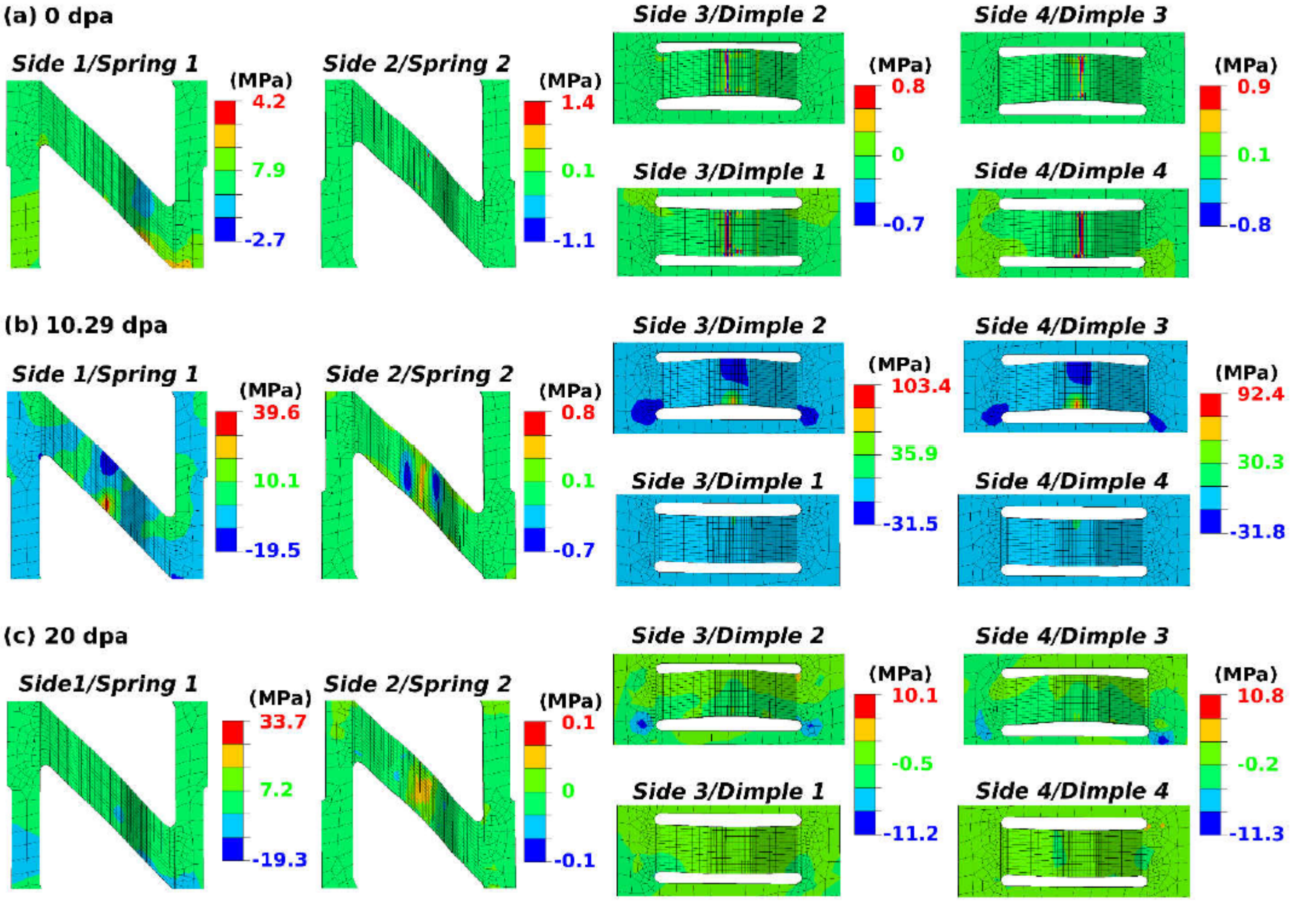

Figure 15. Distribution of pressure in the springs and dimples after a radiation exposure of a) 0 dpa, b) 10.3 dpa, and c) 20 dpa. Note that the scales are different in each of these contours to highlight the stress concentration.

As seen in Fig. 15a), there is a small pressure on the spring and dimple surfaces at 0 dpa dose. This is because the contact overclosures between the spacer grid mesh and the cladding tube mesh were resolved prior to irradiation. There is a thin line of contact on all the dimple surfaces, while no significant contact is observed on the spring surfaces to begin with. Figure 15b) shows a considerable increase in pressure on the spring and dimple surfaces at 10.29 dpa dose. The pressure goes up to 39.6 MPa on the bottom edge of spring 1 on side 1. It is still negligible on spring 2 on side 2. A higher pressure is observed on the bottom edges of dimple 2 on side 3 (≈ 80 MPa) and dimple 3 on side 4 (≈ 92.4 MPa). The top edges of dimple 1 on side 3 and dimple 4 on side 4 exhibit lower pressures of the order ≈ 50 MPa. Figure 15c) shows that the pressure is significantly relaxed in both the springs and dimples at 20 dpa dose, as compared to 10.29 dpa. The pressure magnitudes are negligible, indicating no contact and a complete gap opening on these surfaces.

These observed trends can be correlated to the synergistic effects of various deformation phenomena (irradiation growth, contact pressure relaxation, grid and rod constraints) occurring in the spacer grid and the cladding tube. These will be discussed in detail associated with the presentation of Figure 18 using the analysis for gap opening distance between the springs and dimples and the cladding tube.

Our simulations also predict the nodal normal contact forces on the springs and dimples during irradiation. The simulated nodal contact forces lie in the range 0.01-1.7 N. Spring 1 on side 1 exhibits a maximum contact force of 0.84 N at 15.89 dpa dose, while spring 2 on side 2 exhibits a maximum contact force of 0.02 N at 0 dpa. Dimple 1 on side 3 exhibits a maximum contact force of 0.47 N at 5.49 dpa dose, while dimple 2 on side 3 exhibits a maximum contact force of 1.12 N at 14.29 dpa dose. Dimple 3 on side 4 exhibits a maximum contact force of 1.72 N at 13.09 dpa dose, while dimple 4 on side 4 exhibits a maximum contact force of 0.29 N at 2.69 dpa dose. While we have only performed a static analysis here (with no coolant flow), these contact forces are consistent with other studies in the literature. Jiang et al. [25] performed finite element simulations of the dynamic impact of the fuel rod with the spacer grid for a plastically deforming Zircaloy-4 cladding and spacer grid. They found the rod-to-spring contact force to be in the range 0.08-0.16 N, and the rod-to-dimple contact force in the range 0.17-0.47 N [25]. Further, our model predictions are also consistent with the observation that the dimples generally experience higher contact force as compared to the springs [25].

- **Evolution of contact opening**

Figure 16 shows the side view of the bottom edge of dimple 1 on side 3 of the spacer grid after 0 dpa and 20 dpa dose. This side view only highlights the change in nodal positions in the ***x***- and ***y***-directions; there is an additional dimensional change due to irradiation growth along the ***z***-direction, which is not highlighted here. It is seen that the dimple edge depresses more near the left end as compared to the right end on being irradiated from 0 dpa to 20 dpa dose. This is possibly due to rotation of the cladding tube about the spring plane (to be discussed in detail associated with the presentation of Figure 18).

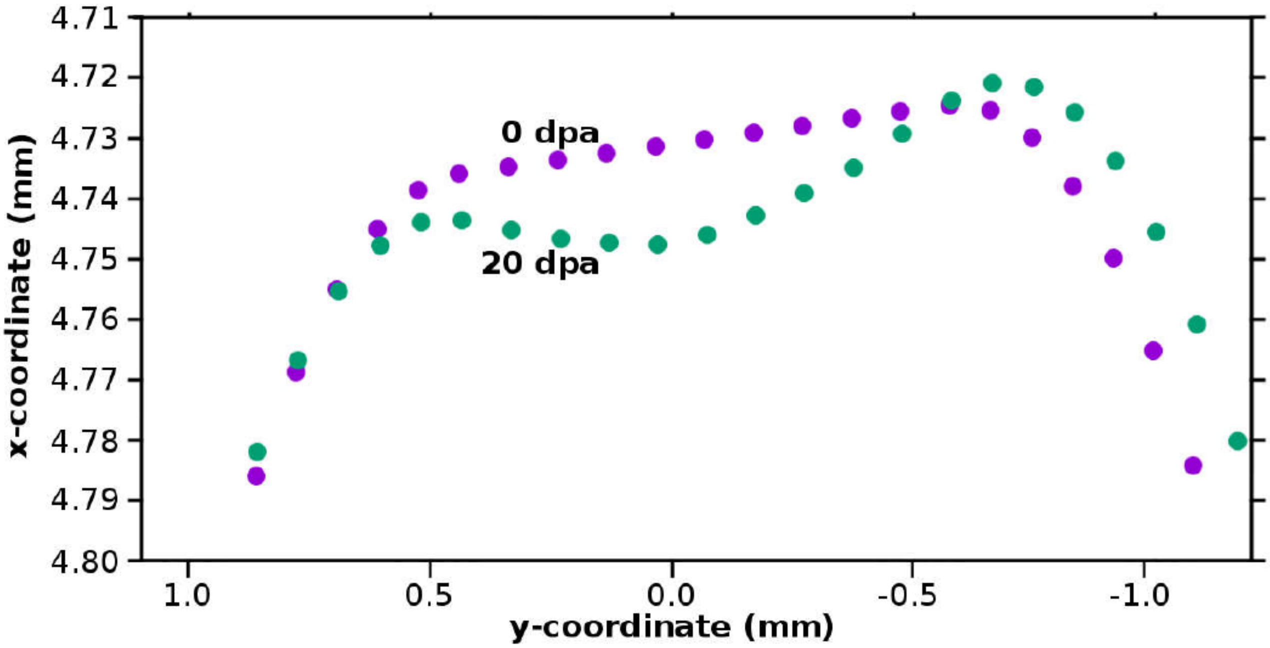

Figure 16. Side view of the location of the bottom edge of dimple 1 on side 3 of the spacer grid, after 0 dpa (purple) and 20 dpa (green), respectively.

However, as a result of the simultaneous deformation of the spacer grid and the cladding tube, it is difficult to infer the gap opening distance quantitatively over the entire contact surface. We use the contact opening distance variable, COPEN, in ABAQUS to get an average estimate of this. COPEN measures the distance between nearest nodes on the two contact surfaces (spring/dimple surface and cladding tube surface in the present case). Note that the surfaces in contact have to be specified *a priori*. At a given dose, we define gap as the arithmetic mean of COPEN over all nodes comprising the surface of a spring or a dimple, i.e.,

$$\mathrm{Gap}_{\mathrm{dpa}} = \frac{1}{N_{surface}} \sum_{i=1}^{N_{surface}} \mathrm{COPEN}^{i}_{\mathrm{dpa}} \tag{13}$$

where, COPEN^{i}_{dpa} is the contact opening distance of the i^{th} node at a given dpa dose, and $N_{surface}$ is the total number of nodes comprising the surface of the spring or dimple. Figure 17 shows the gap for the springs and dimples as a function of radiation dose. The initial non-zero values of gap measured at 0 dpa dose are due the fact that all nodes of the spring/dimple surface defined as the ‘contact surface’ in the simulation are not in contact, and should be regarded as a reference value. As seen in the pressure contours of the dimple surfaces in Fig. 15(a), for example, only a thin strip on the dimple surface is actually in contact with the cladding tube. All other nodes on these dimple surfaces have non-zero COPEN values even at 0 dpa dose.

It is seen that there is no gap opening with radiation for spring 2 on side 2, dimple 1 on side 3 and dimple 4 on side 4. On the other hand, the gap opening keeps increasing starting at ≈ 5 dpa dose, for spring 1 on side 1, dimple 2 on side 3 and dimple 3 on side 4. We define another measure to quantify the change in gap with radiation dose, $\Delta\left(\mathrm{Gap}\right)_{\mathrm{dpa}}$, as

$$\Delta\left(\mathrm{Gap}\right)_{\mathrm{dpa}} = \mathrm{Gap}_{\mathrm{dpa}} - \mathrm{Gap}_{0\,\mathrm{dpa}} \tag{14}$$

The value of $\Delta\left(\mathrm{Gap}\right)_{20\ \mathrm{dpa}}$ is 15.1 μm for spring 1, 29.3 μm for dimple 2, and 30.3 μm for dimple 3. This is the contribution of irradiation growth and creep to grid-to-rod gap opening under steady state conditions at 20 dpa dose. Note that we have not considered the effect of fretting wear due to frictional contact between the spacer grid and the cladding, which is also influenced by the turbulent coolant flow and associated vibrations. It is expected that fretting wear combined with irradiation-induced deformation would further enhance the grid-to-rod gap under dynamic coolant flow conditions. Nevertheless, our simulations predict that irradiation growth and creep have a non-negligible contribution to the gap opening. While there is not much quantitative data available in the literature regarding gap opening during in-reactor conditions, out-of-reactor experiments on fuel rod assemblies generally use a transverse displacement amplitude in the range 5-30 μm for grid-to-rod fretting wear tests [25,26]. In another analytical study [27], a grid-to-rod gap of 10 μm was predicted at end of life for Zircaloy-4 spacer grid and clad, with consideration for irradiation growth and creep using phenomenological constitutive models. In the aforementioned study, the predicted spring force relaxation compared favorably with relevant experiments [27]. Our finite element simulations predict gap opening in the same range as well.

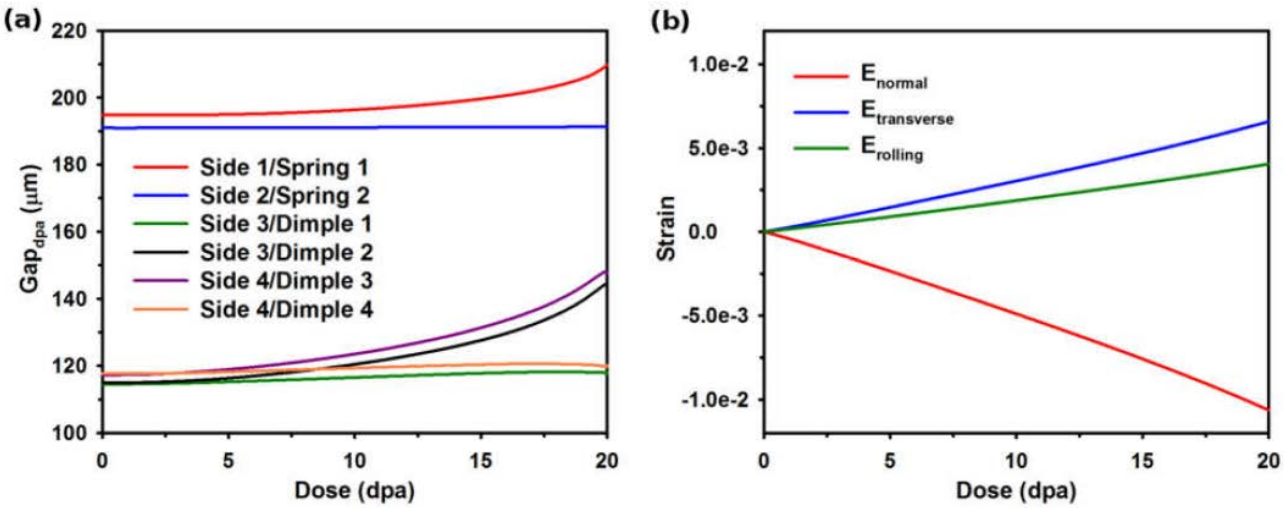

Figure 17. a) Gap as a function of radiation dose fro the springs and dimples, and b) predictions of growth strain for the texture shown in Fig. 13d.

Irradiation growth and creep are texture- and microstructure- dependent phenomena. Based on the texture given in Fig. 14b), the cladding tube elongates along the axial direction and shrinks along the radial and hoop direction due to irradiation growth. As shown in Fig. 17b), the spring texture in Fig. 14d) results in the springs and dimples expanding along the rolling and transverse direction and contracting along the normal direction. This is schematically described in Figure 18. Physically, the direction along the basal pole component of the texture exhibits contraction due to the aforementioned formation of vacancy loops along the ***c***-axis, while the direction(s) perpendicular to this exhibits elongation due to the formation of interstitial loops along the prismatic directions, $\boldsymbol{a}_1$, $\boldsymbol{a}_2$, and $\boldsymbol{a}_3$. Eventually, the gap between the spacer grid and the cladding tube opens with accumulated dose as the contact forces relax due to irradiation growth and creep.

However, as a result of the mechanical configuration of the ensemble, the gap does not open symmetrically because the springs and dimples are not disposed symmetrically with respect to the axis of the tube. As shown in Fig. 13, the spacer sides with springs (sides 1 and 2) are adjacent to each other, while the spacer sides with dimples (sides 3 and 4) are adjacent to each other. As shown previously, the contact forces are different in each of the springs and dimples. Visual inspection of the pressure contours in Fig. 15b) suggests that spring 1 on side 1 is still in contact with the cladding tube at 10.29 dpa dose, while spring 2 on side 2 is no longer in contact. Also, dimple 2 on side 3 and dimple 3 on side 4, which are near the top end of the tube in this simulation show higher contact pressures as compared to dimple 1 on side 3 and dimple 4 on side 4. This suggests that bending of the tube takes place about the bottom edge of dimple 2 and the top edge of dimple 1 on side 3, and the bottom edge of spring 1 on (diametrically opposite) side 1. This is schematically described in Fig. 18d). Moreover, since the spring is oriented at an angle with respect to the tube axis, the contact force exerted by the spring 1 on side 1 tends to rotate the cladding tube (Fig. 18e)). Rotation of the tube in the plane of the spring has also been studied using an analytical model by Billerey [27]. These trends suggest that a multiaxial bending and rotation of the cladding tube takes place during irradiation. The tube is inclined against sides 1, 4, and 3, which are adjacent to each other, and out of contact with side 2. With further irradiation up to 20 dpa (cf. Fig. 15c)), growth and creep relax the contact forces on the springs and dimples, such that they are completely out of contact with the cladding tube. These trends are also evident from the gap data presented in Fig. 17(a). It is seen that the gap opening does not change appreciably for spring 2 on side 2, while it increases with radiation dose for spring 1 on side 1. Also, the dimples near the bottom end of the tube (dimple 1 on side 3 and dimple 4 on side 4) do not show appreciable change in the gap, while the gap increases with radiation dose for those near the top end (dimple 2 on side 3 and dimple 3 on side 4).

Note that we have not modeled fuel pellets in the present work. It is expected that expansion of the fuel pellets will arrest the ‘inward’ creep of the cladding tube and consequently lead to a nearly uniform gap size after a certain radiation dose. Also, we have not considered the effect of external loads on the springs and dimples due to contact with the adjacent fuel rods in this analysis.

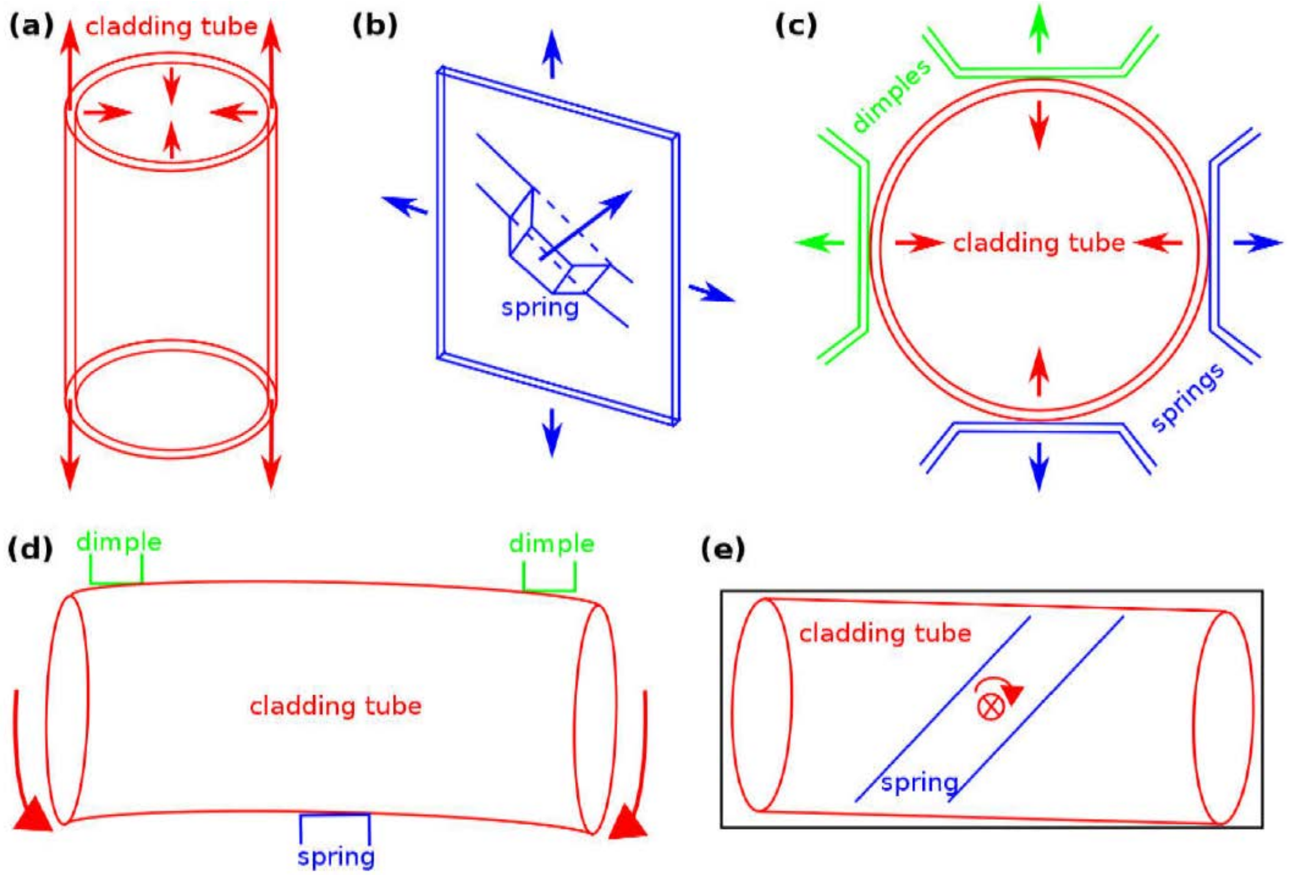

Figure 18. Schematic of texture-dependent deformation due to irradiation growth in a) cladding tube, b) spring on the spacer grid, c) top view of the cladding tube and springs/dimples of the spacer grid, d) side view demonstrating asymmetric bending of the cladding tube about one of the spring edges and the inner dimple edge, and e) side view showing rotation of the cladding tube about the plane of the spring. Arrows indicate the direction of deformation.

• **Effect of texture**

In order to assess whether texture can be used to either reduce or eliminate the gap opening, we have performed a parametric study of the effect of texture on the gap opening between the spacer grid and the cladding tube. Results from three simulations are compared where the texture for the spacer grid was rotated by 90° such that basal poles are either aligned with the normal (case T1), or the transverse (case T2), or the rolling direction (case T3) of the spring/dimple. Case 1 corresponds to the results presented previously associated with Figures 15 to 17. Gap evolution and VPSC-SA predictions of growth strain for case T1 were presented in Fig. 17. The same results for case T2 and case T3 are presented in Figs. 19 and 20, respectively.

Comparing the simulation results in Fig. 17a) with Fig. 19a), it can be seen that the gap evolution profiles for case T1 and case T2 are nearly identical for all the springs and dimples. The gap at 20 dpa for spring 1 is slightly higher for case T2, as compared to case T1. The VPSC-SA calculations in Fig. 17b) and Fig. 19b) show that the strain along the normal and transverse directions are interchanged between case T1 and case T2 as a result of the rotation of the texture with respect to the spring geometry. The normal and transverse directions correspond either to the ***x***- or ***y***-directions of the spacer grid plates (depending on their orientation), while the rolling direction corresponds to the ***z***-direction in the laboratory coordinates. Based on these FE simulations, it is evident that expansion or contraction of the springs and dimples along either the rolling or transverse directions does not affect the gap opening significantly.

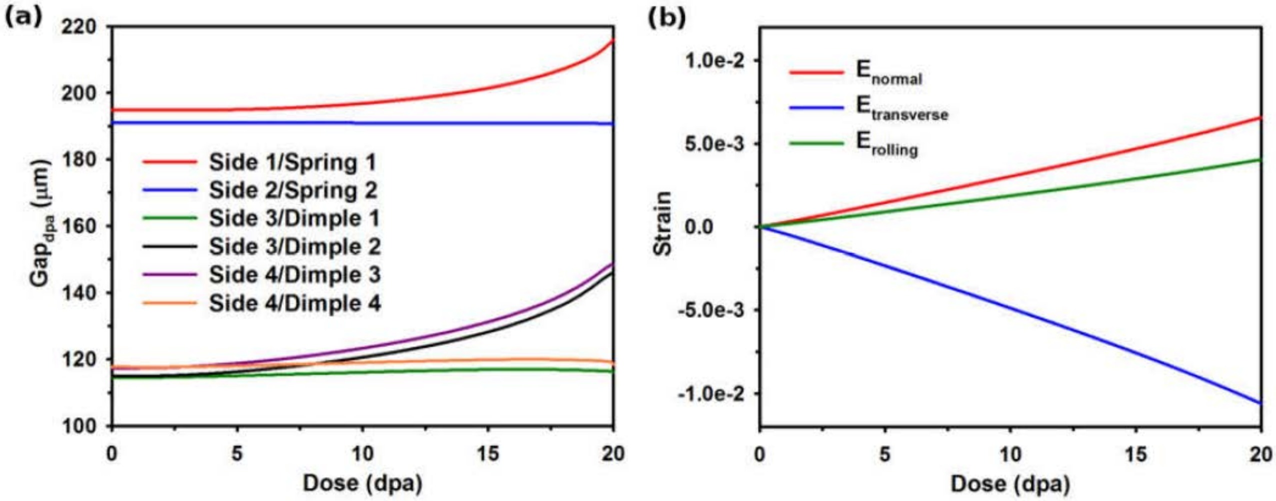

Figure 19. a) Gap as a function of radiation dose for the springs and dimples, and b) predictions of growth strain for case T2, in which the basal poles align along the transverse direction of the springs and dimples.

Figure 20a) shows that case T3 has a different gap evolution profile as compared to cases T1 and T2. VPSC-SA predictions in Fig. 10(b) show that the spring texture, with basal poles along the rolling direction, results in contraction along the rolling direction and expansion along the normal and transverse directions. For case T3, the gap still does not increase appreciably for spring 2 on side 2, dimple 1 on side 3 and dimple 4 on side 4. However, the gap is significantly larger for dimple 2 on side 3 and dimple 3 on side 4. It is also marginally larger for spring 1 on side 1 as compared to case T1. Irradiation growth is a volume-conserving process and contraction of the spacer grid along the rolling direction results in expansion along the normal and transverse directions with radiation dose. Consequently, net expansion occurs along the lateral direction for the springs and dimples and this relaxes the contact forces with the cladding tube, resulting in larger contact opening.

At ≈ 18 dpa dose, the gap starts to decrease again for dimple 2 on side 3 and dimple 3 on side 4. Comparison with the contact pressure profiles (not presented here) shows that dimple 2 and dimple 3 are completely out of contact with the cladding tube at this point. Note that dimple 1 on side 3, dimple 4 on side 4, and spring 2 on side 2 were already out of contact before reaching this dose, implying that side 2, side 3, and side 4 are now completely out of contact with the cladding tube. The cladding tube starts rotating about its plane of contact with spring 1 on side 1. Moreover, dimple 2 on side 3 and dimple 3 on side 4 are now completely relaxed (previously only the top edges of these dimples were in contact) and spatially relocated. As a result of the rotation of the cladding tube and the spatial relocation of nodes on dimple 2 and dimple 3, we see a small drop in the gap for these past 18 dpa dose.

This parametric study highlights the effect of texture (physically representative of the cold-work history of the material) on gap opening. If the spring sheets are processed such that the basal poles are predominantly aligned with the rolling direction, it leads to a larger gap, which is detrimental from the fretting wear perspective (more gap will facilitate more vibrations during coolant flow and consequently more fretting wear). Dominant basal poles along the transverse direction do not change the gap significantly as compared to the spring sheet with basal poles along the normal direction. Simulations with different textures may be used to guide the design of spacer grids that have lower gap opening.

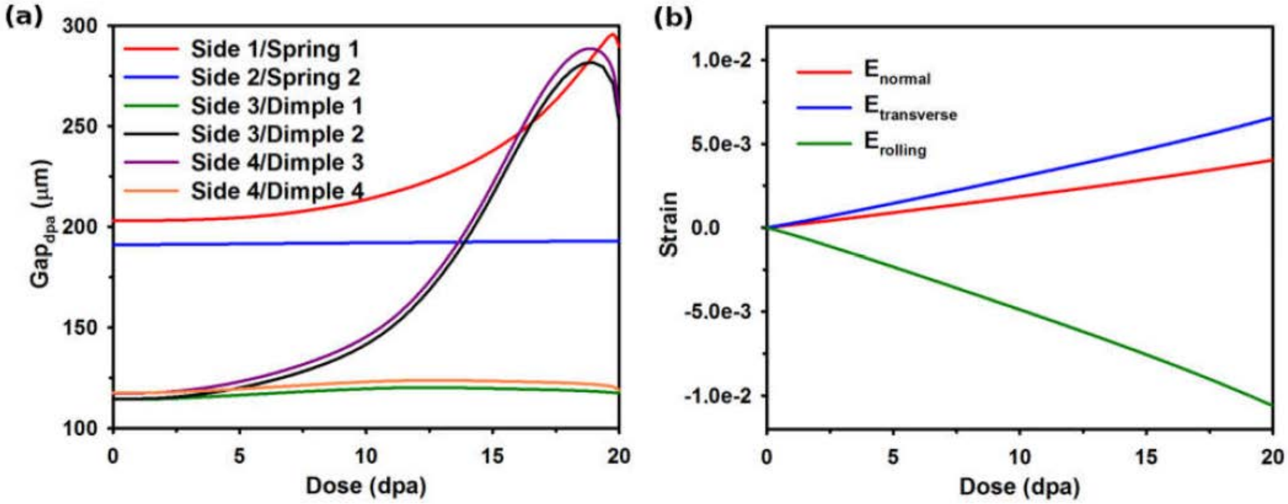

Figure 20. a) Gap as a function of radiation dose for the springs and dimples, and b) predictions of growth strain for case T3, in which the basal poles align along the rolling direction of the springs and dimples.

To summarize this study of gap development, we have identified the deformation mechanisms governing the gap opening, and these have been correlated to the texture-dependent material response. Contact pressures and contact forces on the springs and dimples have been calculated from our simulations and are found to compare favorably with available data in the literature. A parametric study has been performed to highlight the effect of texture on the gap evolution profiles of the springs and dimples. It is found that the hypothetical presence of basal poles along the rolling direction of the spring sheet leads to significantly larger gap opening and is detrimental from the perspective of subsequent wear. We find that the current texture of the grid is preferable, since it tends to minimize the gap opening. Larger gap opening is expected to lead to higher fretting wear and eventual fuel rod leakage. This is in agreement with in-reactor data, where numerous cases of fuel rod failures were found to occur at the periphery of the fuel rod assembly [28]. This also agrees with the proposed hypothesis that insufficient rod support is one of the factors contributing to higher grid-to-rod-fretting wear [28].

3.2 Effects of Gap Size and excitation frequency

The gap size plays an important role in determining the wear rate. Multiple possible scenarios may work together. A close fit between the rod and grid is often associated with a larger contact pressure and frictional force, and therefore tend to increase the wear rate if sliding happens. However, a sufficiently tight fit can restrict sliding, and therefore, reduce the wear rate. Conversely, a loose connection between the rod and grid may lead to dynamic impacts during oscillation; this would increase the wear rate. However, if the gap between the rod and the grid is too large, the oscillations may not be of sufficient amplitude to cause regular contact; this would reduce the wear rate. Of course, this would not be desirable, even if it was associated with a low wear rate because the spacer grid would not be providing adequate support for the fuel rod.

The wear rate is also sensitive to the excitation frequency, which depends on the mechanical design and flow velocity. Conceptually, the wear rate is expected to increase with the frequency and the amplitude of the rod vibration. A higher frequency would result in more fretting cycles in a given interval of time, while a larger vibration amplitude would generate a larger contact force. However, the situation is subtler than a simple dependence on these two parameters might suggest, because the frequency and the amplitude of the vibration of the rod are not independent. Even if one assumes a periodic excitation frequency from the fluid, the frequencies and amplitudes of the rod can become chaotic. As the excitation frequency increases through the natural frequency of the rod, the rod responds in subharmonic, period-doubling and chaotic modes of vibration. The responding frequency and amplitude of the rod may change dramatically as the vibration mode of the rod evolves from one regime to another. An additional issue is that the turbulent fluid flow induces chaotic vibrations, which further complicates the modeling. This has been discussed in the prior section. Here we focus on the issues that evolve from the assumption of a periodic driving force.

Most existing numerical models for GTRF have been based on 1-D simulations. While these models are capable of estimating how normal loads and displacements are affected by the geometry and vibration, they cannot provide local wear information; this requires details about the contacts and local stresses. Therefore, we have developed 3-D finite-element modeling approach to explore (a) the dynamic response of a fuel rod under the driving forces of various frequencies induced by the coolant, (b) the effects of the gap size and initial interference on the wear rate of the rod, and (c) the effect of the excitation frequency on the wear rate. There are two key contributions of this study. The first is a calculation of the critical gap size that generates the greatest wear. The second is a calculation that shows how this critical gap depends on the excitation frequency and dynamic response of the rod.

Figure 15 shows a 3-D model of a simplified rod and grid system that we used to explore the interaction of the gap size, geometry, and vibration frequency on wear rate.

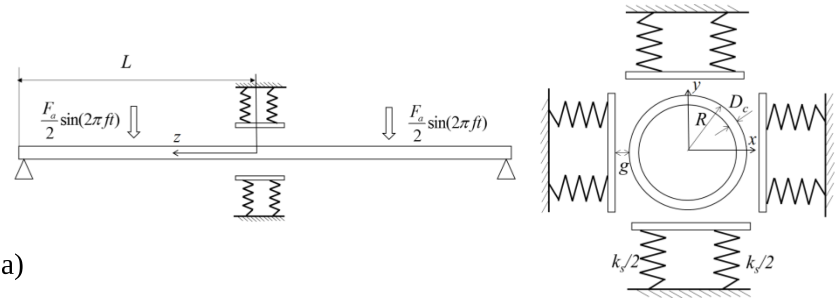

(a)

(b)

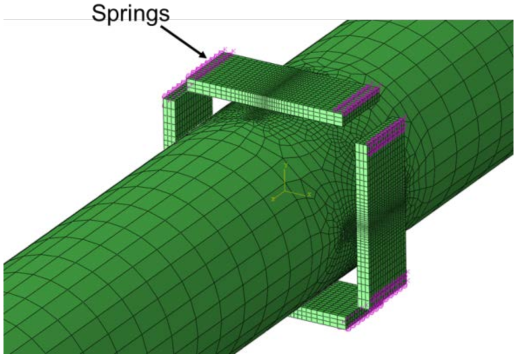

Figure 21. A simplified 3-D model used for the GTRF simulation. (a) A schematic illustration of the side view and the cross-section view showing the load and constraint. The fuel rod has an outer radius of R with a cladding thickness of Dc. Four support plates are connected to springs with a stiffness of ks. The gap between the fuel rod and the plate is g. The vibration of the rod is assumed to occur along a plane inclined at 45° to the x- and y-axes. (b) 3-D finite-element model of the rod and supports. Contact elements and refined meshes are used in the contact regions. Each plate is connected to ground springs with a total stiffness of ks.

We performed a series of calculations covering a large spectrum of gap sizes and excitation frequencies. Figure 22 shows the dependence of the wear rate on the gap size and excitation frequency. In the subharmonic regime, there is a critical gap size associated with the maximum wear rate for each excitation frequency. When the gap size exceeds the critical value, the vibration becomes chaotic and the wear rate drops dramatically. The critical gap that is associated with the peak wear rate is dependent on the excitation frequency.

As shown in Fig. 22, the maximum wear rate in the landscape of gap size and excitation frequency correlates with the natural resonance of the system, which is defined as the frequency of the first mode of free vibration of the system consisting of the rod and support plates.

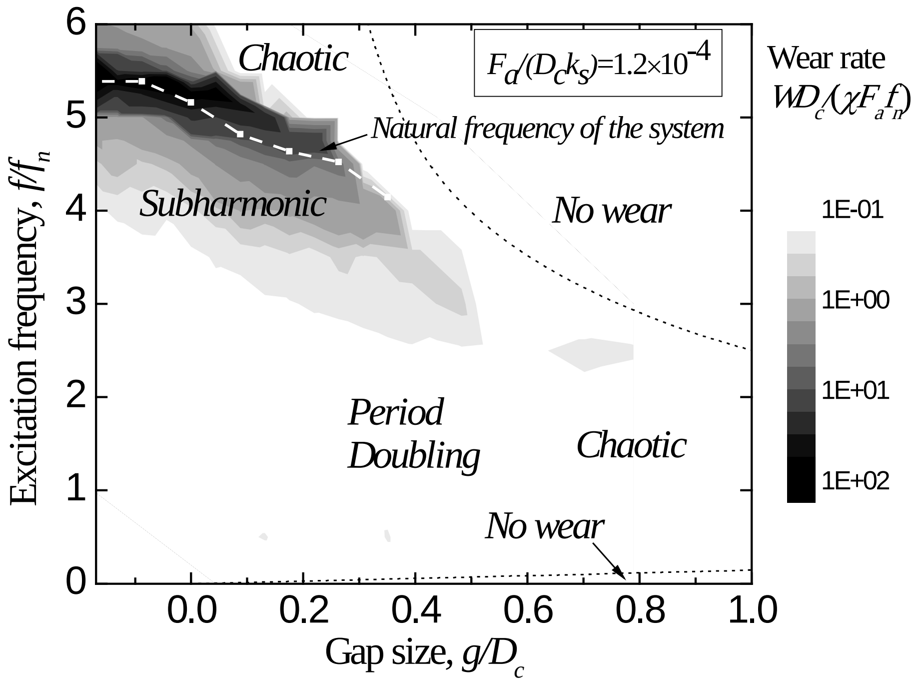

Figure 22. A wear-rate map for a large spectrum of gap sizes and excitation frequencies. The critical gap size, which is associated with the maximum wear rate, lies within the subharmonic regime. In the no wear region the amplitude of the rod vibration is smaller than the gap size so that no impact between the rod and plate can happen. The curve of the natural frequency of the system appears to overlap with the peaks in the contour.

3.3 Coupling Wear with Creep and Oxidation in 2-Dimensional Finite Elements

2D Finite Element Model

The geometry and boundary conditions of the GTRF model are provided in Figure 23. We did some preliminary simulations using this model before; now we reran those and did new simulations with the adaptive-meshing method for both wear and oxide growth.

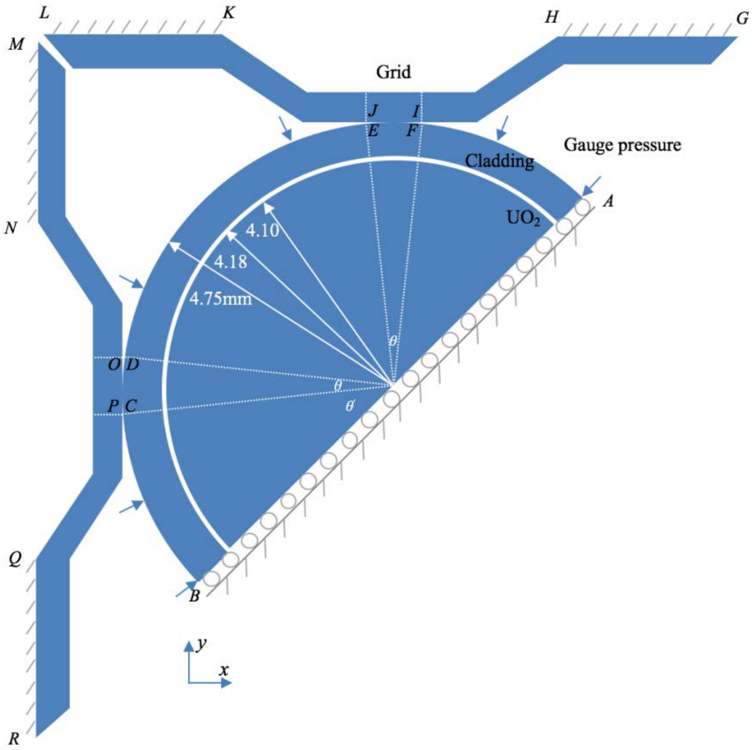

Figure 23. The grid, cladding and UO2 assembly. Wear is simulated on the surfaces of CD/OP, and EF/IJ. Symmetric boundary conditions are enforced along AB. An oscillating pressure is applied on the BC surface. To apply the initial interference, the boundaries MN and QR are displaced along the x-direction, while the boundaries LK and GH are displaced along the y-direction. The four boundaries are then fully constrained before starting the simulation. The angle θ is 6°, while the angle θ' is 42°. The thermal problem was solved by considering the realistic conditions, including the heating rate in the fuel, thermal properties of the fuel and the cladding, an initial space between the inner surface of the cladding and the outer surface of the fuel (the fuel rod fill gas was assumed to be helium). Thermal expansion, elastic deformation and mechanism-based creep of zircaloy, and elastic deformation, thermal expansion, creep and swelling of UO2 were included. The creep-down of the cladding due to the external pressure causes dimensional changes to the cladding.

Based on the Hillner model [29], the oxidation rate for the pre- and post-transition is expressed with the equations below:

$$\text{Pre-transition (cubic oxidation rate)}: W^3 = 6.36\times10^{11}\exp(-13636/T)\times t \qquad (15)$$

$$\text{Post-transition (linear oxidation rate)}: W = 1.12\times10^{8}\exp(-12529/T)\times t \qquad (16)$$

Here W is the weight gain (mg/dm^2), T is the absolute temperature (K), and t is the total exposure time (days). The transition time and transition weight can be obtained by equating the W in Eq. (15) and Eq. (16), giving

$$t_t = 6.73\times10^{-7}\exp(11975/\text{T}) \qquad (17)$$

$$W_t = 7.53\times10^1 \exp(-553.6/T) \tag{18}$$

where t_t is the time to transition from cubic to linear kinetics (days), and W_t is the weight gain at transition $(\mathrm{mg/dm^2})$. In the simulation, we assumed that the temperature of the surface of both the grid and the rod are 600K during operation. Equations (17) and (18) are valid in the temperature range of 430K-670K, so it was appropriate to apply these equations for the given temperature of 600K. The weight gain of the oxide can be converted to the increase of the oxide thickness, with $14.9\ \mathrm{mg/dm^2}$ weight gain corresponds to 1 μm increase in the thickness [4]. Moreover, the wear coefficient of the oxide layer was assumed to be 50 to 200 times lower than that of the zircaloy based on recent experimental data [15].

Coupled Wear and Creep

Many physical phenomena take place simultaneously in the GTRF problem. How to couple them poses a computational challenge. As an example, here we show how creep and wear can be coupled. Both creep and fretting wear between the fuel rod and spacer grid can cause the contact force to relax. Conversely, the contact stress affects both creep and wear. While creep and wear are inherently coupled in the GTRF problem, the characteristic time scales of the two mechanisms are quite different. The time-scale of the dominated frequency of the turbulence in the coolant can be described by a frequency of 10Hz or higher. Therefore, a single cycle of wear can occur within a second. In contrast, significant creep can take place at the scale of days or months. Using the small time increment suitable for each wear cycle would be too computational expensive and impractical. On the other hand, using the relative large time step suitable for creep may miss significant changes in contact stress induced by wear.

To resolve this large difference in time scales, we have developed an effective cycle approach. Within a single period of the excitation force, neither creep nor wear will cause significant changes to the geometry or to the contact pressure. Therefore, up to some limit, several successive vibration cycles can be combined into a single effective cycle with a larger period without loss of accuracy (Fig. 24). We need to calculate a practical limit or how many cycles can be combined into a new effective cycle, without significant loss of accuracy. In calculating an optimal effective period, it is noted that both wear and creep cause stress redistribution, and both affect each other because of this stress change. The effective cycle technique takes care of this interaction in a systematic and efficient way. For instance, creep causes stress relaxation within each effective cycle, and this change in stress inherently interacts with the wear calculation, since both wear and creep are calculated simultaneously at each time step within the effective cycle.

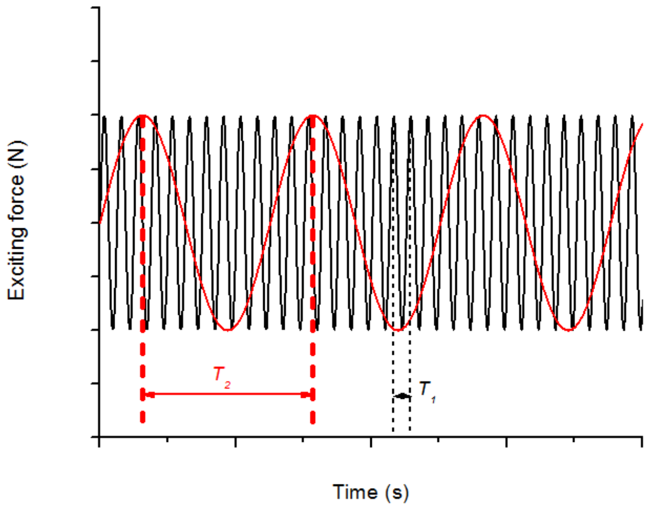

Figure 24. The effective cycle approach to couple creep and wear. Several successive vibration cycles (T1) are combined into a single effective cycle with a larger period (T2). The interaction between creep and wear is inherently taken care of within the effective cycle. The period of the effective cycle is adjusted dynamically for both computational efficiency and accuracy.

The period of the effective cycle is adjusted dynamically based on the current rate of stress relaxation from both creep and wear in accordance with any required accuracy. This automatic adjustment of the effective cycle is achieved by continuously monitoring the change of contact pressure. Our studies have shown that drops in contact pressure across an interface as large as 20% between two successive effective cycles can still give accurate results in terms of the wear shape and contact pressure distribution.

We have coupled the effective cycle approach and the fictitious-eigenstrain approach for wear, and the mechanism-based creep model to evaluate gap formation in GTRF. These tools are used to model gap formation in a simplified 2-D GTRF model (Fig. 23). However, it is important to note that turbulent flow effects have not been incorporated. Such coupling is incredibly complex, but some progress has been achieved within CASL, as discussed in Section 3.5.

Wear profile evolution (arrow shows increasing time)

Contact force relaxation

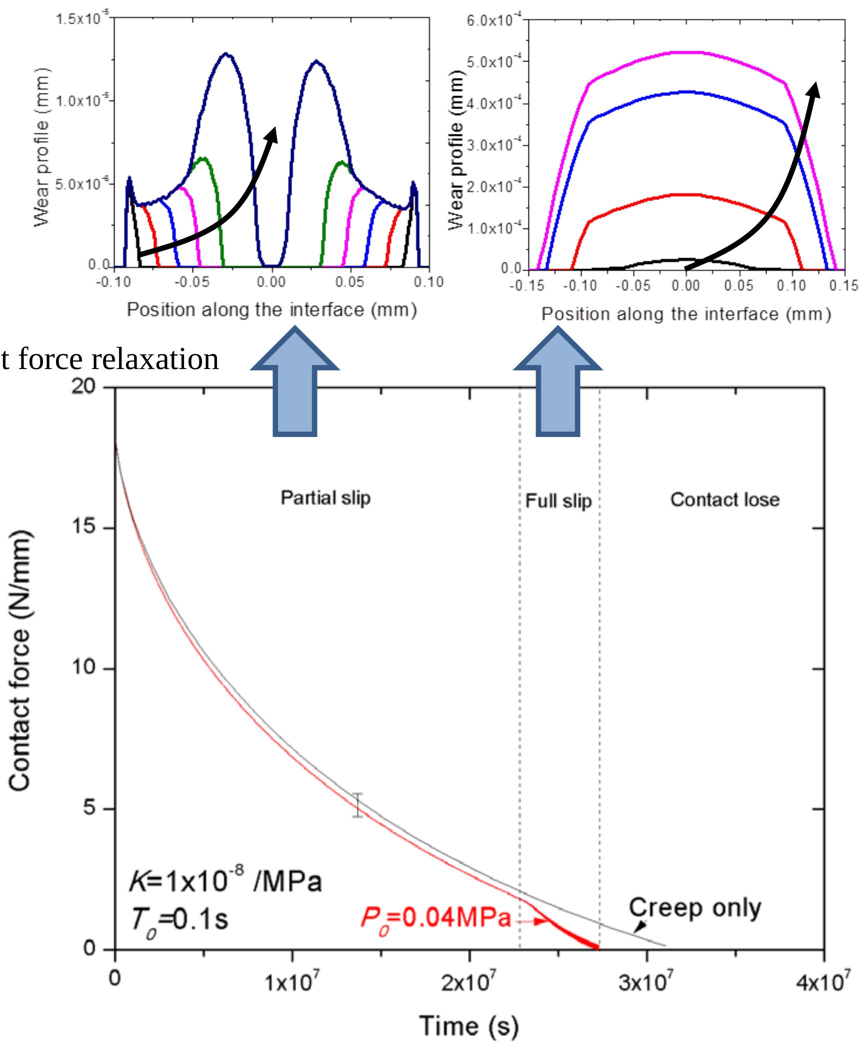

Figure 25. The contact force, which is the total force due to contact pressure, relaxes over time. Two stages exist: partial slip and full slip. When partial slip occurs, creep is found to dominate the stress relaxation. When full slip occurs, wear is found to become the dominant stress relaxation mechanism. The wear scar shows different geometry in the partial slip and full slip stages.

Figure 25 shows the contact force relaxation process during service due to creep and wear. For comparison, we have also shown the stress relaxation if only creep is active, and no wear. The comparison shows that when partial slip occurs, creep dominants the stress relaxation. When full slip occurs, wear becomes the dominant stress relaxation mechanism. The result not only gives a prediction of the service time before the loss of contact event happens, but also shows that the process is composed of two stages: partial slip where wear happens at the edge of the contact surface, and full slip where wear happens at the entire surface. Though the amount of wear is smaller in the partial slip stage, this stage occupies most of the time and therefore partial slip is an important factor in GTRF.

The insets in Fig. 25 also show the wear profile evolution at different stages. The wear scar shows different geometry in the partial slip and full slip stages.

At present the excitation force caused by the turbulent flow is modeled as a sinusoidal wave. It is possible for future studies to replace the sinusoidal wave by the turbulent excitation force spectrum obtained from the computational fluid dynamics. This model will be used to simulate the contact force relaxation at different conditions of excitation force, wear coefficient and initial interference to provide guidance to the assembly design. With its prediction capability, appropriate actions can be taken when the grid and fuel rod lose contact.

Coupled Wear, Oxidation and Creep

The simulation results for the relaxation of the contact force are shown in Fig. 26. These results show no difference from our previous results for which oxide growth was described by adaptive meshing and the wearing surface was modeled by the eigenstrain method. In the figure, μ is the friction coefficient, K_o and K_s are wear coefficients of the oxide layer and of the substrate, E is the Young's modulus, F_0 is the amplitude of excitation force, R is the outer radius of the cladding, N is the normal contact force, and T_0 is the period of sinusoidal excitation force. Our simulations show that from the beginning till loss of contact only the cubic oxidation rate was active because the oxide layer did not reach the thickness for post-transition linear oxide growth.

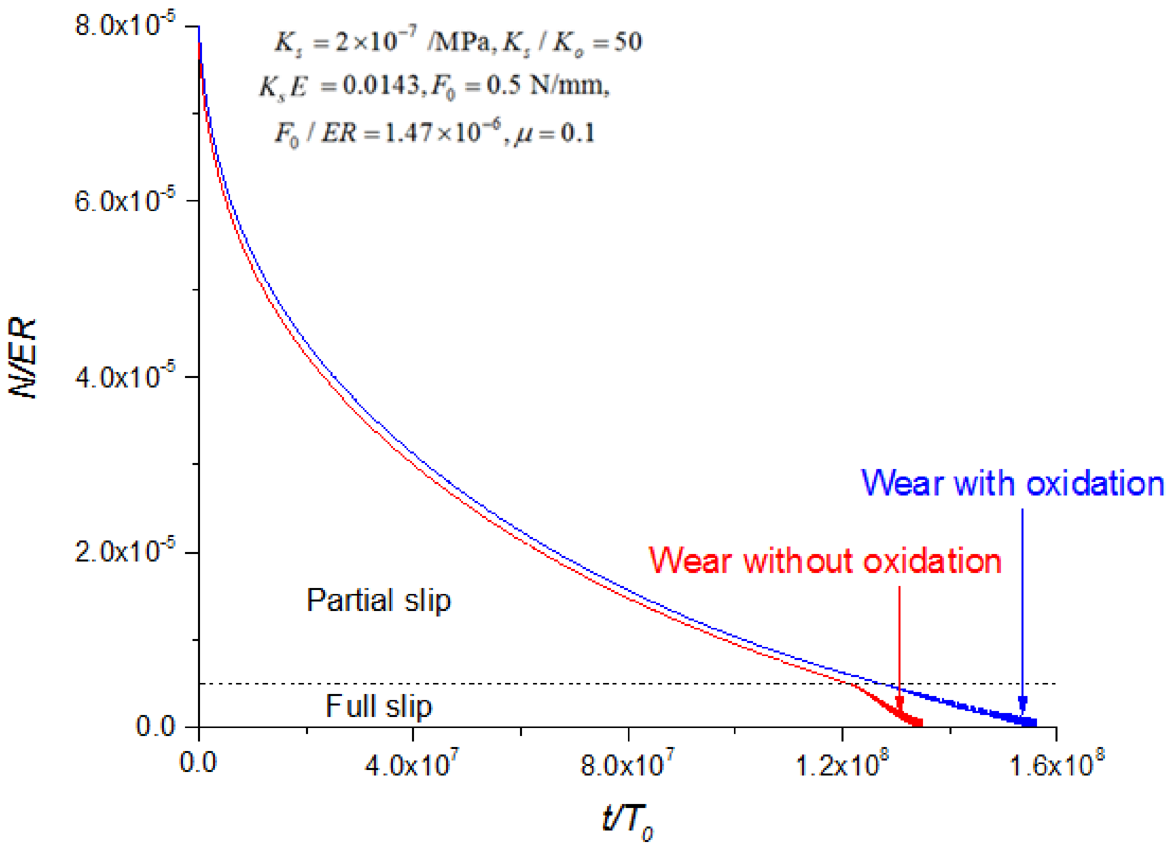

Figure 26. Plots of contact force relaxation over time with and without oxidation.

We can observe that the time for the contact force to be fully relaxed, corresponding to gap formation and loss of contact between the rod and the grid, is about 180 days. In comparison to the case without oxidation (red curve), the gap formation is delayed by about a month. We found that wear cannot penetrate the oxide layer before contact is lost, with the growth rates with the parameters we used. In addition to exhibiting a low wear coefficient, the growing oxide layer increases the contact pressure between the rod and the grid, which delays the gap formation. Furthermore, the onset of full slip is delayed by the presence of an oxide layer, owing to the increased contact pressure. Since the wear coefficient of the oxide layer is quite low, stress relaxation is still dominated by creep even after full slip occurs.

The evolution of wear profiles with concurrent oxide growth is given in Fig. 27 at different times. Initially, wear scars form near the edges of the contact, which are characterized by the peaks at the left and right end of Fig. 27a). Then, as the contact force is relaxed, mostly by creep, slip extends to the center of contact, and so does the wear scar. As creep further relaxes the contact force, full slip occurs. In this full-slip regime, wear scars extending from the edges merge at their center, and wear occurs over the entire contact surface. As shown in Fig. 27b), full-slip is characterized by deep wear scars in the center region. We can also observe that the wear scar becomes wider with time, but eventually reaches a limit.

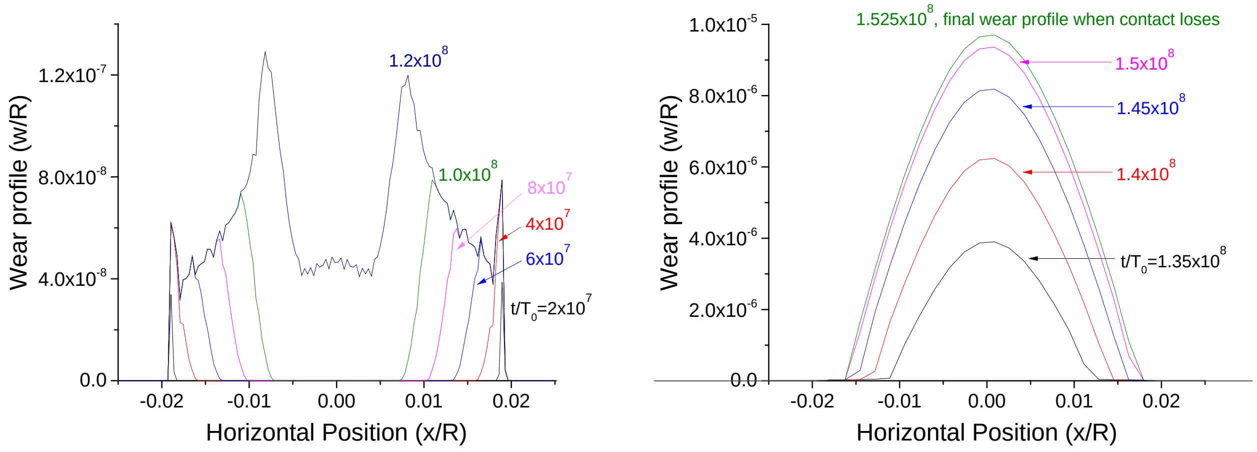

(a) (b)

Figure 27. Wear profiles at different times: (a) partial slip regime, and (b) full slip regime.

A comparison of wear profiles in the full-slip regime, with and without oxidation, is given in Figure 28. The wear depth when there is oxidation is much smaller than when there is no oxidation, owing to the low wear coefficient of the oxide. In addition, the wear profile is narrower for the case with oxidation, which can also be explained by the low wear coefficient of oxide. For the case of a Hertzian contact, as applicable for GTRF, the peak pressure at the center of contact decreases toward a uniform distribution as wear proceeds, by increasing the size of the contact area [30]. In contrast, the oxide layer delays the wearing process so that the peak pressure cannot be distributed over a wider contact surface. Because of these, stress relaxation is dominated by the creep mechanism and the effect of wear on stress relaxation becomes almost negligible.

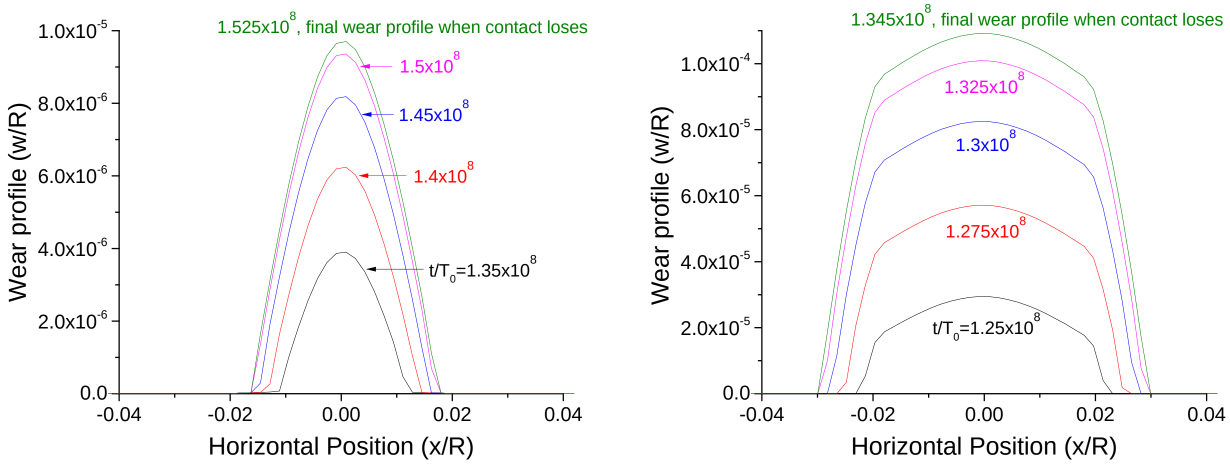

(a) (b)

Figure 28. Wear profiles under full slip regime. (a) with oxidation, (b) without oxidation.

3.4 Structural Mechanics and fluid-induced turbulent excitations in multi-rod geometry

Multi-rod grid coupling

Traditional modeling approaches [31] accounting for turbulence-driven rod vibration rely on statistical characterizations of fluctuating fluid pressure distributions on the rod surfaces based on random vibration theory [32]. Loading is applied to structural rod models based on classical Euler-Bernoulli elastic beam theory, coupled at multiple positions along its length to grounded springs representing discrete points of mechanical interaction (contact, friction, sliding) with grid springs and dimples. Resulting histories of point contact force, and relative sliding at each spring and dimple site are generated and analyzed for accumulated sliding wear work, and wide-ranging parametric studies of specific variables can be assessed and used to drive more-detailed continuum modeling of the wear processes, as in the following section. We have adopted certain features of the structural modeling approaches used in the VITRAN rod vibration modeling software [33], including approximation of turbulent loading using a Gaussian Band-Limited White Noise approximation of the power spectral density (PSD) of discrete transverse point loads applied downstream of each mid-span grid. For linearized random vibrations, the magnitude of the PSD scales that of observables such as mid-span velocity and acceleration, providing a means of calibration. The FFT algorithm is used to span the frequency window, generating a set of temporal sine waves of random phase shift, constraining half of them to produce a real signal of the desired PSD form. Rod vibration is simulated over a time interval sufficiently large compared to the maximum loading period by explicit integration of projected modal dynamics, accounting for solution-dependent grid/rod contact interactions. Multiple realizations of random phase shifts provide a converged estimate of the mean and the standard deviation of frictional work (rate) at each potential contact.

The support stiffnesses of the springs and dimples of a given grid cell facet's interaction with its adjacent fuel rod(s) are intrinsically coupled, owing to the local bending flexibility of the orthogonal grid strips, as their respective 'egg crate' structures have been connected to form an integral multi-cell grid that, in totality, is substantially grounded with respect to global transverse motion.

Figure 29 shows a representative grid strip and illustrates the support coupling of two adjacent rods with the two dimples and one spring comprising a single panel of the grid cell. Let the non-negative contact forces at the spring and dimples of a panel segment be denoted by $\boldsymbol{F}$ and the corresponding normal deflections be denoted by $\boldsymbol{\delta}$; an elastic stiffness matrix connects these quantities according to

$$\begin{bmatrix} k_{ss} & k_{sd_1} & k_{sd_2} \\ k_{d_1s} & k_{d_1d_1} & k_{d_1d_2} \\ k_{d_2s} & k_{d_2d_1} & k_{d_2d_2} \end{bmatrix} \begin{Bmatrix} \delta_s \\ \delta_{d_1} \\ \delta_{d_2} \end{Bmatrix} = \begin{Bmatrix} F_s \\ F_{d_1} \\ F_{d_2} \end{Bmatrix}.$$

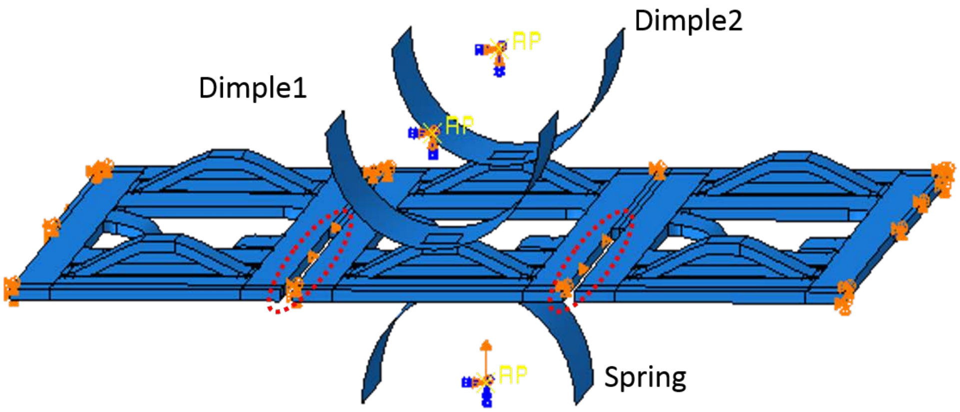

Figure 29. Schematic illustration of rod contact at the 2 dimples and one opposing spring comprising a single panel of a spacer grid cell. Contact force at any one site on the panel elastically deflects all grid contact points on the panel segment.

We have incorporated this two-sided elastically-coupled contact stiffness within the structural mechanics models of multi-rod vibration, and have discovered that spatial patterning of peak sliding wear work can take place within model multi-rod/multi-grid assemblies. Figure 30 illustrates the spatial patterning of computed wear work rate in a model 5 by 5 assembly. Each tube was supported by 7 spacer grids and subjected to identical initial support conditions of zero gap and zero normal force, along with span-by-span turbulent loading of constant PSD for a fixed interval. Repeated simulations resulted in converged values for mean and standard deviation of wear work rate at each contact point. For each rod, the peak mean wear rate computed at any contact point along the rod is normalized, in percent, by the corresponding value for a single rod identically loaded and supported by the four coupled grid panels comprising the grid cell at each spacer grid. First, none of the rods in the model assembly exhibited wear rates exceeding that of the single-rod model, suggesting that the latter provides conservative estimates of wear work. Secondly, the peak wear work in the upper right corner rod, which was supported externally by (stiffer) dimples and internally by (compliant) springs, matched that of the single rod, while the rod in the lower-left corner, supported externally by springs and internally by dimples, exhibited roughly half the wear work of the single-rod model, with intermediate levels of peak wear work along external assembly edges having a dimple support. The reduced wear-work values for interior rod locations is caused by changes in average contact force because adjacent-cell rod contact elastically deflects the contact point on shared grid cell panels. It is interesting to note that the spatial patterns revealed in this simple model bear similarities to patterns of leaking rods within a representative assembly, concentrated along external corners and edges [34].

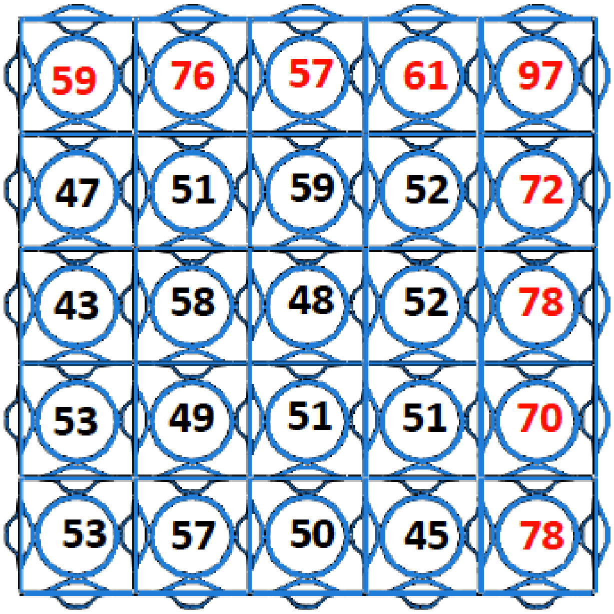

59	76	57	61	97
47	51	59	52	72
43	58	48	52	78
53	49	51	51	70
53	57	50	45	78

Figure 30 Summary of normalized mean peak wear-work rate, in per cent, calculated for a model five by five rod array under conditions of zero mean normal contact force and zero mean gap at each grid/rod interaction point. Normalization is with respect to the corresponding mean peak wear work in a single-rod model, supported at each grid by a single-cell of four compliance-coupled panels.

Multi-Rod Fluid-Structure Coupling

Typically, flow-induced vibrations in GTRF are modeled by studying the force spectrum on an isolated rod, generally assumed rigid, interacting with a transverse flow at high-Reynolds number. An important consideration when applying these observations to the system level is whether flow through a rod assembly causes geometric coupling with the fluid phase, resulting in certain rods receiving different forcing signatures than others.

This question can be addressed through a full fluid-structure interaction study of a multi-rod system. The simulation method used is the Reference Map Technique [35,36], an Eulerian numerical framework that permits the simulation of a dynamic fluid phase interacting with a possibly nonlinear continuum solid phase, computed on a single, fixed numerical grid.

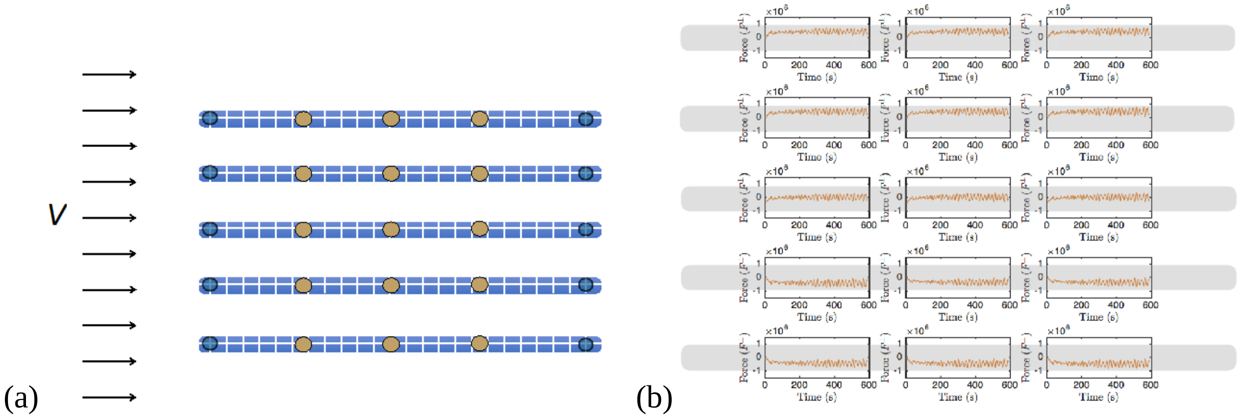

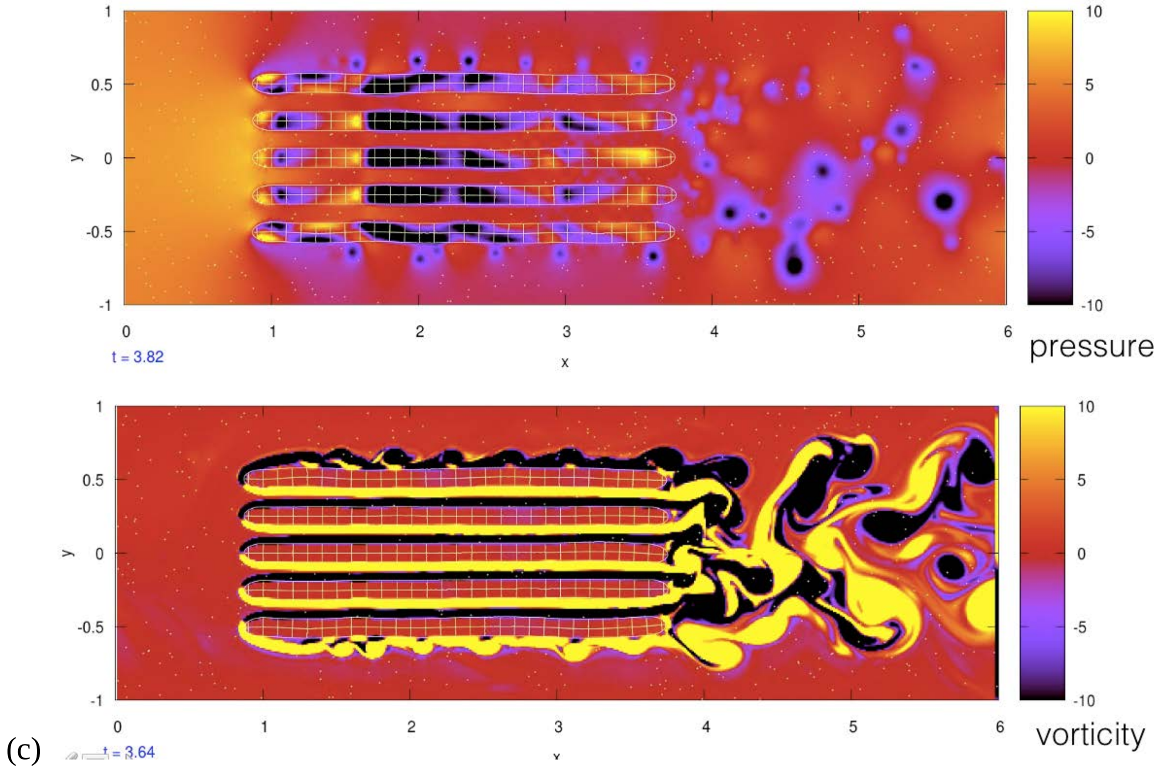

Figure 31. (a) Model environment of five rods anchored at their ends and subject to an incoming uniform fluid flow. Weak supports provided at three interior locations. (b) Transverse forces at the interior supports on each rod from the onset of fluid flow to steady behavior. (c) Snapshot of relative pressure and vorticity (in SI) during simulation.

We simulate five parallel rods idealized in 2D as solid elastic bodies anchored firmly at their ends and weakly (10x smaller) at three internal points per rod, to model three grid supports per rod. The anchoring is modeled with spring forces spread over the area of the interaction, shown in the figure. An incoming transverse fluid flow is introduced (c.f. Figure 31(a)). To bring out possible coupling of rod motions through the fluid, the rods are given an artificially high elastic compliance. The non-laminar fluid motion successfully induces flow-induced vibrations of the rods (Reynolds number = 12,000). The simulations allow a determination of the velocity and pressure fields in the fluid and within the rods during the process (Figure31(c)).

The simulation shows a fluctuating force of the grids on the rods, consistent with turbulent flow induced vibration of the rods, but, interestingly, there is also a non-negligible mean normal force, which vanishes on the central rod and pushes outward on the extreme rods (Figure 31(b)). A mean force as indicated from the simulation is rarely if ever considered in typical FIV studies used as inputs to GTRF in which only a single rod is considered. As previously noted, rods at the extremal locations of an assembly tend to be more susceptible to wear [34]. Likewise, fluid coupling of the rod system appears to provide another possible reason for this effect, on top of the effect of grid-wise coupling described previously.

We can study the effect of FIV loading at the dimple-spring supports by extracting the force distributions at each such constraint over time. These forces represent the contact forces expected to emerge between the rods and the spring-dimples of the grid and are the key forcing responsible for GTRF. In the direction of flow (i.e. the direction tangent to the rod orientation), we see, expectedly, that the force on the rods at the constraints grows quickly once fluid flow is turned. Such results are shown in Figure 32. The mean tangential force per constraint point per rod is roughly equal (i.e. little variation depending on rod positioning) and the tangential force fluctuations are on the order of 5-10% of the mean. It is clear the dominant behavior of this force component is to prevent the mean fluid flow from translating the rods downstream.

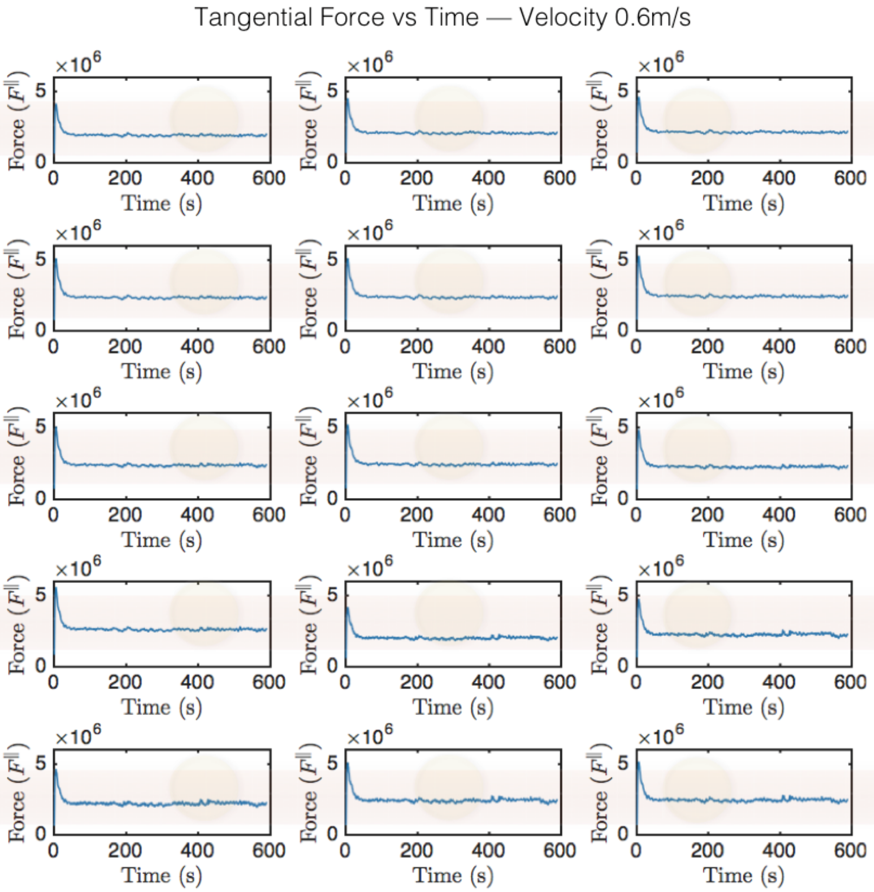

Figure 32. Tangential force time-series at all grid constraints on all rods in the model assembly. In-flow fluid velocity V=0.6 m/s.

This result lies in contrast to the behavior of the lateral force component. This component represents the force normal to the rod alignment, which arises from the grid contacts to resist rod vibration, see Figure 33. For all rods, the force is dominated by fluctuations, expectedly. Also, as expected due to symmetry, the force distribution over time on the central rod has zero up-down mean bias. Interestingly however, it is apparent that the extremal rods --- the ones at the top and bottom of the assembly --- do develop a mean lateral force at the grid constraints. In fact, moving away from the central rod, the mean normal grid-force on the rods is directed *outward* (away from the assembly core) and grows progressively to a maximum at the external rods.

While it is certainly true that wear/leaking is exacerbated by larger force fluctuations, there is a possible role to be played by an emergent mean force as well. Recalling that leaking rods are known to occur with higher frequency on the edges of the assembly[ii] we propose that the mean force we observe, which is largest on the far rods of the assembly, can prematurely open gaps on the interior side of those rod contacts. Once a gap opens, wear-rate increases and failure occurs more quickly. Hence, the mean hydrodynamic force that develops on exterior rods could explain why rods on the corners and edges of an assembly are the most susceptible to failure. This explanation for the positioning of leaking rods is an alternative to the fully-structural explanation based on modal analysis of grid vibrations proposed by the multi-rod structural analysis.

[ii] Z.E. Karoutas, M.A. Krammen, Y. Aleshin, R.L. Kesterson, and S.F. Proceedings of the Water Reactor Fuel Performance Meeting—WRFPM/Top Fuel (2009)

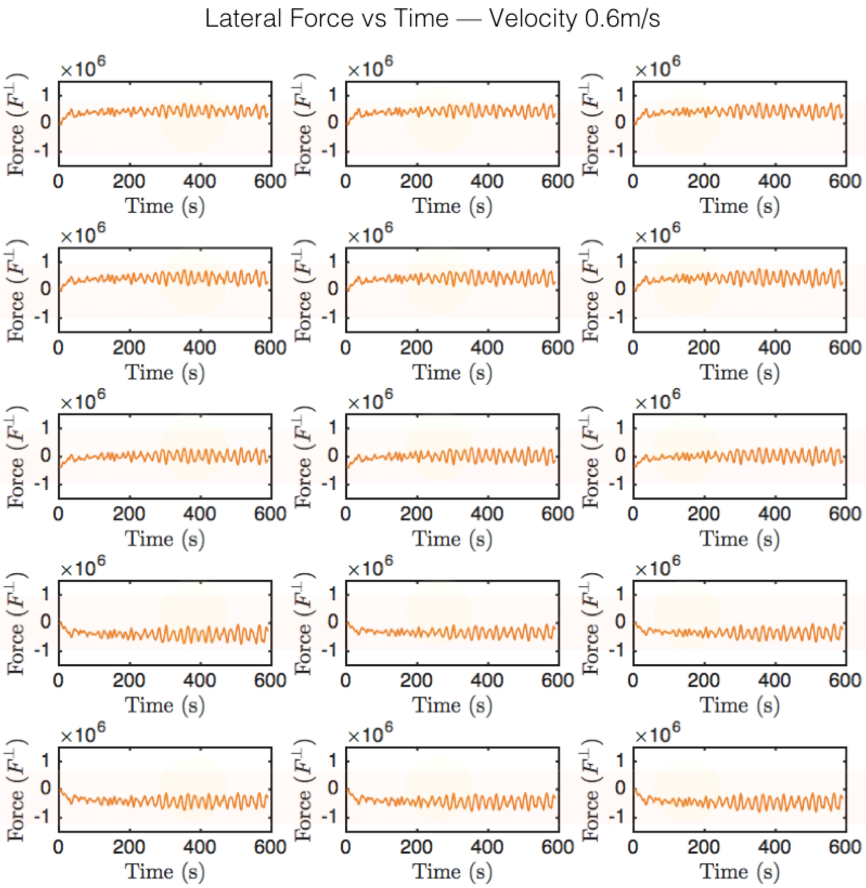

Figure 33. Lateral force time-series at all grid constraints on all rods in the model assembly. In-flow fluid velocity V=0.6 m/s.

4.FRETTING TEST RIG (AUTOCLAVE FRETTING & IMPACT RIG, AFIR)

As stated earlier, the simulation of GTRF conditions in the laboratory is difficult, especially when it comes to replicating the identical contact motions, stress history, creep, temperatures, coolant pressures, flow, fluid chemistry, and neutron irradiation. However, forward progress on simulation and prediction of GTRF behavior demands validated models. A laboratory-scale testing machine to more closely simulate GTRF conditions and serve to train and compare results of the EWM was designed and then installed at ORNL in May 2017.

4.1 Design and Testing of Autoclave Fretting & Impact Rig (AFIR)

It is once again important to point out that, *one cannot understand friction or wear test results unless one first understands the characteristics of the apparatus used to produce them.* Obviously, the more sophisticated the equipment used in research such as this work, the more complicated it is to characterize and determine quantitatively factors such as experimental variability from test-to-test (repeatability) resulting from the ability of the tester to produce accurate results and for the users to compensate for any inherent bias or lack of precision arising from the apparatus design and operation.

Broadly, wear or friction testing can be considered as being either basic/fundamental studies or applied (a.k.a. simulative) studies. The former purpose attempts to make 'generic' measurements using simple contact geometries or to investigate the mechanisms of various forms or wear or types of materials under controlled laboratory conditions. The latter ideally attempts to simulate as closely as possible, the conditions of the intended application so that the data produced can be translated into practice and lead to effective selections of materials, surface treatments, or lubricants. While both purposes for testing can present challenges in the design and operation of the apparatus, arguably the simulative purpose is more challenging because it has to rigorously mimic the mechanical, thermal, and chemical environment of the intended application. One approach is to substitute the materials or interest in the actual machinery to evaluate or rank performance, but that course may be impractical, so some combination of modeling and laboratory testing is employed.

The subject of laboratory-scale tribotester design to produce useful simulations of engineering components has been the subject of books, reviews, and handbooks and will not be further elaborated here (e.g., [37,38]). Suffice it to say that the friction and wear of any material couple responds to the imposed conditions from its tribosystem whether that tribosystem happens to be an engineering device or a laboratory testing machine. Matching the characteristics of the former tribosystem with those of the latter is an essential key to effective simulation. If all aspects of the engineering system of interest (e.g., contact force, type of motion, speed, temperature, or chemical environment) cannot be simulated, one means to determine if the laboratory-scale system is useful for wear testing is to examined the wear surfaces produced and see whether they exhibit the observed features of damage that occurs in the application. In the current case, latter criterion was one of those employed to test the usefulness of the AFIR device. Attempts were made to simulate the type of motion, normal force, amplitude of oscillation, ambient water pressure, and temperature of the grid/rod tribosystem in a PWR.

Figure 34. A newly-designed unique autoclave fretting-impact rig at ORNL. (top-left) The AFIR apparatus showing the control unit, power supply, and plumbing; (top-right) The furnace and test chamber behind the panels; (bottom-left) The autoclave vessel with and liquid and gas handling system; (bottom-right) The specimen assembly inside the autoclave chamber. Each run can test two separate grid/cladding pairs of different material and/or contact geometry combinations. A cladding tube frets against two grid dimples, thus producing a total of four wearing grid/clad contacts in each experiment.

There were three aspects of using the autoclave fretting-impact rig (AFIR) shown in Figure 34. The first aspect was to compare ORNL test data to data on GTRF obtained at other laboratories or industrial research facilities, such as the VIPER tests conducted at WEC or GTRF references from the literature. The second aspect was to compare data with predictions of the derivation of the wear factor as described in Section 2, and the third was use the experimental data produced in the AFIR experiments to test the EWM. These issues are discussed in subsequent sections of this chapter.

4.2 Design, Fabrication and Installation of AFIR

The ORNL-BTC-WEC team determined that a GTRF simulative bench tester should be capable of testing actual pairs of cladding and grid specimens at water temperature from room temperature to 220 ^{o}C under pressure up to 24 bars. This would allow to correlate the bench test results with the VIPER dynamometer data at WEC. Note that VIPER operates at 204 ^{o}C (400 ^{o}F) under about 20 bars pressure. ORNL’s finite element analysis of the cladding-grid contact in FY 2016 estimated that the contact force between the cladding and grid is in the range of 0.08-0.47 N [39]. Therefore the load capability was determined to be 0.1-1.0 N. Based on vibration simulation of WEC [40,41], the desired oscillation frequency is 20-60 Hz, and the stroke is less than 200 μm. The machine also is expected to allow tests of fretting, impact, and fretting plus impact. However, no commercial tribometer meets all the requirements!

The major technical challenge was to precisely drive the very small relative motion under a very small load inside an autoclave. Conventional designs use driving shafts (between the samples and actuator) through the autoclave wall, which is very difficult (1) to get an accurate fretting amplitude in the design range (<200 μm) or good alignment without affecting the small load (0.1-1.0 N) due to the high friction between the shaft and seals of the hole on the vessel wall, and (2) to maintain the high pressure with shaft oscillating in and out (20-60 Hz), a potential safety issue.

The AFIR unit was designed and built by Phoenix Tribology, UK based on an innovative concept: using a miniature autoclave, housing rod-grid contact pairs, vibrated by a voice coil actuator underneath. The entire assembly is vibrated about a vertical axis to induce relative motion between two sets of moving and fixed specimens. Fixed specimens are mounted on lever arms and are loaded against moving specimens by a stainless steel spring, tensioned between the levers. Moving specimens are carried on flexural springs, allowing one degree of freedom along the vertical axis. The autoclave diameter is only 100 mm and there is no driving shaft through the vessel wall!

Although the design concept was clever and straightforward, the process of fabrication, installation, and development was quite a journey:

•5/2015,	Phoenix Tribology proposed the design concept
•6/2015,	Phoenix Tribology was selected as the vendor

- 11/2015, Phoenix Tribology made a non-vessel prototype for proof-of-concept
- 12/2015, PO was issued to Phoenix Tribology
- 4/2016, Full assembly design was done and orders were sent out for components and parts
- 8/2016, Most parts and components were ready, except the LBBC autoclave (being manufactured) and Kaman displacement sensor (received but faulty)
- 9/2016, Autoclave vessel was manufactured and received CE certification
- 11/2016, Autoclave was assembled but failed in final test at LBBC (heater sent back for repair)
- 12/2016, Displacement sensor was fixed and delivered to Phoenix Tribology
- 1/2017, Autoclave was reassembled with the fixed heater and received final CE certification
- 1/31/2017, Autoclave was delivered to Phoenix Tribology
- 3/2017, AFIR was assembled and trial tests were conducted
- 4/24/2017, AFIR was delivered to ORNL
- 5/9/2017, AFIR was installed by Phoenix Tribology in the lab L103 in building 4515 at ORNL
- 5/17/2017, First test at room temperature succeeded
- 5/23/2017, First test at elevated water temperature (150 ^{o}C, 8.8 bars) succeeded
- 6/2/2017, First test at target water temperature (204 ^{o}C, 21 bars) succeeded
- 7/21/2017, First test with H_2-rich water at 204 ^{o}C succeeded
- 8/1/2017, First test with close-loop control of the fretting amplitude succeeded
- 8/10/2017, First test with simulated PWR coolant at 204 ^{o}C succeeded

While installation was in early May 2017, additional development of the apparatus continued for several months afterwards in order to better understand its operating characteristics and to control the applied variables. Owing to the innovative design of the AFIR to avoid mechanical actuators having to feed into the high pressure autoclave chamber, the vibration of the chamber itself induces, by virtue of the elasticity and stiffness of the supports, a certain variability in the amplitude of fretting, which turned out to be one of the challenges in test control during the initial matrix of experiments. A close-loop control mechanism was eventually implemented to control the fretting stroke around the set point with variations less than 20 μm. Another challenge was the temperature gradient inside the vessel causing difficulties in pressure control.

The current parameters of AFIR are shown in Table 5 in comparison with those of VIPER. Both systems operate at a nominal water temperature of 204 ^{o}C with a vessel pressure around 20 bars. The contact force between the cladding and grid dimple is 0.4-0.6 N in AFIR, matching the peak cladding-dimple force 0.5 N in VIPER. The fretting frequency in AFIR currently is set at 25 Hz, right in the middle of the oscillation frequency range 20-30 Hz in VIPER. Limited by the motion control precision, the oscillation stroke in AFIR (50-100 μm) is slightly longer than that in VIPER (up to 20 μm), but both fall in the fretting wear regime (stroke < 300 μm). While the AFIR test duration currently is set at 20 hours to quickly generate data, a longer test, e.g., 100 hours, is readily feasible if matching the work at the contact interface in VIPER or other GTRF systems is of interest. Distilled water is used in VIPER without added chemistry. AFIR can deal with both distilled water and simulated light water reactor coolants.

Table 5. Comparison of the bench-scale AFIR at ORNL and the dynamometer VIPER at WEC.

	Water Temp (°C)	Vessel Pressure (bar)	Cladding-Dimple Load (N)	Oscillation Frequency (Hz)	Oscillation Stroke (um)	Test Duration (hr)	Work Rate (mW)	Work (mWh)
VIPER	204	18-24	0-0.5	20-30	0-20	500	0-0.6	0-300
AFIR	204	18-24	0.4-0.6	25	50-100	20	1.0-3.0	20-60

4.3 AFIR Tests in de-ionized water

The first series of tests used an actual Zr alloy cladding fretting against two actual grids of a Zr alloy and a stainless steel in in D.I. water. Three sets of tests were carried out as follows.

- Self-mated Zr alloy cladding and grid at water temperature of 22, 150 and 204 °C, under the vessel pressure of 1, 9, and 20 bars respectively, to reveal the impact of water temperature on the cladding wear and oxidation;
- Different clad-grid material combinations to investigate the effects of pre-oxidation and grid material on the cladding wear rate. Material combinations include:
  - Self-mated as-received Zr alloy cladding and grid (Zr-Zr)
  - Pre-oxidized Zr alloy cladding against as-received Zr alloy grid (ZrO-Zr)
  - As-received Zr alloy cladding against pre-oxidized Zr alloy grid (Zr-ZrO)
  - Pre-oxidized Zr alloy cladding against pre-oxidized Zr alloy grid (ZrO-ZrO)
  - As-received Zr alloy cladding against stainless steel alloy grid (Zr-SS)
  - Pre-oxidized Zr alloy cladding against stainless steel alloy grid (Zr-SS)

Effects of water temperature

Water temperature truly matters for the wear rate! From 22 to 150 and then 204 °C, the cladding volumetric wear coefficient was increased by 2.5X and 4.8X, respectively, as shown in Fig. 35. Figure 36 shows the Cladding and grid specimens after the 20-hr tests at 22 (left), 150 (center), and 204 °C (right), respectively. The surface color change suggests more oxidation at a higher water temperature. Figure 37 compares the morphology of the cladding wear scars using SEM imaging and composition by EDS analysis. The EDS spectra show a higher O:Zr ratio at a higher water temperature, indicating increased oxidation.

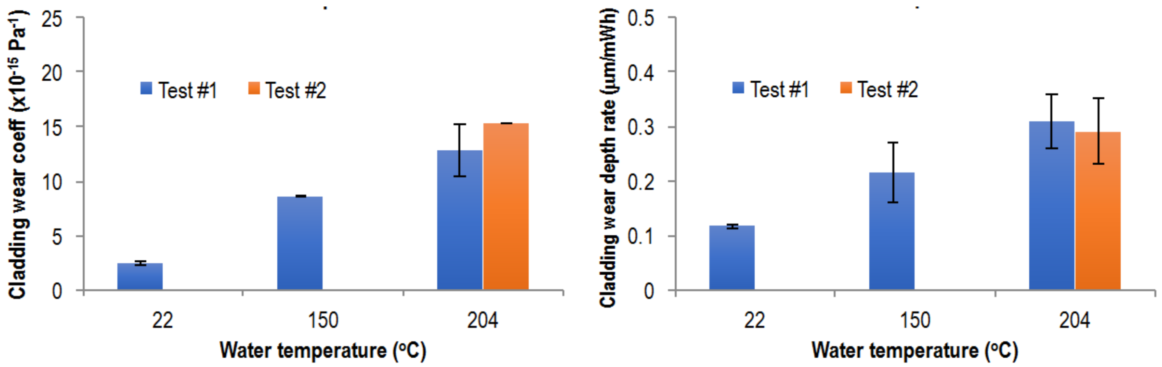

(a) Volumetric wear coefficient (b) Linear wear depth rate

Figure 35. Comparison of wear results at different water temperatures, clearly showing an increased wear rate a higher water temperature.

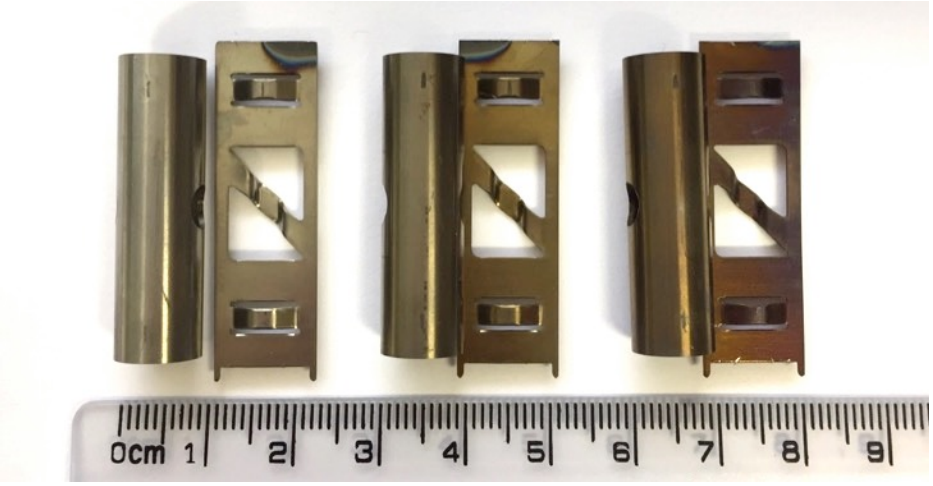

Figure 36. Cladding and grid specimens after the 20-hr tests at 22 (left), 150 (center), and 204 oC (right), respectively. The surface color change suggests more oxidation at a higher water temperature.

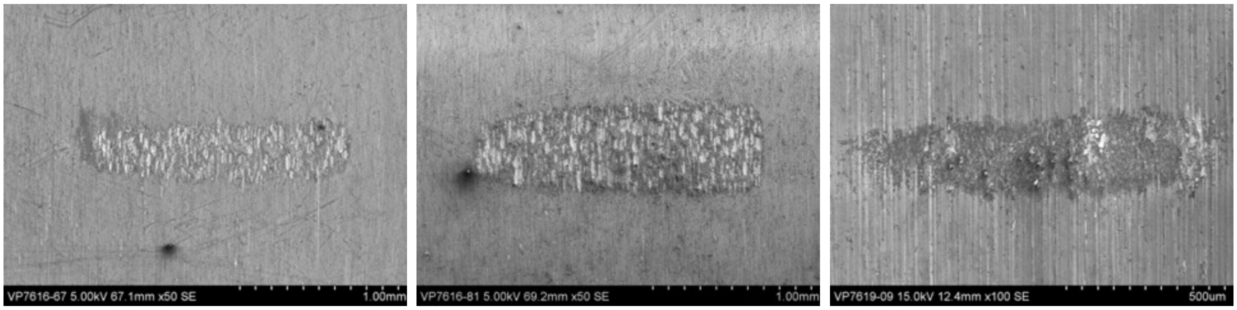

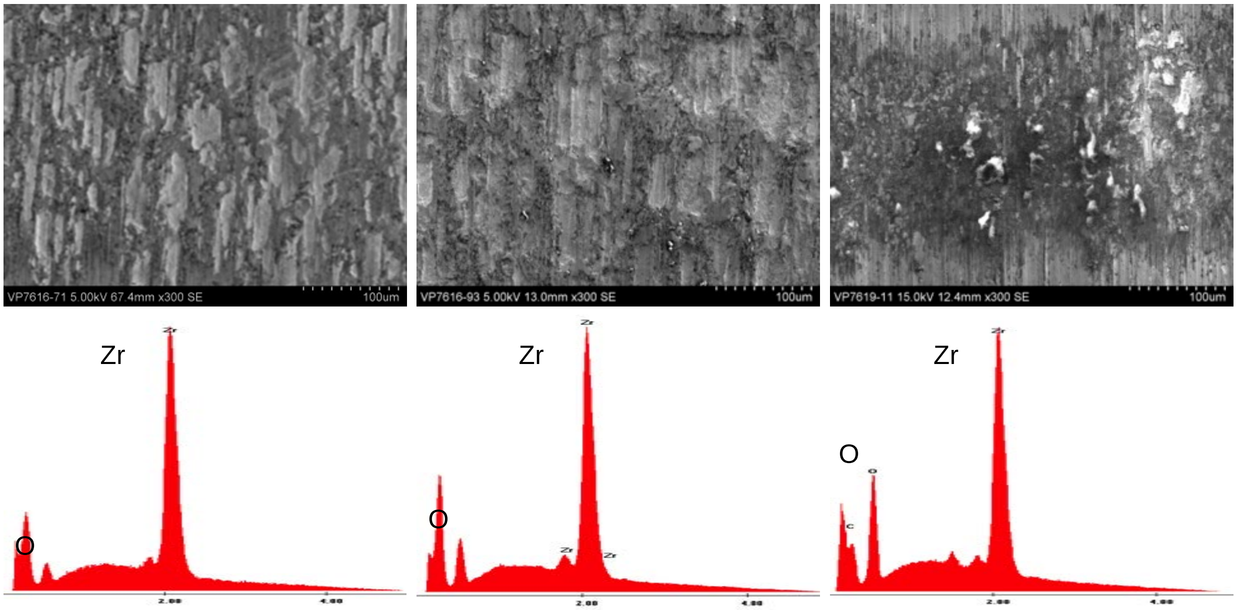

(a) 22 ^{o}C (b) 150 ^{o}C (c) 204 ^{o}C

Figure 37. Comparison of morphology of the cladding wear scars generated at different water temperatures using SEM imaging and composition by EDS analysis. The EDS spectra show a higher O:Zr ratio at a higher water temperature, indicating increased oxidation.

Effects of pre-oxidation

Pre-oxidation of the Zr cladding is known to improve the wear resistance in room temperature bench fretting tests [15] and VIPER dynamometer tests [42]. This set of tests investigated the effects of pre-oxidation on the Zr alloy cladding, grid, or both. The wear results are shown in Fig. 38. Pre-oxidation of the Zr cladding alone reduced the wear coefficient by 77%. While pre-oxidation of the Zr grid alone had no clear-trend impact on wear coefficient, it smoothened the cladding wear scars with less adhesion. Pre-oxidation of both the cladding and grid decisively reduced the wear coefficient by 90%.

The wear scar morphology is compared using 3D white light interferometry scan, as shown in Fig. 39. Pre-oxidation generally not only reduced the wear scar size but also made the worn area smoother, changing the wear mode from a combined adhesion and abrasion to abrasion-domination.

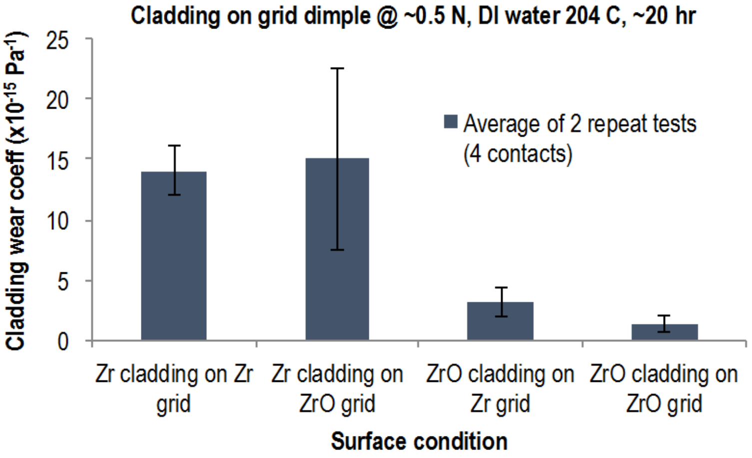

(a) Volumetric wear coefficient

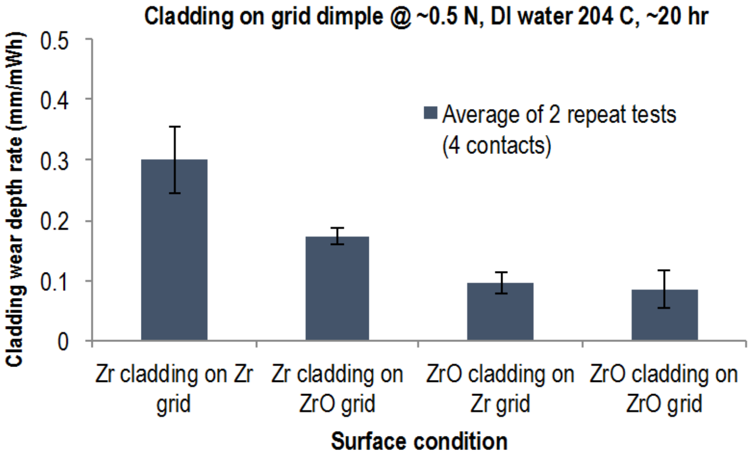

(b) Linear wear depth rate

Figure 38. Comparison of wear results for Zr alloy cladding and grid in different combinations of as-received and pre-oxidized conditions, clearly showing wear reduction with cladding pre-oxidation.

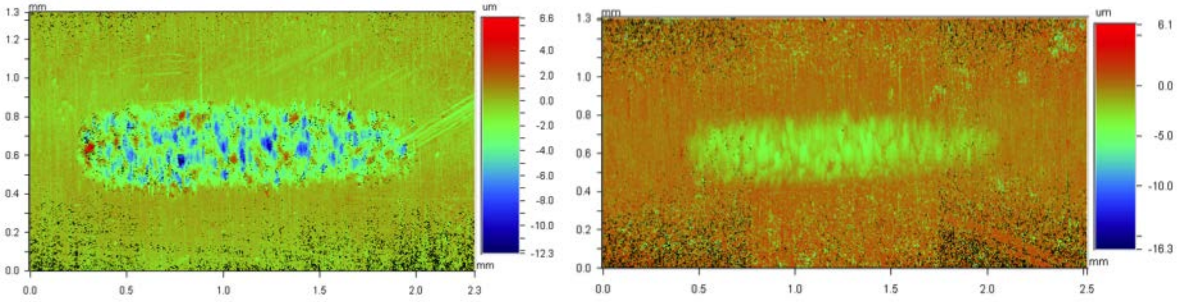

(a) Zr-Zr (b) ZrO-Zr

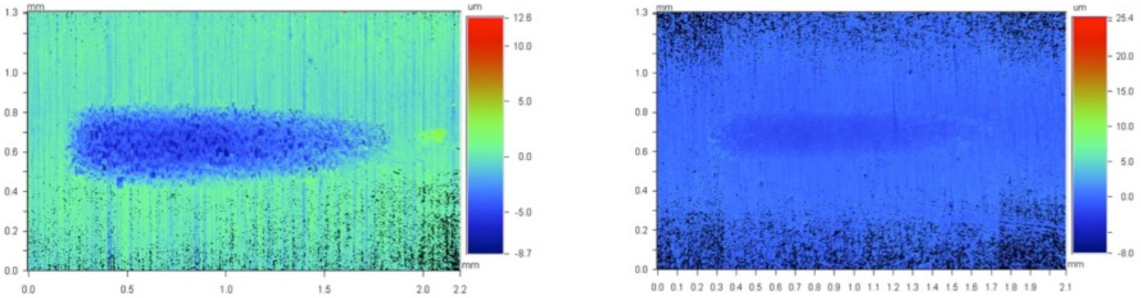

(a) Zr-ZrO (b) ZrO-ZrO

Figure 39. Comparison of wear scar morphology for Zr alloy cladding against Zr alloy grid with pre-oxidation of the cladding, grid, or both.

Stainless steel grid

AFIR tests showed that the grid material had great influence on the cladding wear. Under the same test condition, using a stainless steel grid reduced the Zr cladding wear coefficient by 87%, as shown in Fig. 40. The pre-oxidized Zr cladding had no measurable wear or noticeable surface damage when rubbing against the stainless steel grid (see the wear summary chart in Fig. 42). A wear reduction was expected for using the stainless steel grid because rubbing of dissimilar materials usually has less adhesive wear, but we did not imagine such a dramatic impact.

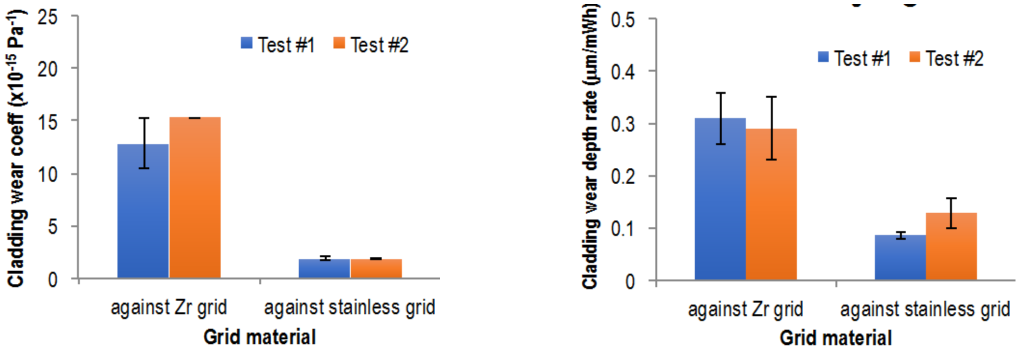

(a) Volumetric wear coefficient (b) Linear wear depth rate

Figure 40. Comparison of wear results of Zr alloy cladding rubbing Zr alloy and stainless steel grids, clearly showing significant wear reduction by using the stainless steel grid.

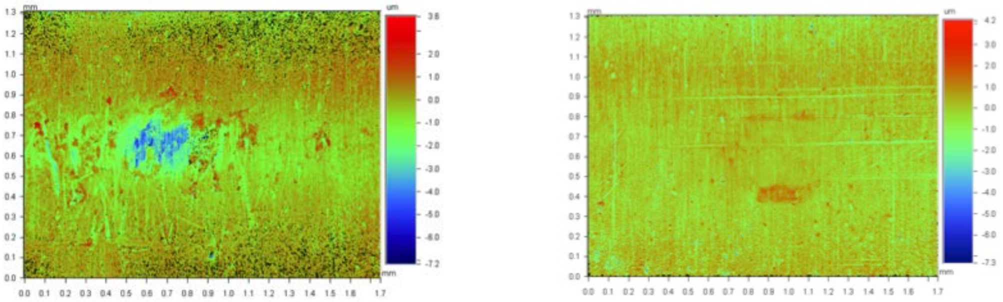

(a) Zr-SS (b) ZrO-SS

Figure 41. Wear scar morphology on Zr alloy cladding against stainless steel grid.

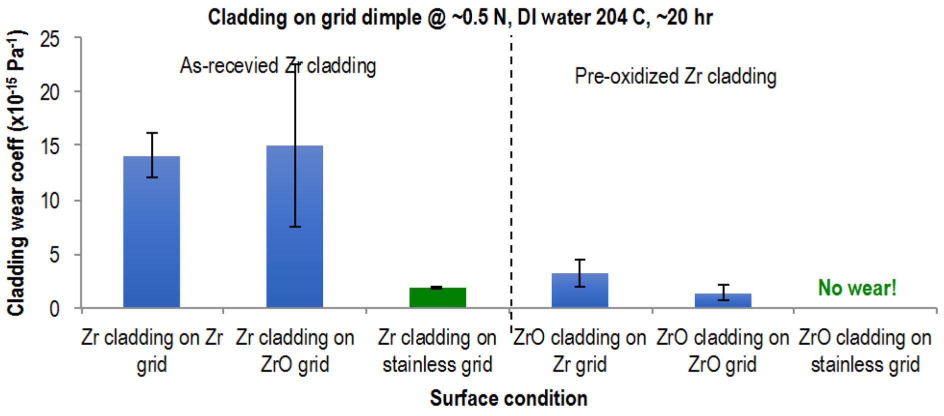

(a) Volumetric wear coefficient

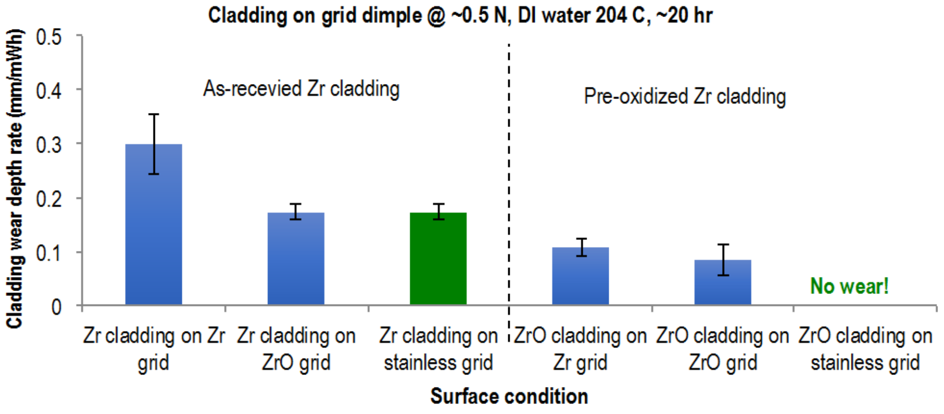

(b) Linear wear depth rate

Figure 42. Summary of wear coefficients of different material combinations tested in D.I. water by AFIR.

AFIR wear results of different material combinations in D.I. water are summarized in Fig. 42. Major observations include:

- Good repeatability in both wear coefficient and wear scar morphology.
- Water temperature matters. From 22 to 150 and then 204 ^{o}C, the cladding wear coefficient was increased by 2.5X, and 4.8X, respectively.
- Pre-oxidation of Zr alloy cladding reduced the wear coefficient by 77%. Pre-oxidation of both the cladding and grid reduced the wear coefficient by 90%.
- Grid material is important. Stainless steel grid reduced the Zr cladding wear coefficient by 87% and pre-oxidized Zr cladding had no measurable wear or surface damage when rubbing against the stainless steel grid.

4.4 Comparison of AFIR test results to WEC VIPER dynamometer data

4.5 AFIR Tests in Simulated PWR Coolants

Since PWR coolants contain B, Li, and H_2 among numerous chemical additions, additional AFIR tests were performed with controlled chemistry variations to evaluate the influence of water chemistry on fretting wear. The typical concentration of H_2 in a PWR coolant is 2-5 ppm. A special procedure was established to introduce H_2 gas into the water inside the AFIR pressure vessel:

1. Pump Ar+4% H_2 into the autoclave vessel (~1.0 L w/ the sample fixture inside) containing D.I. water (~750 mL) to 5 bars and then release the gas; repeat for twice at RT
2. Repeat the Ar+4%H2 flash (5 bars) another three times while heating up the water to 90-98 ^{o}C to ensure the dominance of Ar+4%H2 in the overgas
3. Seal the vessel (with BPR set at 22.6 bars) to allow heating up the water to 204 ^{o}C

Calculating the actual H_2 content in the heated water in the sealed vessel was a bit challenging because multiple factors had to be taken into consideration: significant water expansion, water vapor pressure, fixed amount of H_2, and temperature gradient inside the vessel. At 204 ^{o}C water temperature measured near the center of the vessel, the recorded 22-23 bars pressure indicated an overgas temperature of ~214 ^{o}C. Based on the literature data of H_2 solubility in water at elevated temperature the H_2 content in the water at 204 ^{o}C at the beginning of the AFIR test was calculated to be ~0.25 ppm according to the Henry's Law.

The typical concentrations of B and Li in a PWR coolant are 1000 and 2-3 ppm, respectively, resulting a pH in the range of 6.9-7.4. The corresponding treat rates are 0.572 wt% for H_3BO_3 and 0.0008 wt% for LiOH in D.I. water. Each AFIR test uses ~750 mL water that contains 4.3 g H_3BO_3 and 5.9 mg LiOH.

The pairs of materials in contact in each AFIR test in a simulated PWR coolant are a Zr alloy cladding rubbing against a Zr alloy grid and a stainless steel grid, respectively. The cladding wear rates for both the Zr-Zr and Zr-SS contacts are summarized in Fig. 47, and the wear scar morphology and surface composition for the Zr-Zr contact are shown in Fig. 48.

Effect of H_2

Interestingly, the 0.25 ppm H_2 seemed to reduce both the wear coefficient and oxidation of the contact area for both the Zr-Zr and Zr-SS contacts. A possible explanation is that hydrogen diffusion hardened the Zr alloy cladding and grid surface to reduce adhesion-induced frictional heating (oxidation) and material removal (wear).

Effect of H_3BO_3 and LiOH

Adding H_3BO_3 and LiOH into the water (but without H_2) significantly reduced wear but had little change in the oxidation rate. We suspect a protective tribofilm formed on the contact area and will confirm it with XPS surface chemical analysis.

Effect of H_3BO_3 and LiOH together with H_2

Adding H_3BO_3 and LiOH together with H_2 into the water reduced the wear but at a price of significantly increased oxidation on the wear scar (but little oxidation outside the wear scar), indicating tribo-corrosion.

The observations strongly suggest that wear and corrosion need to be considered together:

- Fretting can dramatically promote oxidation/corrosion;
- Wear reduction may come at a price of oxidation/corrosion.

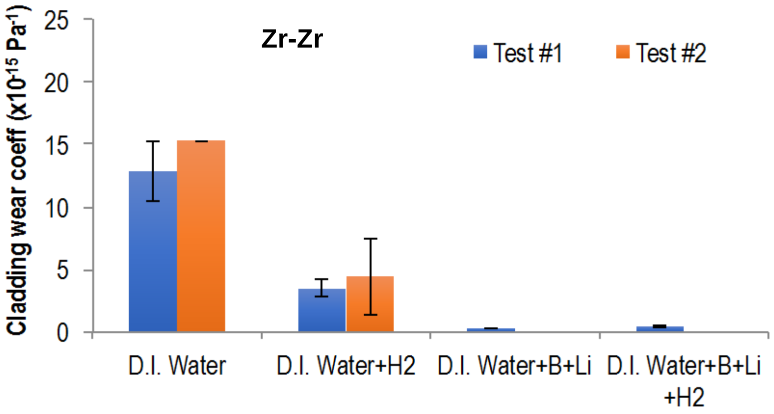

(a) Zr alloy cladding against Zr alloy grid

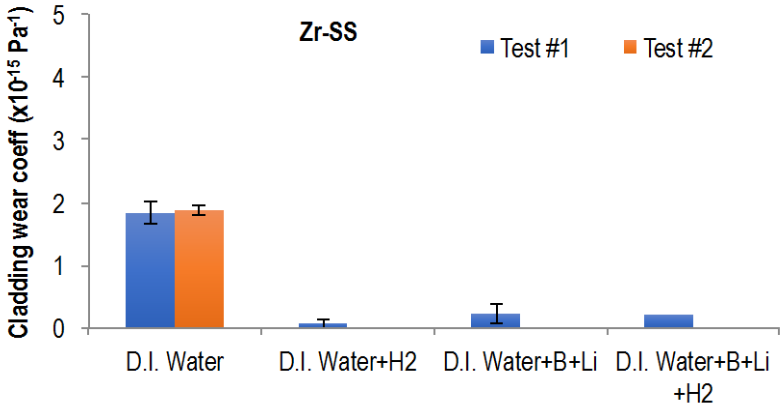

(b) Zr alloy cladding against stainless steel grid

Figure 47. Effects of water chemistry on wear coefficient.

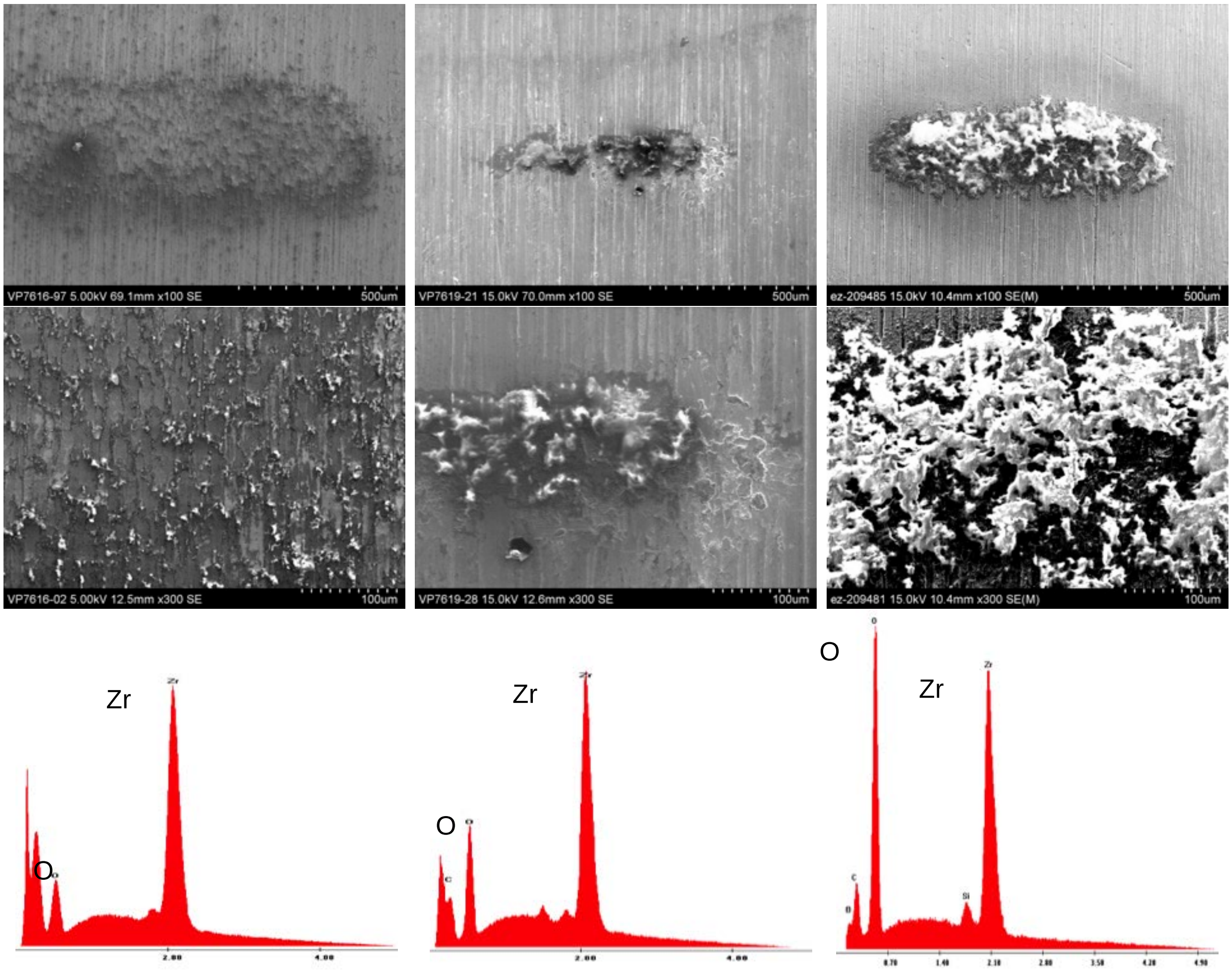

(a) D.I. water + H_2(b) D.I. water+H_3BO_3+LiOH (c) D.I. water+H_3BO_3+LiOH+H_2

Figure 48. Comparison of morphology of the cladding wear scars for the Zr-Zr contact generated in different water chemistries. The EDS spectra (compared with Fig. 12) indicating reduced, no change, increased oxidation when adding H2, B+Li, and H2+B+Li to the water, respectively.

4.6 Validation of the Engineering Wear Model against AFIR test data

The multi-stage, engineering wear model was previously described in Sections 1 and 2. Transitions between stages represent a change in the materials in contact and the respective wear factors. The basic form of the EWM indicates a direct linear dependence between the incremental wear depth and the normal force, fretting amplitude, fretting frequency and wear factor in each stage. Non-linearity is introduced by the change in the wear scar width on the cladding (cylinder) as the wear depth increases, and by the imposition of a relaxation in the normal force, as shown in the earlier examples. However, there was no direct consideration of the effects of ambient temperature or periodic gap development/evolution in the EWM. While impact-fretting combinations have yet to be explored in the AFIR at the time of this writing, the effects of temperature and some information on the relationship between maximum wear depth in the cladding and the wear volume has become available and are discussed in the following subsections.

Training the EWM to account for Temperature

Initially, the AFIR tests were done using increasing conditions of severity. This stepwise approach was used to ensure that the temperature, pressure, load, and amplitude of contact were performing as expected from the design. The first series of experiments on self-mated, as-received Zr™ alloys (both the grid and cladding specimens were made of the same material) used three different temperatures: 22, 150, and 204 ^{o}C. Measurements of the wear damage enabled an initial assessment of the effects of temperature. Based on data obtained on 16, 22, 31 May 2017 and on 20 June 2017, the wear factors for the cladding specimen were measured. The ratio of the wear factor (W_f) at each test temperature (in degrees K) relative to that for the tests at room temperature (T = 295.15 K or 22 C) can be directly compared.

Here we define the normalized temperature (Θ_T) as the ratio of the test temperature (T_{test}) to room temperature (T_{ref}) in degrees K. The non-dimensional reference temperature was taken to be 295.15 K (22 ^{o}C):

$$\Theta_T = \frac{T_{test}}{T_{ref}} = \frac{T_{test}}{295.15} \tag{19}$$

and similarly, the non-dimensional ratio of the average wear factors (Ω_{Wf}) for the two grid material contacts rubbing against a cladding tube) obtained at T_{test}:

$$\Omega_T = \frac{W_{f,T=Ttest}}{W_{f,T=295K}} \tag{20}$$

Using ORNL/AFIR data provided on 13 July 2017, the normalized temperature was plotted versus the ratio of wear factors obtained under similar test conditions, but at three difference temperatures is plotted in Figure 49. There is a reasonable exponential fit to the data in terms of the normalized parameters defined in Eqns. (19) and (20).

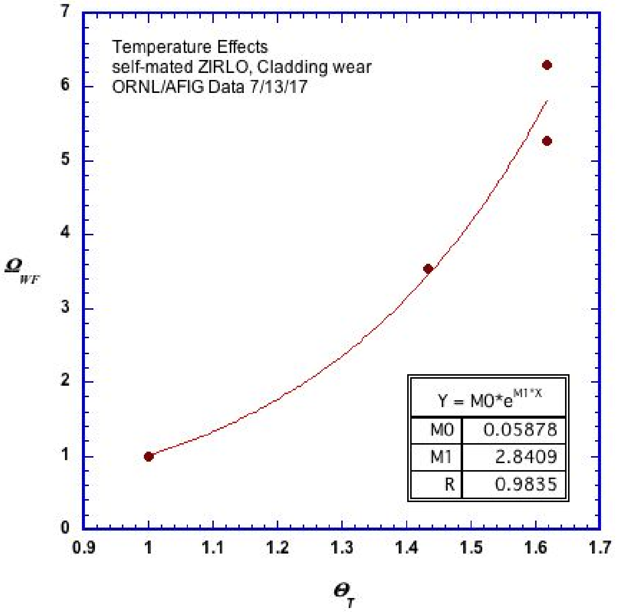

Figure 49. Normalized test temperature versus relative wear factor for self-mated Zr specimens in the ORNL/AFIR. Each point represents the average wear rate of two contacts on the cladding/grid pair. A reasonable exponential curve fit was obtained albeit for the limited data.

The relationship between the increase in wear factor due to temperature is therefore:

$$W_{f,T=T} = 0.059e^{2.84\Theta_T} \tag{21}$$

To account for the effects of temperature on the wear factor derived from ORNL experiments on that equipment, one can modify Eqn. (1) to account for temperature by adding a pre-factor as follows:

$$z_t = z_0 + \left(\frac{Fx}{A}\right)\left[0.059e^{2.84\Theta_T}\right]W_f \tag{22}$$

where z_t = the total wear depth after time increment t, z_0 = the wear depth at the beginning of time increment t, Fx = the frictional work dissipated during time increment (i.e., average friction force F times the sliding contact distance x), A = the average contact area over which the frictional work is dissipated*, W_f = the wear factor obtained under room temperature conditions, and Θ_T is the normalized temperature defined in Eqn. (19).

One then could approximate the effects of temperature on the wear factors that were obtained in similar equipment at room temperature. To the best of our knowledge, this is the first time such a correction has been available.

Area function based on volume and depth

Initial ORNL measurements of wear volumes and maximum depth were obtained about 13 July 2017 and distributed to the GTRF team. While some of the wear scars, especially those against stainless steel grids and pre-oxidized specimens were smaller and less regular shaped that others, many of the cladding specimens wear scars exhibited shapes very similar to those from VIPER tests at WEC, from experiments, and from GTRF fretting simulations published in the literature. Figure 39a shows one of the scar shapes from an ORNL test of self-mated Zr, as-received. From this figure, the contact area is approximately (1.75 long x 0.42 wide, area of an ellipse = π *a b* = (π/4) (1.75 x 0.42) = 0.577 mm^2). The ratio of the wear volume to the scar depth can used to approximate the contact area. Using volume and maximum scar depth data from ORNL, the contact area of specimens consisting of self-mated Zr is plotted in Figure 50.

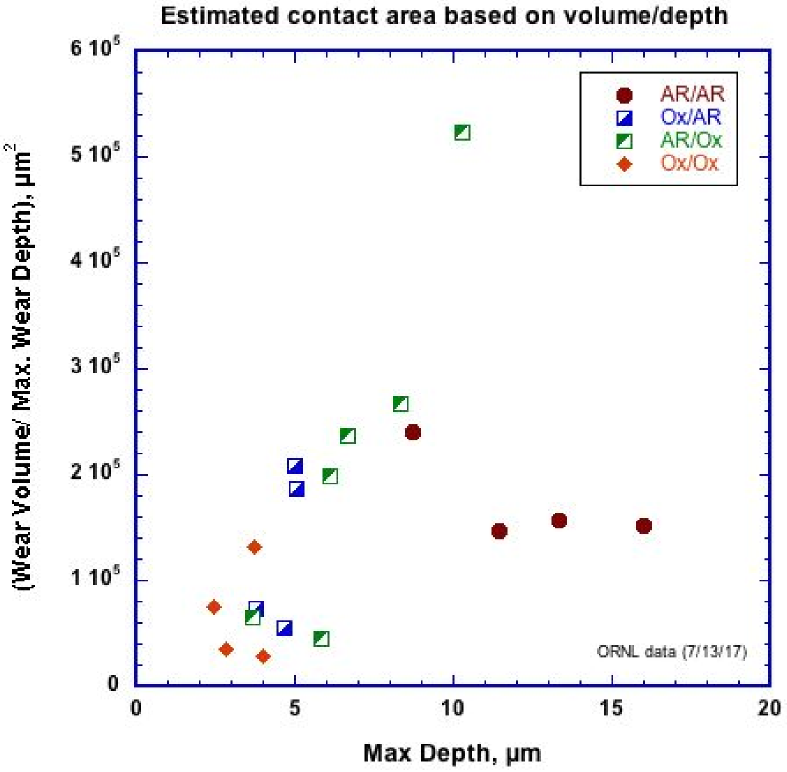

Figure 50. Estimate of the contact area (μm2) using AFIR data on scar volume and maximum scar depths. (AR = as-received Zr, Ox = pre-oxidized Zr, order: clad/grid material)

Figure 50 fails to indicate a correlation that would enable one to back-calculate the contact area from wear depth information to use in the denominator of Eqn. (1). This disappointing lack of a correlation is likely the result of the unevenness and asymmetry of the wear contact as the components adjust to the mechanical and thermal conditions during operation. This problem is especially evident when the scar depths are quite shallow. While the scars are not perfectly symmetrical, the geometry of scars deeper than a few µm can still be approximated by a narrow ellipse or a narrow rectangle. The length of the scar would then be determined from the geometry of the dimple and spring design. The instantaneous width at a given time would be the cumulative wear scar dimensions.

<u>Accounting for sliding amplitude</u>

Figure 51 shows, for various combinations of Zr specimens (oxidized versus as-received), the effects of an increase in fretting stroke length (amplitude) results in an increase in the wear coefficient (wear factor). The effect of stroke length seems larger for couples in which only one member of the pair is pre-oxidized. From the limited data in Figure 40 it cannot be determined if this dependence is linear, but as assumed in the EWM [Eqns. (1 and 2)], an increase in sliding length increases the wear coefficient. From Figure 41, it seems that there is a larger effect of stroke length on wear coefficient than the 1:1 effect assumed in Eqn. (1). Further experimental work may result in changing the model to reflect how W_f changes with δ. Classical studies of fretting indicate a sigmoidal curve shape of amplitude versus wear volume in fretting. Therefore, the amplitude versus wear factor relationship may be linearly approximated only within a certain range.

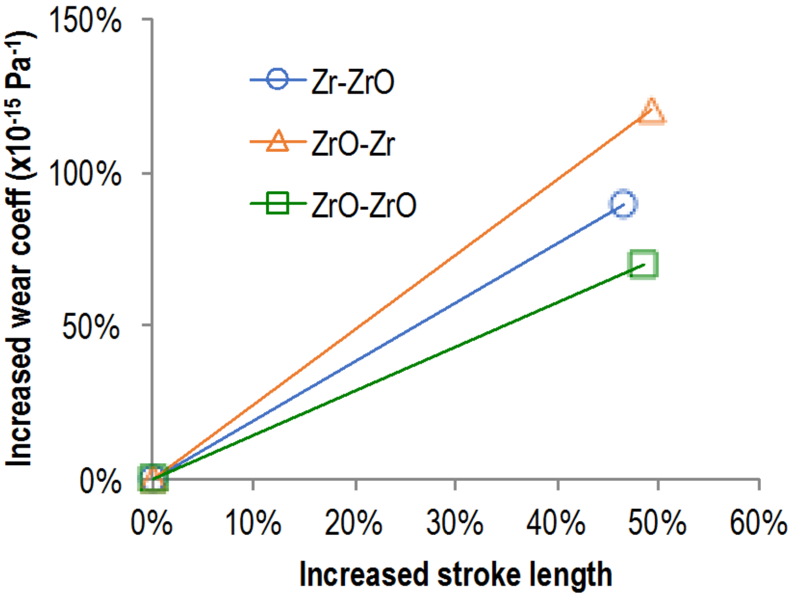

Figure 51. Effects of increasing the contact stroke length on wear of Zr and pre-oxidized Zr fretting couples.

Coolant chemistry effects

Tribochemistry is the science and related technology that concerns the influence of the local chemical environment on interfaces that are subjected to wear. Along with the behavior of fluids flowing through confined spaces, it is part of the basis for lubrication science, especially in the boundary lubrication regime in which surfaces make contact in the presence of reactive species. It underlies the oil and grease industries that depend on additives to reduce friction and wear. One aspect of tribochemistry is tribocorrosion and the synergy between mechanical wear and chemically-affected surface damage. Tribocorrosion is a concern in numerous applications including mining, agriculture, the petroleum industry, ocean engineering, bio-implants, aerospace propulsion, ground propulsion, and the nuclear industry, among others. In the present case, GTRF occurs in a chemical environment composed of hot, flowing coolant that contains intentional additives as well as reaction products and contaminants like CRUD.

The properties of the chemical environment are affected by temperature as well as the composition of the fluid and tribosurface. All these may change with time, so the ability to study such effects is important when simulating GTRF wear processes in the laboratory. After consulting with experts in nuclear component corrosion, the AFIR was used to conduct studies of the effects of H_3BO_3, LiOH, and H_2 in simulated coolant situations. Twenty-hour-long tests of self-mated Zr were in four tribochemical conditions were conducted with applied pressure of 18-24 Bar, temperature of 204 ^{o}C, contact force of 0.4-0.6 N, frequency of 25 Hz, and slip amplitude of 190 µm or 50-100 ± µm (closed loop). The simulated coolants were the following:

1) Deionized water (N_2)
2) Deionized water + 0.25 ppm H_2 (Ar+4% H_2)
3) Deionized water + H_3BO_3 [1000 ppm B] and LiOH [2.3 ppm Li] (N_2)
4) Deionized water + H_2 + H_3BO_3 and LiOH (Ar+4% H_2)

After testing in 750 ml of coolant for each test, there was noticeable coloration of the specimens indicating changes in surface composition after coolant exposure. Detailed results are not repeated here, but the primary findings of this initial work on tribochemical effects on GTRF wear of self-mated Zr (two tests for each condition) are summarized in Table 6.

Table 6. Preliminary AFIR Test Results: Effects of Coolant Composition on Wear Coefficient (20-24 Bar, 204 oC, 25 Hz, 0.4-0.6 N load)

Test Fluid	Nominal wear rate $\times 10^{-6}$ (mm^3/N-m)	Scar appearance
Deionized water	~ 13. - 15.	elongated ellipse with patches irregular pitting
Deionized water + H_2	~ 4.- 5.	relatively smooth; more uniform pit distribution
Deionized water + H_3BO_3 + LiOH	< 1.	small, irregularly shaped
Deionized water + H_2 + H_3BO_3 + LiOH	< 1.	indication of an small ellipse, but non-uniform shape; significant tribo-oxidation products in the contact area

When the grid specimen was changed to stainless steel, similar results obtained, but further review of the data is being done at this writing at ORNL. What can be stated, based on the available, albeit preliminary data is that compared with results for tests in deionized water, all of the simulated coolant compositions, involving H, H_3BO_3, and LiOH reffectively reduced the rate of wear. Thus one could further modify the EWM for continuous fretting without compensation for a contact gap by incorporating a factor (ψ)that accounts for tribo-chemical effects as follows:

$$z_t = z_0 + \Psi\left(\frac{Fx}{A}\right)[0.059e^{2.84\Theta_T}]W_f \qquad (23)$$

Where, by Eq. (2), x = $2\delta\nu t$. Recall, from section 3.4.3, that the effect of the fretting amplitude (δ) may be other than linear. Note also that the values of 0.059 and 2.84 in Eqn. (23) are empirical fits to limited AFIR data, and their values in actual reactor situations may differ. Likewise, the value for ψ would have to be empirically determined. For the reader's convenience, the definitions and units used for the symbols in Eqn. (23) are reproduced in Table 7.

Table 7. Parameter Definitions for the Modified Engineering Wear Model.

Symbol	Description	Units of measure
A	area of the wear scar on the cladding (approximated by an elongated ellipse or an elongated rectangle)	mm^2
F	kinetic friction force (=μP)	N
P	normal force applied to the wear scar during fretting contact	N
t	interval of fretting contact for each calculation within the given stage	s
T_{ref}	reference temperature at which the wear factor was determined (298.16 K = 25 ^{o}C in the present case)	K
T_{test}	testing (operating) temperature	K
W_f	wear factor operating during the given stage of GTRF wear	mm^3/N-m
x	total sliding distance during time interval t_{inc}	mm
z_t	total depth of wear; the sum of the initial wear depth and the increment z_i	µm or mm
z_0	depth of wear at the beginning of the increment of wear calculation	µm or mm
μ	average friction coefficient on the wear scar during time t	non-dimensional
δ	amplitude of fretting (stroke length)	µm
ν	frequency of fretting	s^{-1}
Θ_T	normalized temperature factor (= T_{test} / T_{ref})	non-dimensional
ψ	empirical factor that scales the rate of wear by the influence of coolant chemistry	non-dimensional

5. SUMMARY

A materials tribology approach was taken assuming that the wear factor of the cladding reflected how effectively the available frictional work was converted in to wear volume and hence, wear depth in the cladding. That efficiency was reflected by the magnitude of the “wear factor”. Its derivation relied on a number of sources including consultation with industry, the literature, interviews with experts in fretting wear; experimental findings and data from ORNL, Westinghouse, and elsewhere; and the authors’ experience. A metallurgical approach was taken to compute the magnitude of the wear factor based on the nucleation of wear debris from pre-existing ‘embryos’ (defects) in the material arising from microstructures of the alloys in as-processed form and cladding that had be intentionally oxidized. Some parameters in that derivation (such as the probability that a defect will nucleate an incipient wear particle), while physically reasonable, are difficult to compute or measure, forcing estimates to be made.

The availability of simulative data from elevated temperature, pressurized coolant, wear tests of Zr alloys and grids at ORNL made possible improvements in the form of the EWM. The complex role of gaps and impacts was reflected by a pre-factor in the model. However, physically the magnitude of the effects of gaps was complicated by the role of fluid dynamics from the flowing coolant into the converging grid/clad gap. Pressure which counteracts the normal grid/clad clamping force can be generated in that way and the flow of coolant can aid in fretting wear debris removal. Large closing forces could in principle add an impact component to the wear rate, but remains to be verified.

The following general conclusions were drawn from this work:

- A great deal of research has been done on fretting, but GTRF presents some special problems and complexities that do not conform to the assumptions of classical studies, like a reciprocating sphere-on-flat under dry conditions.
- Like wear in general, GTRF wear is a cumulative process that sums incremental material loss or displacements over time, and the rate of wear can change as reactor operating conditions and surface material changes. Physical changes to the contact conditions include oxide loss, exposure of the substrate, and hydrogen embrittlement (tribo-corrosion).
- One of the main findings of the initial computational fluid dynamics modeling effort within GTRF is that the fuel rod displacement, acceleration and wear work-rates as obtained from the nonlinear dynamics computations using VITRAN are relatively insensitive to the use of either Hydra-TH or STAR- CCM+ for computing fluid forces on the rod.
- The dissipation of frictional work during wear is affected by the partition of energy needed to generate wear particles from the surface of the cladding (and grid), to form third-body debris layers, to destroy those layers, and to remove debris layer fragments. Thus, both a primary and secondary debris process are envisioned.
- Structural mechanics modeling of the multiple rod and grid contact within fuel assemblies indicates that the patterns of leaking rods is concentrated along external corners and edges, in agreement with observations.
- Structural mechanics modeling has identified the effect of crystallographic texture within the spacer grids, revealing that thermal-mechanical processing of the grids to produce basal poles aligned along the transverse or normal direction, as opposed to aligned along the rolling direction, will impede the development of fuel-grid gap that minimizes fretting wear.
- Based on the literature and computational modeling, wear factors for fretting in GTRF environments seem to fall within the range of 10^{-5} to 10^{-7} mm^3/N-m or below. (This corresponds to 10^{-14} to 10^{-16} in units of Pa^{-1}.)
- The good agreement between ORNL AFIR and WEC VIPER on both wear rate and morphology provides a solid foundation for correlating AFIR results with field experience and using them for training and validating GTRF models including EWM.
- Surface treatment of the cladding and grid material are important. Pre-oxidation of Zr alloy cladding and/or using stainless steel grid effectively reduced the cladding wear rate.
- Wear and corrosion must be considered together. Fretting can dramatically promote oxidation/corrosion, and wear reduction may come at a price of oxidation/corrosion
- A exponential form of temperature compensation can be added to the EWM to compensate for the effects of temperature on wear factors, as observed in AFIR experiments at ORNL. Thus, some means of extrapolating wear data obtained in lower-temperature studies to those more typical of reactor operation can be approximated.
- To date, the effects of radiation on the wear behavior of materials can only be estimated by adjusting the magnitude of the wear factors used in the EWM. No accurate data on possible radiation effects on the wear rates of Zr-based alloys, stainless steels, or Ni-based superalloys has been found so those effects cannot be directly predicted by the EWM.

6. REFERENCES

1. K. Edsinger, C.R. Stanek and B.D. Wirth, “Light Water Reactor Fuel Performance: Current Status, Challenges, and Future High Fidelity Modeling”, *JOM* **63** (2011) 49-52.
2. R. Lu, Z. Karoutas, and T.-L. Sham, “CASL Virtual Reactor Predictive Simulation: Grid-to-Rod Fretting Wear”, *JOM* **63** (2011) 53-58.
3. W. Lu, M.D. Thouless, Z.P. Hu, H. Wang, R. Ghelichi, C.H. Wu, K. Kamrin, and D. Parks, “CASL Structural Mechanics Modeling of Grid-to-Rod Fretting (GTRF), *JOM* **68** (2016) 2922-2929.
4. Kyu-Tae Kim and Jung-Min Suh, “Impact of nuclear fuel assembly design on grid-to-rod Fretting Wear,” *Journal of Nuclear Science and Technology*, **46**, 149-157, 2009.
5. Y-H Lee and H-K Kim: *Wear*, 301, 569 (2013).
6. P. J. Blau, J. Qu, and R. Lu (2016) “Modeling of Complex Wear Behavior Associated with Grid-to-Rod Fretting in Light Water Nuclear Reactors,” *JOM* **68** (2016) 2938-2943.
7. M.A. Christon, R. Lu, J. Bakosi, B.T. Nadiga, Z. Karoutas, and M. Berndt, “Large-eddy simulation, fuel rod vibration and grid-to-rod fretting in pressurized water reactors”, *Journal of Computational Physics* **322** (2016) 142-161.
8. H. Czichos: *Tribology – A systems approach to the science and technology of friction, lubrication and wear* (Amsterdam, Netherlands Elsevier Publishing, 1978) pp. 30-42.
9. P. J. Blau: *Wear*, 313 (1-2), 89 (2014).
10. J. F. Archard: *J. Appl. Phys*., 24 (3), 981 (1953).
11. O. Vingsbo and S. Soderberg : *Wear*, 126 (2), 131 (1988).
12. E. Rabinowicz: *Friction and Wear of Materials* (New York, New York: John Wiley and Sons, 1965) p. 138.
13. P.J. Blau, Tribosystem analysis: A practical approach to the diagnosis of wear problems, (CRC Press, Taylor & Francis, New York, 2016).
14. P. J. Blau, A. V. Hayrapetian, and M. Demkowicz (2012) “Development of a Predictive Wear Model for Grid-to-Rod Fretting in Lightwater Nuclear Reactors,” in ASTM STP 1563, Tribo-Corrosion: Research, Testing, and Applications, ed. P. J. Blau, J-P. Celis, and D. Drees, ASTM International, W. Conshohocken PA, pp. 139-158.
15. J. Qu, K.M. Cooley, A.H. Shaw, R.Y. Lu, P.J. Blau, “Assessment of wear coefficients of nuclear zirconium claddings without and with pre-oxidation,” Wear 356-357 (2016) 17-22.
16. K-T Kim (2010) A study on the grid-to-rod fretting wear-induced fuel failure observed in the 16 **x**16KOFA fuel. *Nuclear Engineering and Design* 240, pp. 756–762.
17. A. Rosenfield, “A fracture mechanics approach to wear,” *Wear*, 61(1980) pp. 125-132.
18. A. Patra, and C.N. Tome, “Finite element simulation of gap opening between cladding tube and spacer grid in a fuel rod assembly using crystallographic models of irradiation growth and creep”, *Nuclear Engineering and Design* **315** (2017) 155-169.
19. R. A. Holt, A. R. Causey, N. Christodoulou, M. Griffiths, E. T. C. Ho, and C. H. Woo, “Non-linear irradiation growth of cold-worked Zircaloy-2,” presented at the Zirconium in the Nuclear Industry: Eleventh International Symposium, ASTM STP 1295, E.R. Bradley and G.P. Sabol, Eds., 1996, pp. 623–637.
20. D. Lhuillier and C. Tome, “Modeling of irradiation and thermal creep of pressure tubes: 1. Texture reduction and interpolation,” Atomic Energy of Canada Ltd., COG-94-232 RC-1222, 1995.
21. R. Liu, A. Prudil, W. Zhou, and P. K. Chan, “Multiphysics coupled modeling of light water reactor fuel performance,” *Progress in Nuclear Energy*, vol. 91, pp. 38–48, Aug. 2016.

22. R. L. Williamson, “Enhancing the ABAQUS thermomechanics code to simulate multipellet steady and transient LWR fuel rod behavior,” *Journal of Nuclear Materials*, vol. 415, no. 1, pp. 74–83, Aug. 2011.
23. R. L. Williamson *et al.*, “Multidimensional multiphysics simulation of nuclear fuel behavior,” *Journal of Nuclear Materials*, vol. 423, no. 1–3, pp. 149–163, Apr. 2012.
24. A. Patra, C. N. Tomé, and S. I. Golubov, “Crystal plasticity modeling of irradition growth in Zircaloy-2,” *Philosophical Magazine* **97** (2017) 2018-2051.
25. H. Jiang, J. Qu, R. Y. Lu, and J.-A. J. Wang, “Grid-to-rod flow-induced impact study for PWR fuel in reactor,” *Progress in Nuclear Energy*, vol. 91, pp. 355–361, 2016.
26. T. P. Joulin, F. M. Guérout, A. Lina, and D. Moinereau, “Effects of loading conditions and types of motion on PWR fuel rod cladding wear,” pp. 1011–1018, 2002.
27. A. Billerey, “Evolution of fuel rod support under irradiation–Impact on the mechanical behaviour of fuel assemblies,” *Structural behaviour of fuel assemblies for water cooled reactors,(in Cadarache, France, 22–26 November 2004), IAEA-TECDOC-1454*, pp. 101–111, 2005.
28. J. Yan, K. Yuan, E. Tatli, and Z. Karoutas, “A new method to predict Grid-To-Rod Fretting in a PWR fuel assembly inlet region,” *Nuclear Engineering and Design*, vol. 241, no. 8, pp. 2974–2982, 2011.
29. Hillner, E., Franklin, D. G., and Smee, J. D. (2000). Long-term corrosion of Zircaloy before and after irradiation. *Journal of Nuclear Materials, 278*, 334-345.
30. McColl, I. R., Ding, J., & Leen, S. B. (2004). Finite element simulation and experimental validation of fretting wear. *Wear*, *256*(11), 1114-1127.
31. P. R. Rubiolo, “Probabalistic prediction of fretting-wear damage of nuclear fuel rods,” *Nuclear Engineering and Design*, **236**, 1628-1640, 2006.
32. P. H. Wirsching, T. H. Paez, and K. Ortiz, *RANDOM VIBRATIONS Theory and Practice*, John Wiley, New York, 1995.
33. P. R. Rubiolo and M. Y. Young, “VITRAN: an Advance Statistic Tool to Evaluate Fretting-wear Damage,” *Journal of Power and Energy Systems*, **2**, 57-66, 2008.
34. Z. Karoutas, M. Krammen, Y. Aleshin, R. Kesterton, and S. Grill, “Prediction of Grid to Rod Gap for Fuel Rod Vibration Analysis in PWR Cores,” Paper 2014 in *Proceedings*, *Top Fuel 2009*, Paris, Sept. 2009.
35. Kamrin, Ken, Chris H. Rycroft, and Jean-Christophe Nave. "Reference map technique for finite-strain elasticity and fluid–solid interaction." *Journal of the Mechanics and Physics of Solids* **60.11**, 1952-1969, 2012.
36. Valkov, Boris, Chris H. Rycroft, and Ken Kamrin. "Eulerian method for multiphase interactions of soft solid bodies in fluids." *Journal of Applied Mechanics* **82.4**, 041011, 2015.
37. P. J. Blau (1997) "Design and validation of laboratory-scale simulations for selecting tribomaterials and surface treatments," Chapter, in New Directions in Tribology, ed. I. M. Hutchings, Mech. Engr. Pub., Ltd., Suffolk, UK.
38. P. J. Blau (2001) “Simulative Friction and Wear Testing,” Chapter 14 in Handbook of Modern Tribology, Vol. 1, ed. B. Bhushan, CRC Press, Boca Raton, Florida, pp. 511-522.
39. H. Jiang, J. Qu, R.Y. Lu, J.J. Wang, “Grid-to-rod flow-induced impact study for PWR fuel in reactor,” Progress in Nuclear Energy 91 (2016) 355–361.
40. R.Y. Lu, M.E. Conner, M.L. Boone, C.L. Wilbur, R. Marshall, Nuclear fuel assembly flow-induced vibration and endurance testing, In: *Proceeding of Symposium on Flow-Induced Vibration* – 2001 ASME Pressure Vessels and Piping Conference, July 22–26, 2001, Atlanta, Georgia.
41. R.Y. Lu and Z. Karoutas, “Application of VERA Advanced Codes to Grid-to-Rod Fretting Wear,” CASL Milestone Report L3:AMC:CHLNG:P5.01, 2012.

42. R.Y. Lu, “17x17 V5H Fretting Wear Data from VIPER Long-Term Wear Test,” Westinghouse Report PFT-12-28, 2012.

Appendix A. Bibliography of CASL publications related to GTRF Challenge Problem

K. Edsinger, C.R. Stanek and B.D. Wirth, “Light Water Reactor Fuel Performance: Current Status, Challenges, and Future High Fidelity Modeling”, *JOM* **63** (2011) 49-52.

R. Lu, Z. Karoutas, and T.-L. Sham, “CASL Virtual Reactor Predictive Simulation: Grid-to-Rod Fretting Wear”, *JOM* **63** (2011) 53-58.

P. J. Blau, A. V. Hayrapetian, and M. Demkowicz (2012) “Development of a Predictive Wear Model for Grid-to-Rod Fretting in Lightwater Nuclear Reactors,” in ASTM STP 1563, Tribo-Corrosion: Research, Testing, and Applications, ed. P. J. Blau, J-P. Celis, and D. Drees, ASTM International, W. Conshohocken PA, pp. 139-158.

H. Wang, Z. Hu, W. Lu, and M.D. Thouless, “A mechanism-based framework for the numerical analysis of creep in zircaloy-4”, *Journal of Nuclear Materials* **433** (2013) 188-198.

P. J. Blau: *Wear*, 313 (1-2), 89 (2014).

Z.P. Hu, W. Lu and M.D. Thouless, “Simulation of wear evolution using fictitious eigenstrains”, *Tribology International* **82** (2015) 191-194.

P.J. Blau, <u>Tribosystem analysis: A practical approach to the diagnosis of wear problems,</u> (CRC Press, Taylor & Francis, New York, 2016).

J. Qu, K.M. Cooley, A.H. Shaw, R.Y. Lu, P.J. Blau, “Assessment of wear coefficients of nuclear zirconium claddings without and with pre-oxidation,” Wear 356-357 (2016) 17-22.

W. Lu, M.D. Thouless, Z.P. Hu, H. Wang, R. Ghelichi, C.H. Wu, K. Kamrin, and D. Parks, “CASL Structural Mechanics Modeling of Grid-to-Rod Fretting (GTRF), *JOM* **68** (2016) 2922-2929.

Z.P. Hu, W. Lu and M.D. Thouless, “Effect of plastic deformation on the evolution of wear and local stress fields in fretting”, *International Journal of Solids and Structures* **82** (2016) 1-8.

P. J. Blau, J. Qu, and R. Lu “Modeling of Complex Wear Behavior Associated with Grid-to-Rod Fretting in Light Water Nuclear Reactors,” *JOM* **68** (2016) 2938-2943.

M.A. Christon, R. Lu, J. Bakosi, B.T. Nadiga, Z. Karoutas, and M. Berndt, “Large-eddy simulation, fuel rod vibration and grid-to-rod fretting in pressurized water reactors”, *Journal of Computational Physics* **322** (2016) 142-161.

Z.P. Hu, M.D. Thouless and W. Lu, “Effects of gap size and excitation frequency on the vibration behavior and wear rate of fuel rods”, *Nuclear Engineering and Design* **308** (2016) 261-268.

A. Patra, C. N. Tomé, and S. I. Golubov, “Crystal plasticity modeling of irradition growth in Zircaloy-2,” *Philosophical Magazine* **97** (2017) 2018-2051.

A. Patra, and C.N. Tome, “Finite element simulation of gap opening between cladding tube and spacer grid in a fuel rod assembly using crystallographic models of irradiation growth and creep”, *Nuclear Engineering and Design* **315** (2017) 155-169.

H. Wang, Z.P. Hu, W. Lu, and M.D. Thouless, “The effect of coupled wear and creep during grid-to-rod fretting”, *Nuclear Engineering and Design* **318** (2017) 163-173.